

Data processing and calibration techniques in a 3-D videogrammetric PTV system

Hans-Gerd Maas

Institute of Geodesy and Photogrammetry

ETH - Hönggerberg, CH - 8093 Zürich, Switzerland

Tel. +41-1-6333058, Fax +41-1-6331101, e-mail gerd@p.igp.ethz.ch

Handouts

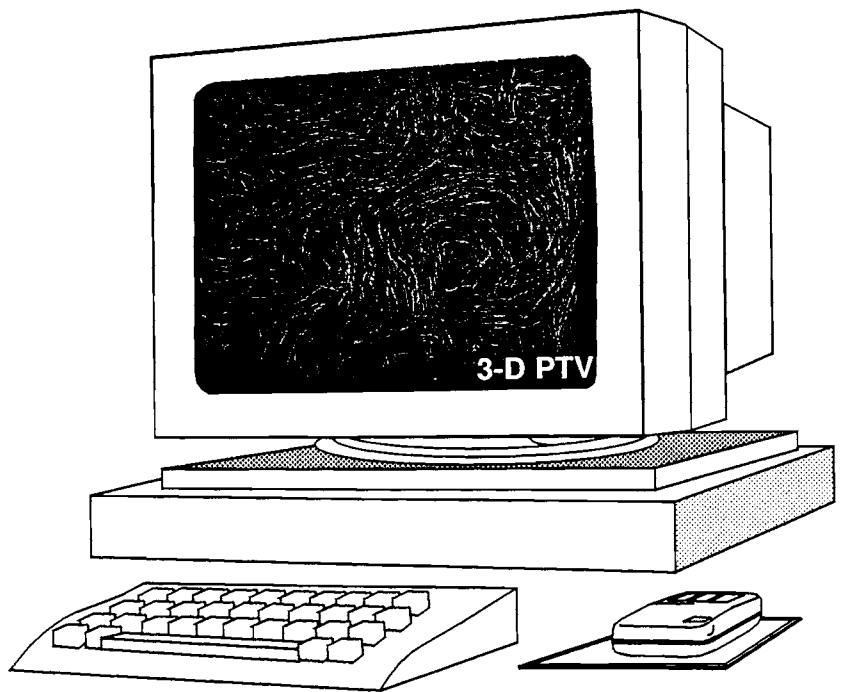
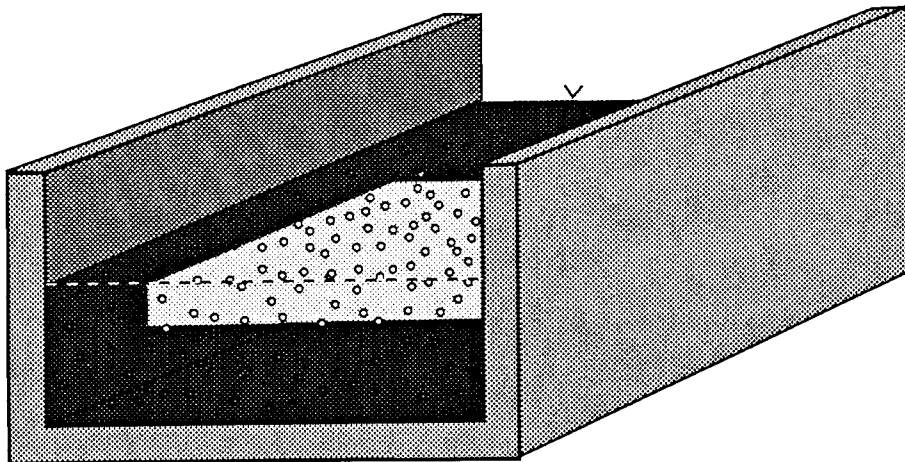
Short Course

in

3-D Velocimetry and Image Analysis Techniques

Zurich, March 1-3, 1995

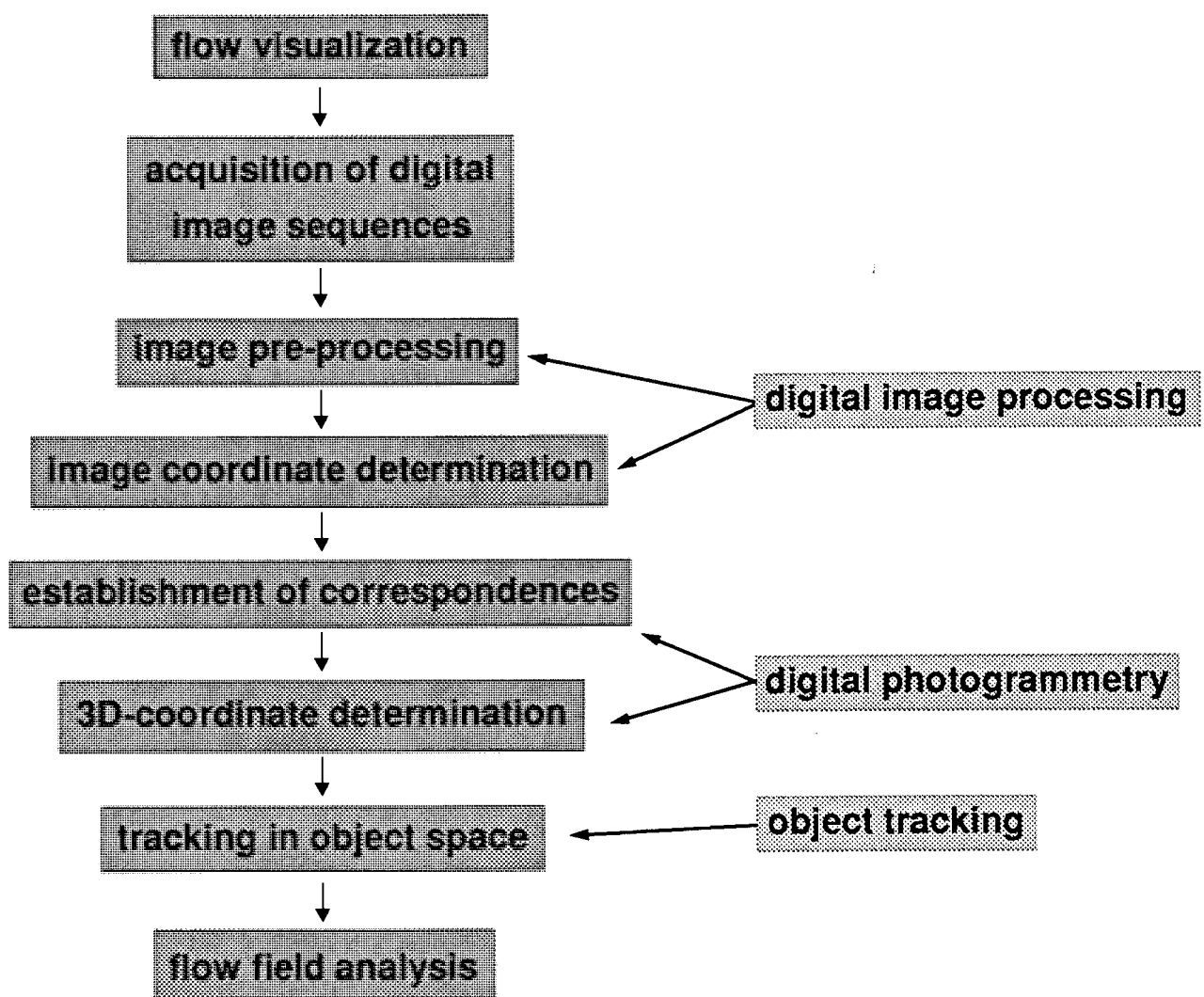
3-D Particle-Tracking-Velocimetry (3-D PTV)



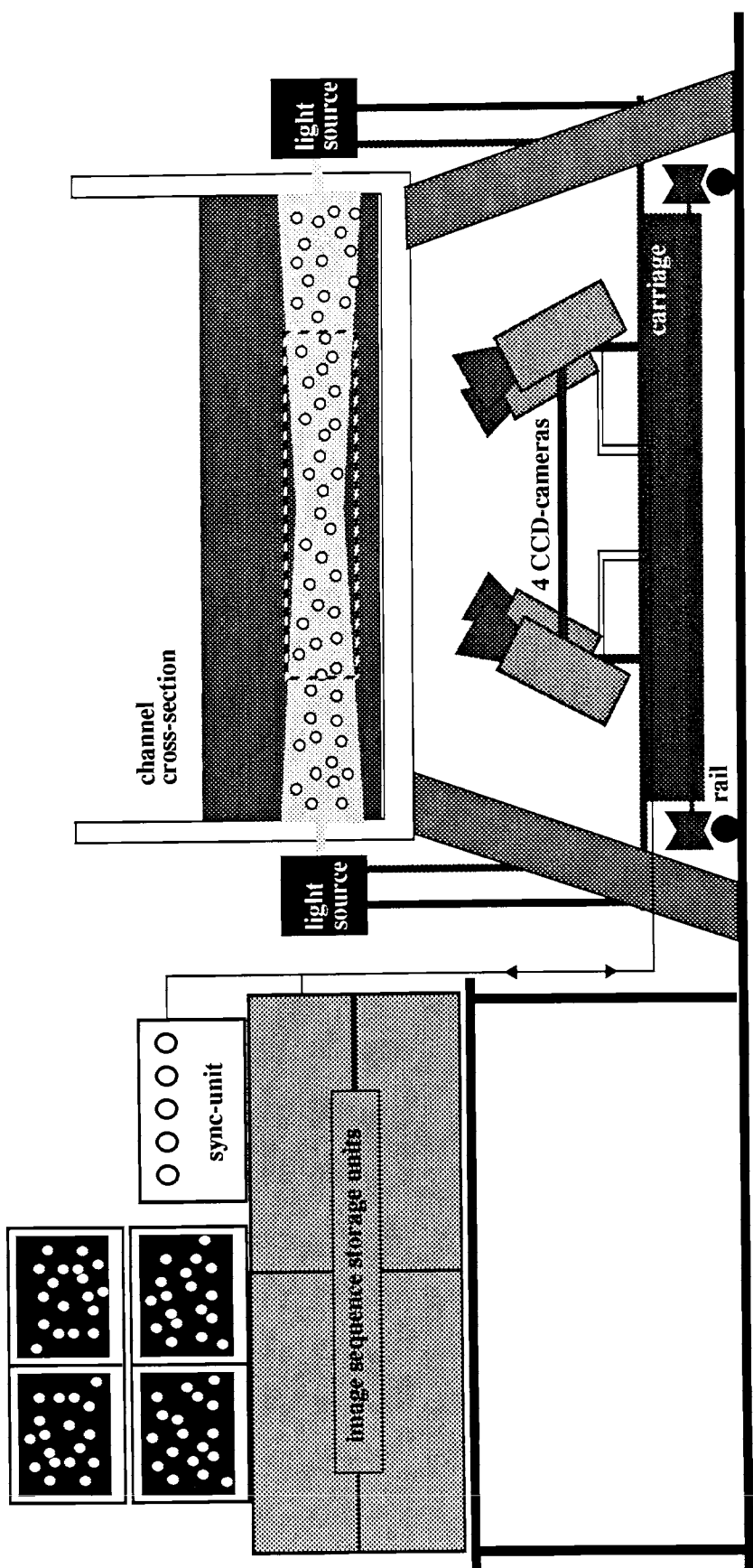
Principle:

- > Flow visualization by tracer particles
- > Illumination of a 3-D observation volume
- > Stereoscopic recording by two (or more) CCD cameras
- > Photogrammetric 3-D coordinate determination**
- > Velocity vectors from consecutive datasets
- > Particle trajectories from image sequences

Flow chart 3-D PTV

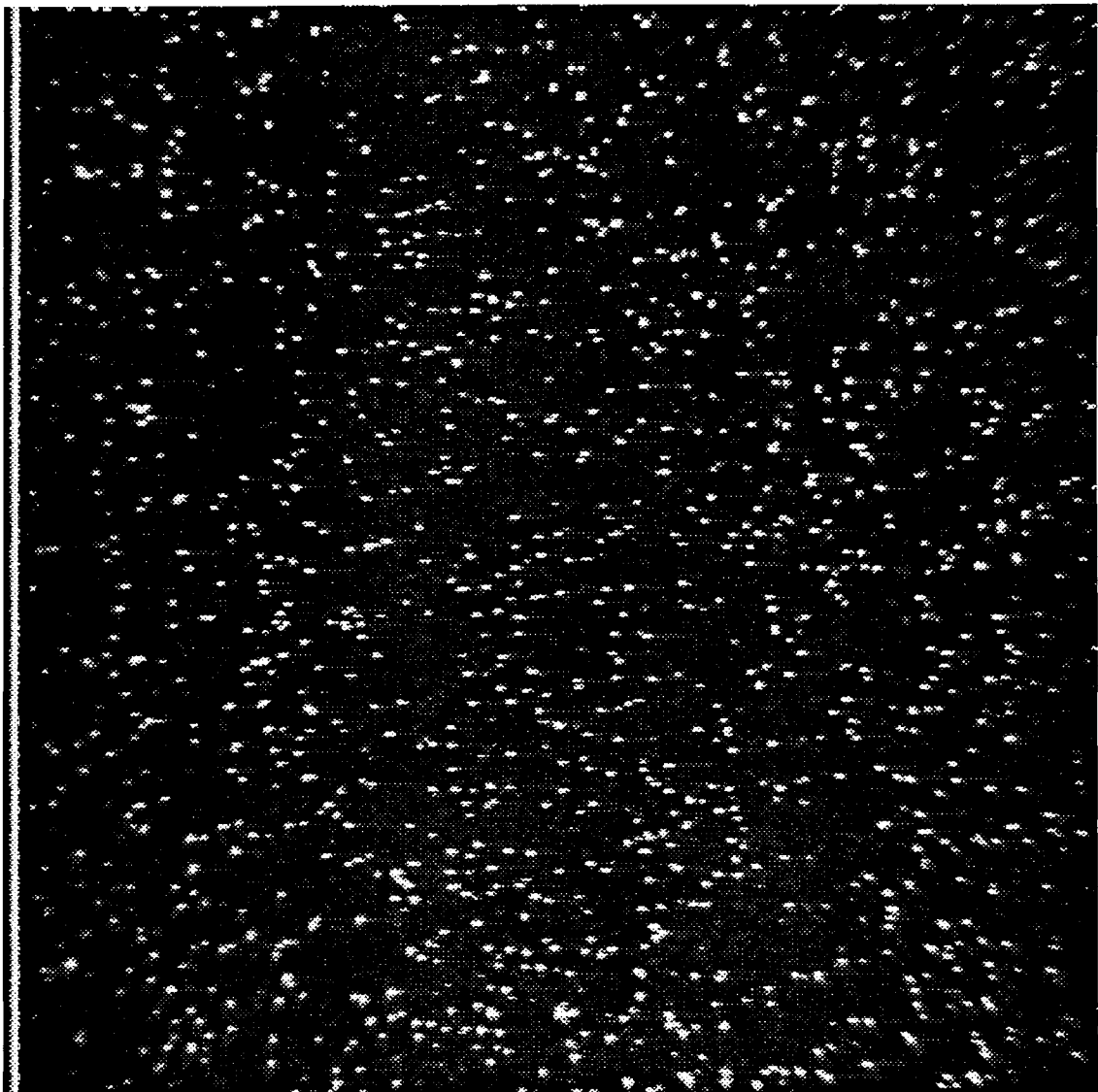


**Data acquisition system:
mobile installation at a laboratory channel
(4-camera system)**

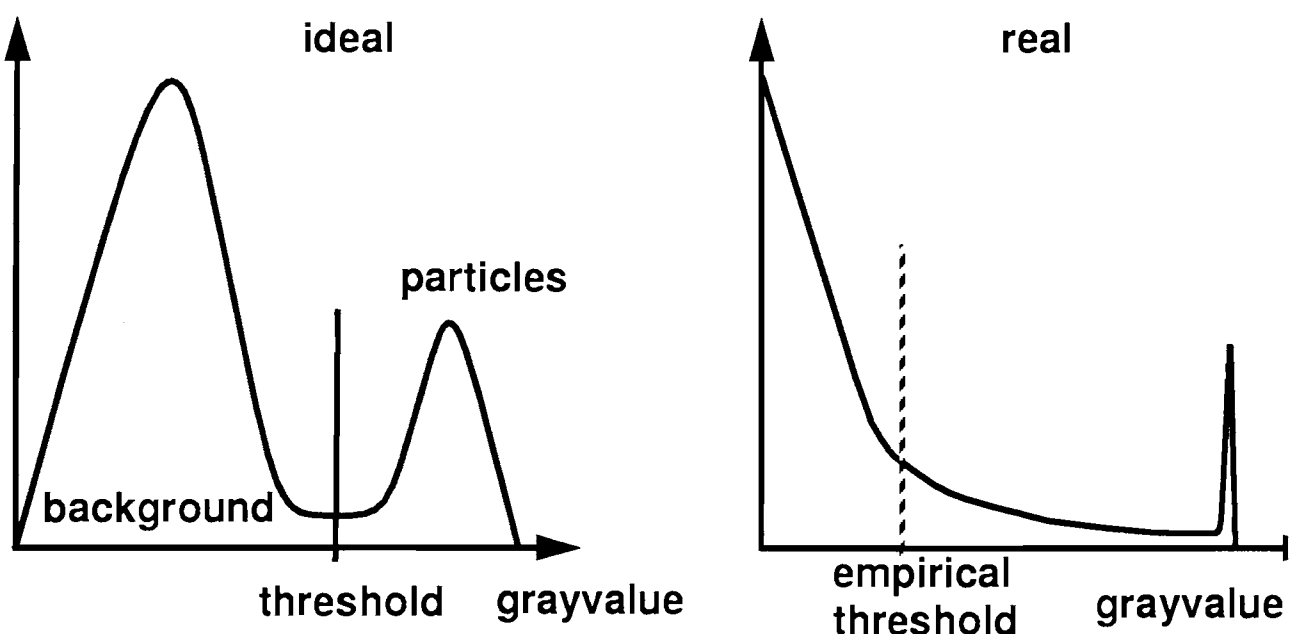


Example:

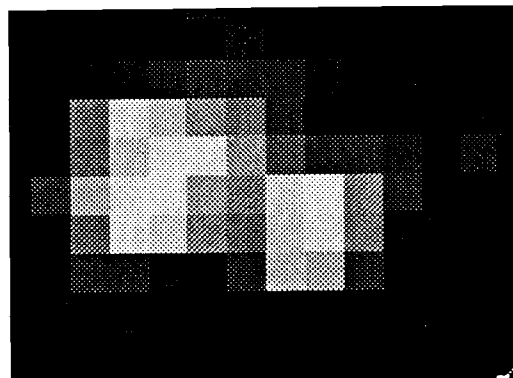
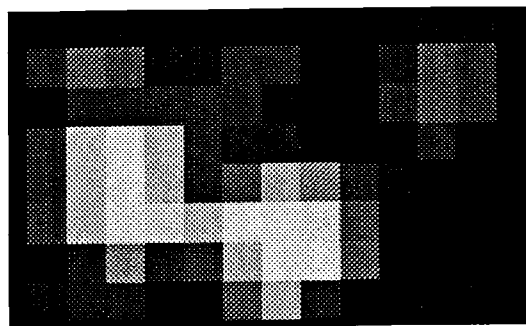
**ca. 1300 particles in digital image (512 x 512 pixel)
(turbulent channel flow)**



histograms



problem: occlusions

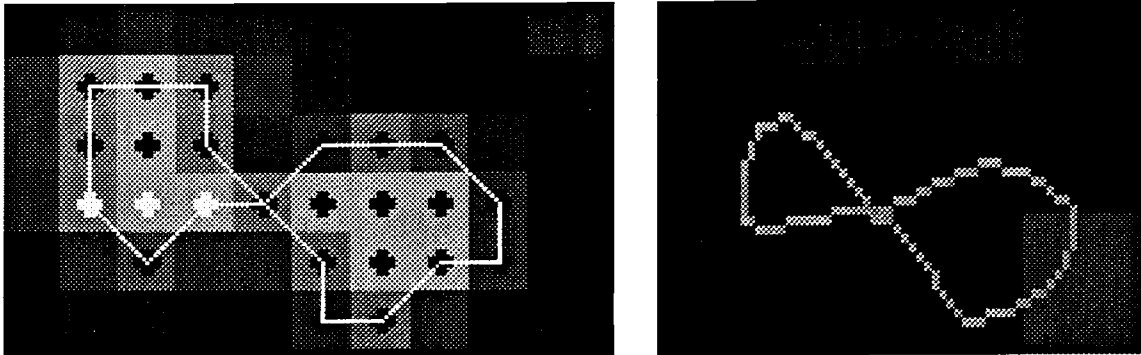


n_p	f	N_a
1000	10.0	74
2000	10.0	279
3000	10.0	596

$$N_a = N_a(f, n_p^2)$$

Detection and splitting of overlapping particle images

- Fourier-analysis of the contour line (-> characteristic taille)



- Invariant moments

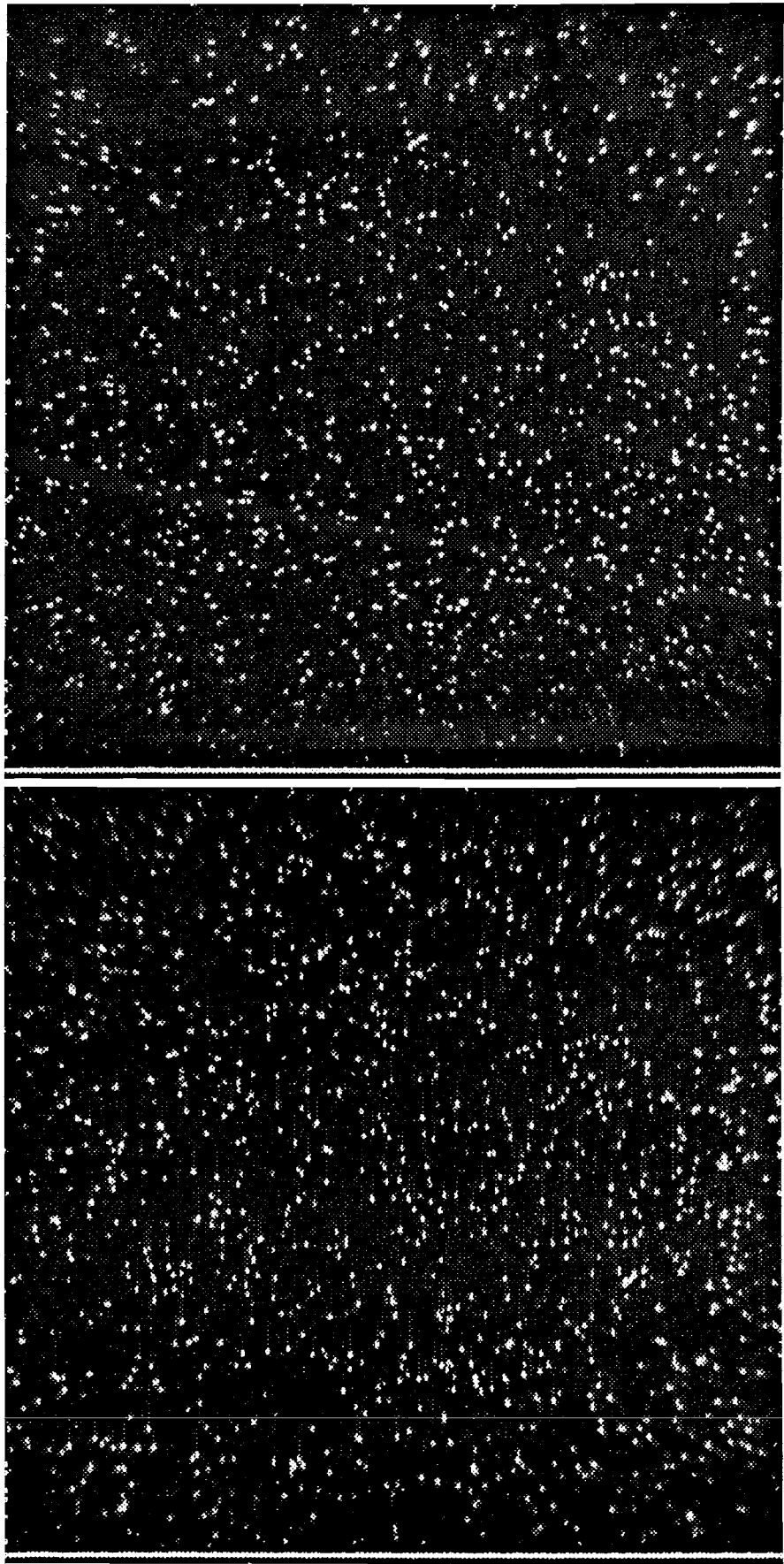
$$M_{kl} = \int_{-\infty}^{\infty} \int_{-\infty}^{\infty} x^k y^l g v(x, y) dx dy$$

- Differential operators, Hough-Transform, Voronoi-diagrams, morphological operators, template matching, ...
- Extended rule-based thresholding

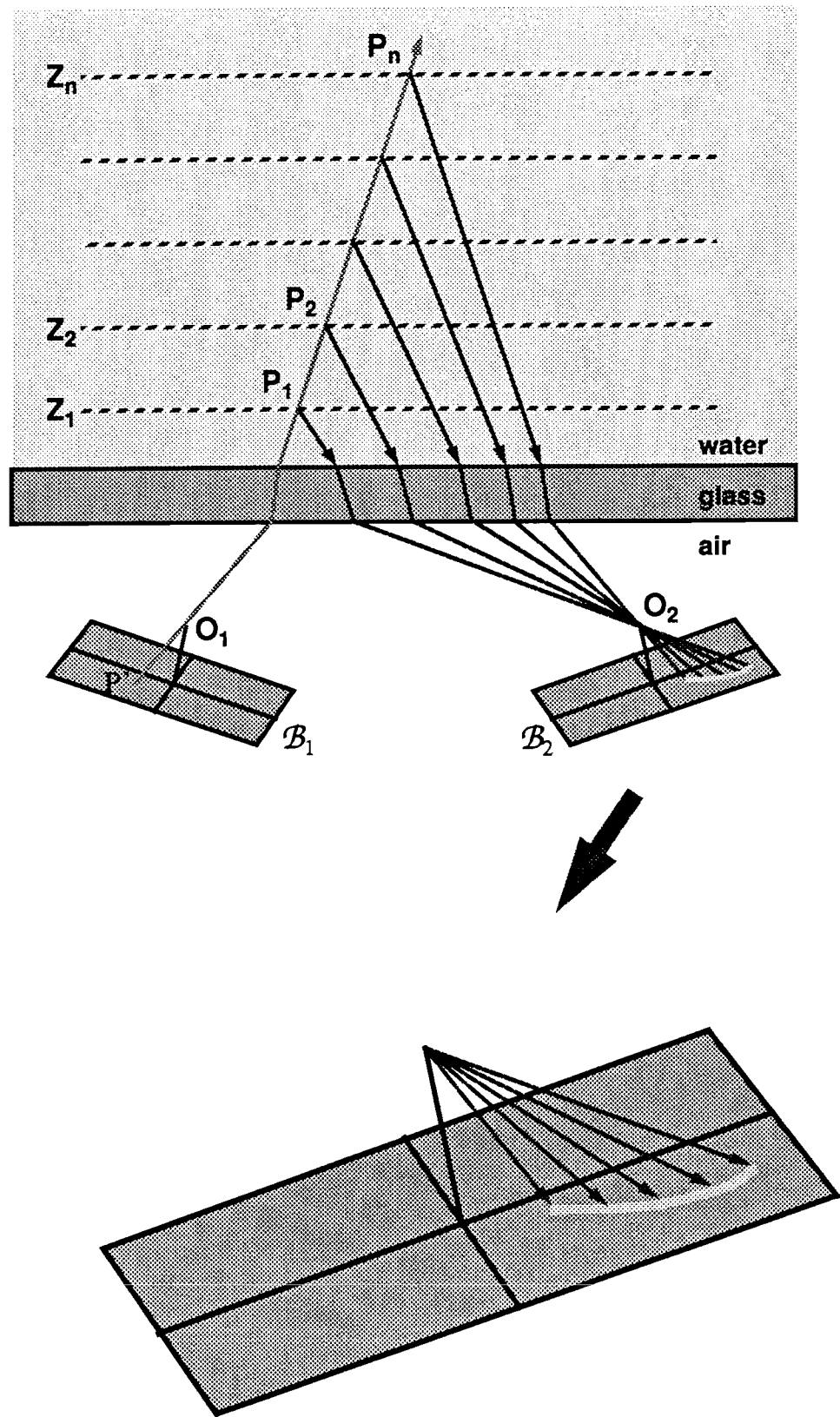
- the grayvalues of all pixels belonging to a particle image are above the threshold
- a particle image shows exactly one local maximum
- grayvalues drop continuously inside a particle image
- a pixel representing a local minimum, which can be attached to more than one neighbor pixels, is being attached to the neighbor pixel with the largest grayvalue

convergent stereopair

goal: establishment of stereoscopic correspondences

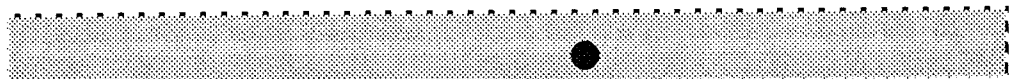


Epipolar lines in multimedia geometry

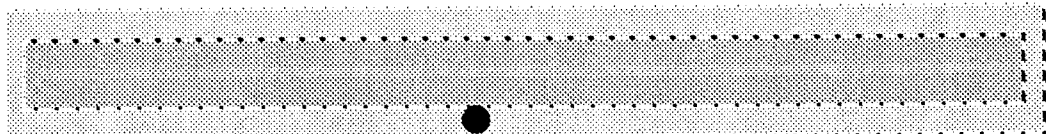


Candidate search in the epipolar search window

1.) exactly one candidate -> okay



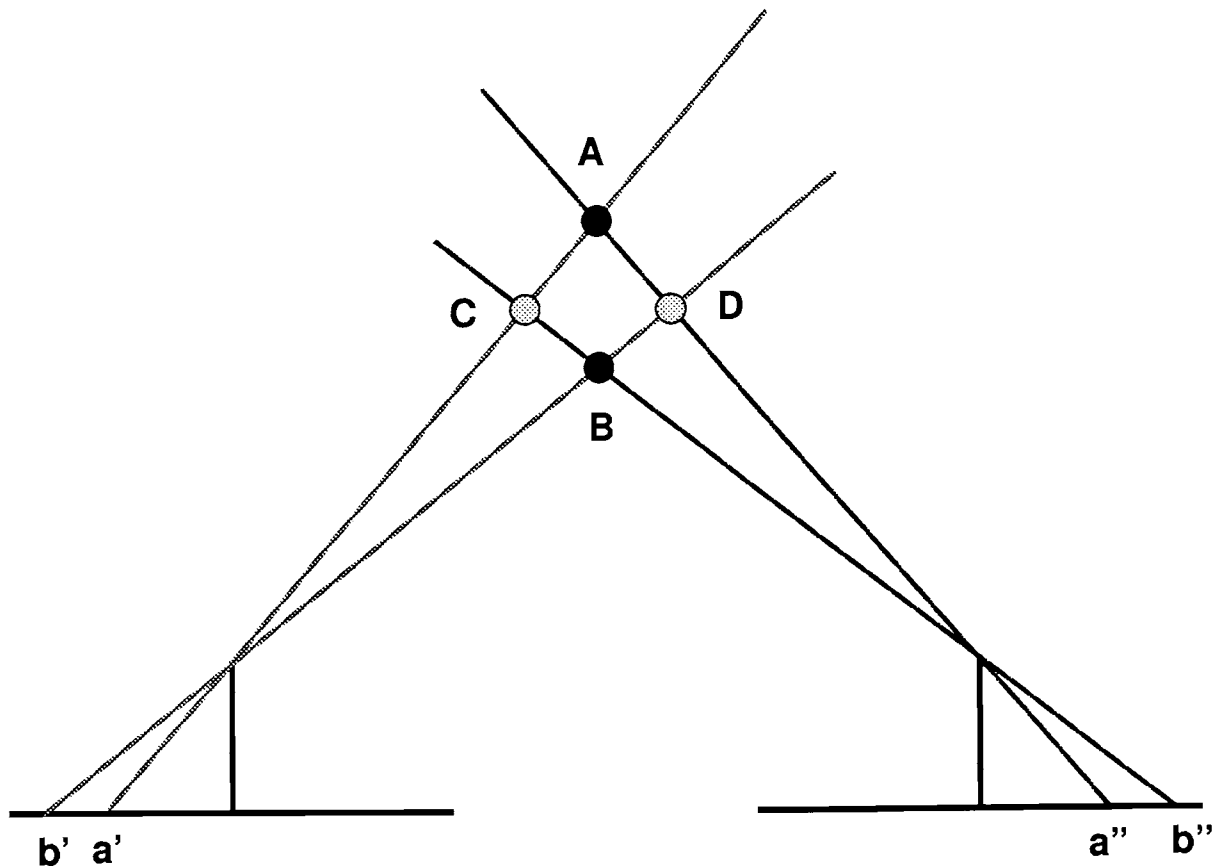
2.) no candidate -> enlarge tolerance



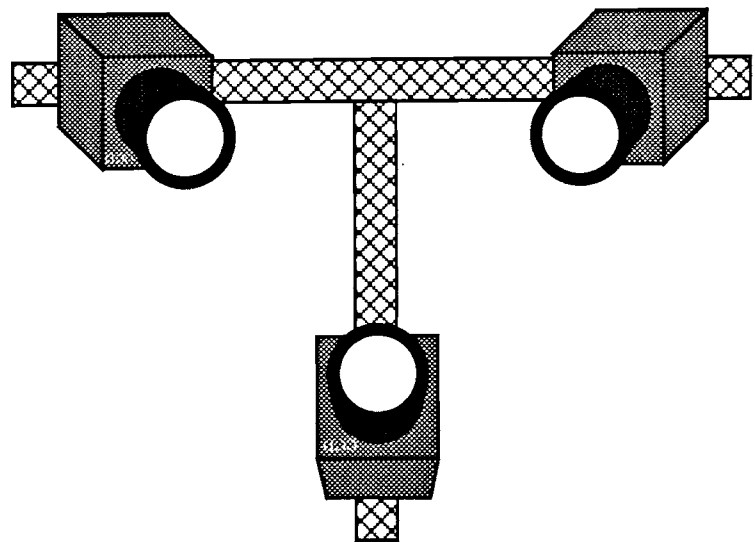
3.) two or more candidates -> ???



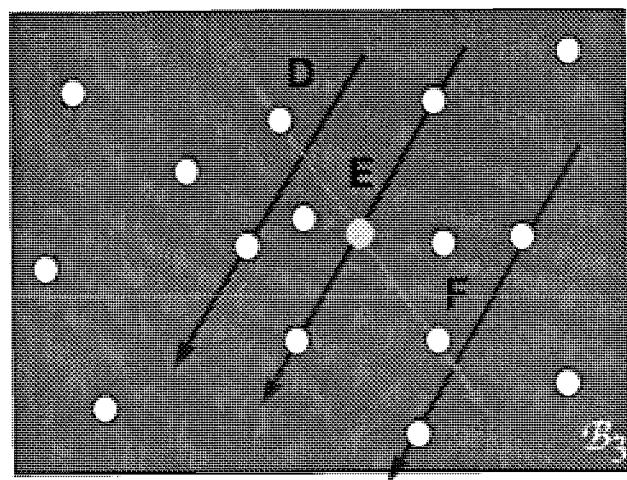
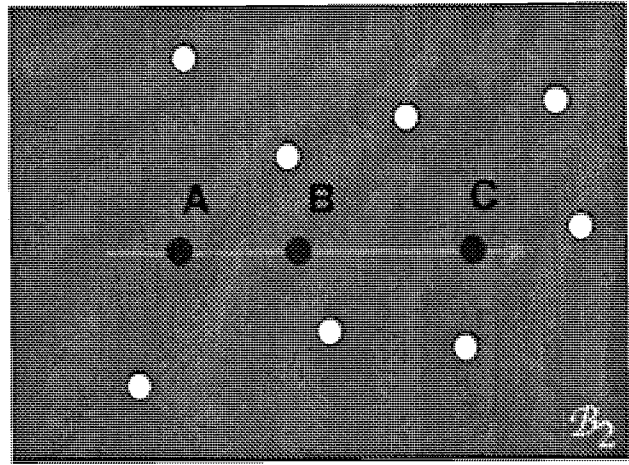
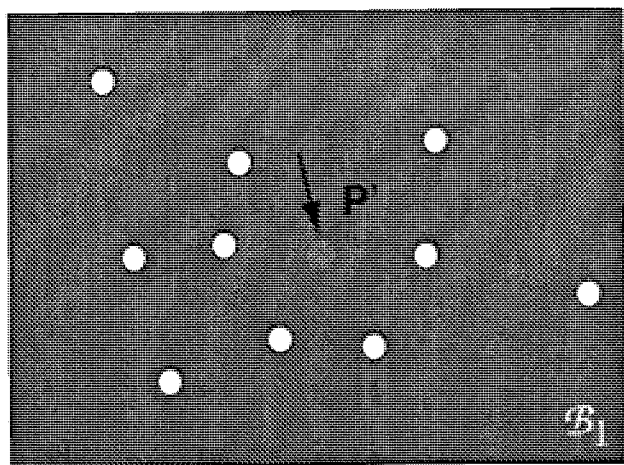
Example of unsolvable ambiguity in a stereo pair



Solution: Employment of a third camera



=> method of intersection of epipolar lines



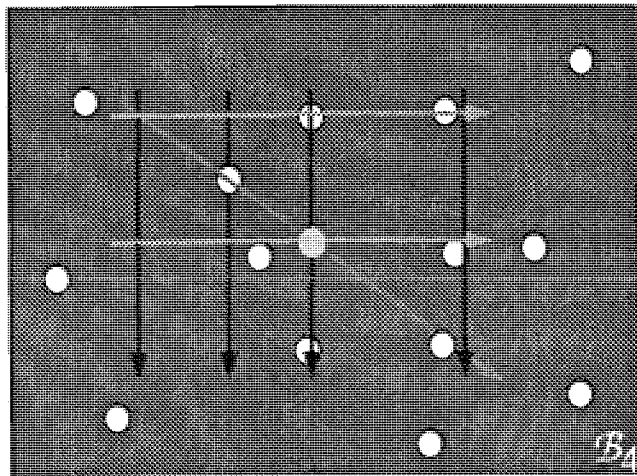
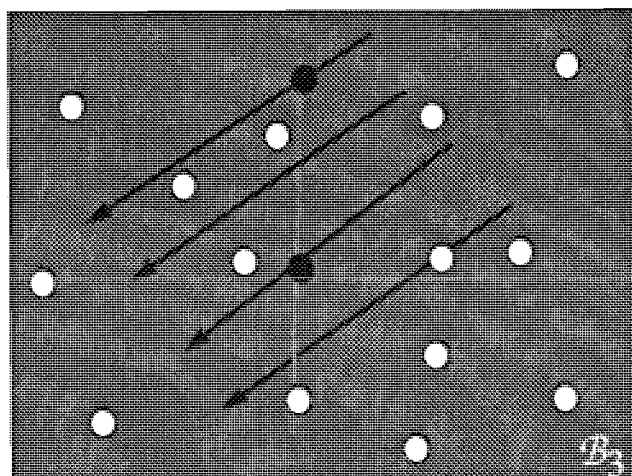
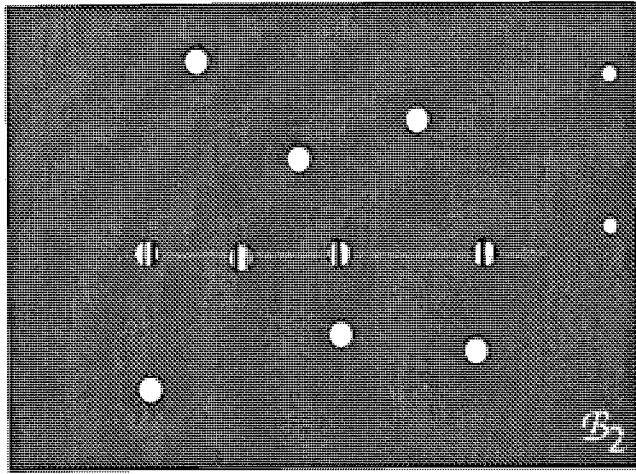
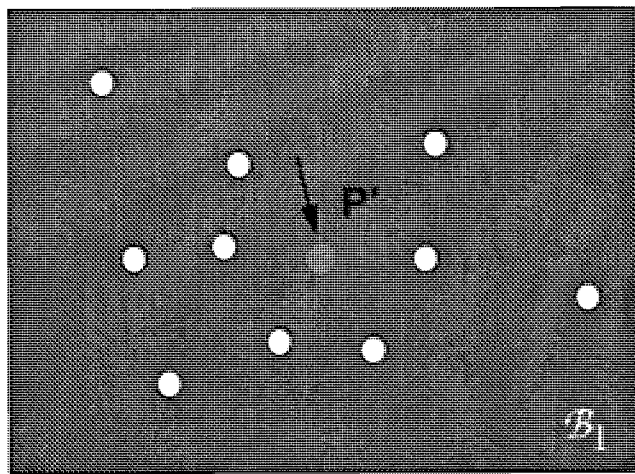
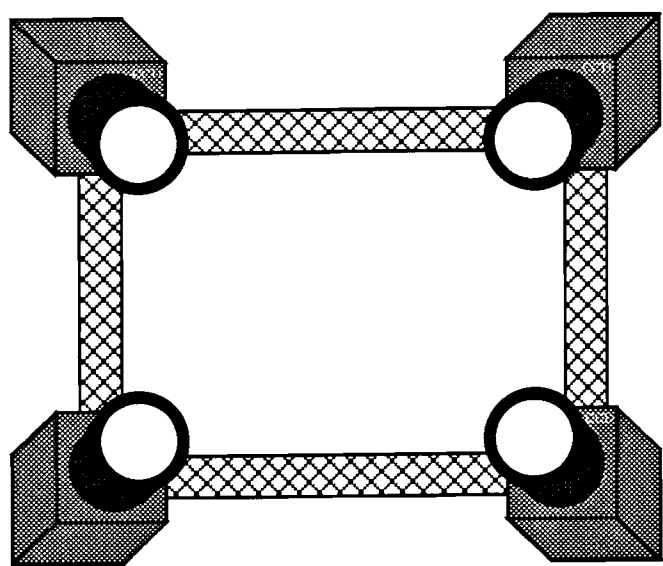
Probability of ambiguities:

# of particles	tolerance to epipolar line	ΔZ	ambiguities in 2-camera-system	ambiguities in 3-camera-system
1000	10 μm	40 mm	401	35
2000	10 μm	40 mm	1605	140
1000	5 μm	40 mm	201	9
1000	10 μm	80 mm	802	35
			$\Rightarrow f(n^2, \varepsilon, \Delta Z)$	$\Rightarrow f(n^2, \varepsilon^2)$

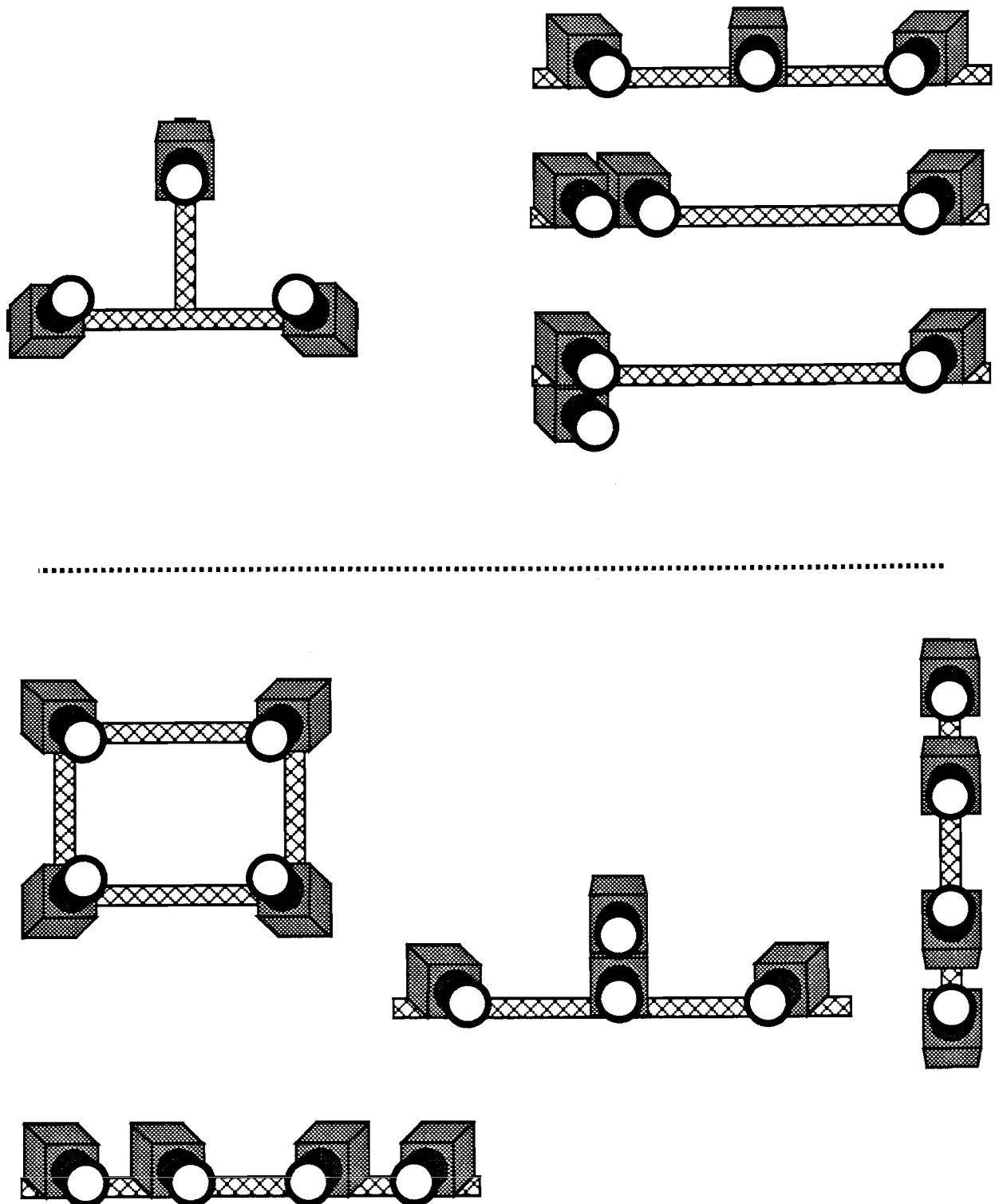
=> Advantages of a three-camera-system

- Reduction of the probability of ambiguities by at least one order of magnitude
- Independent on depth extension in object space
- Gain of accuracy

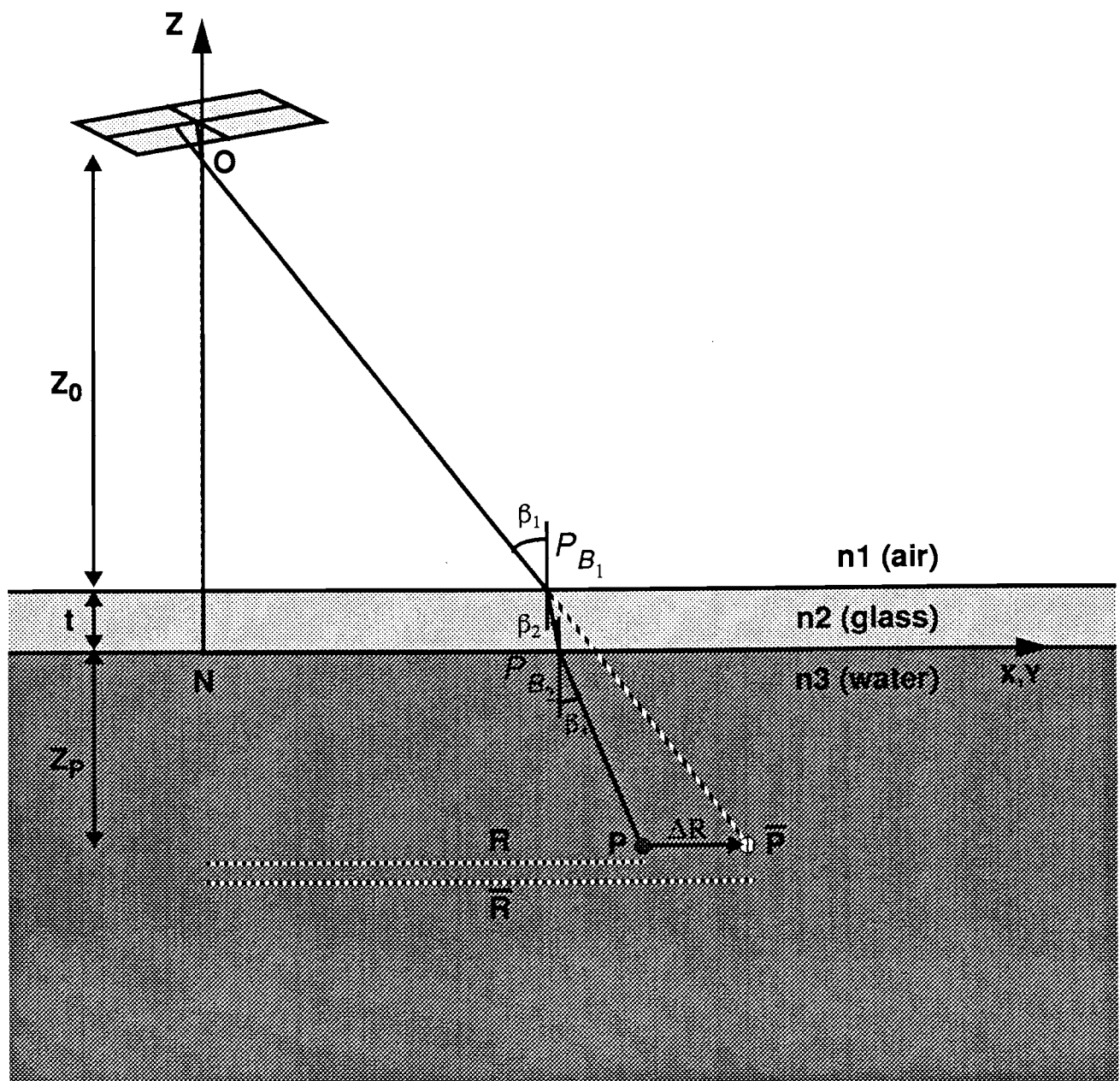
Further reduction of remaining ambiguities: 4-camera-system



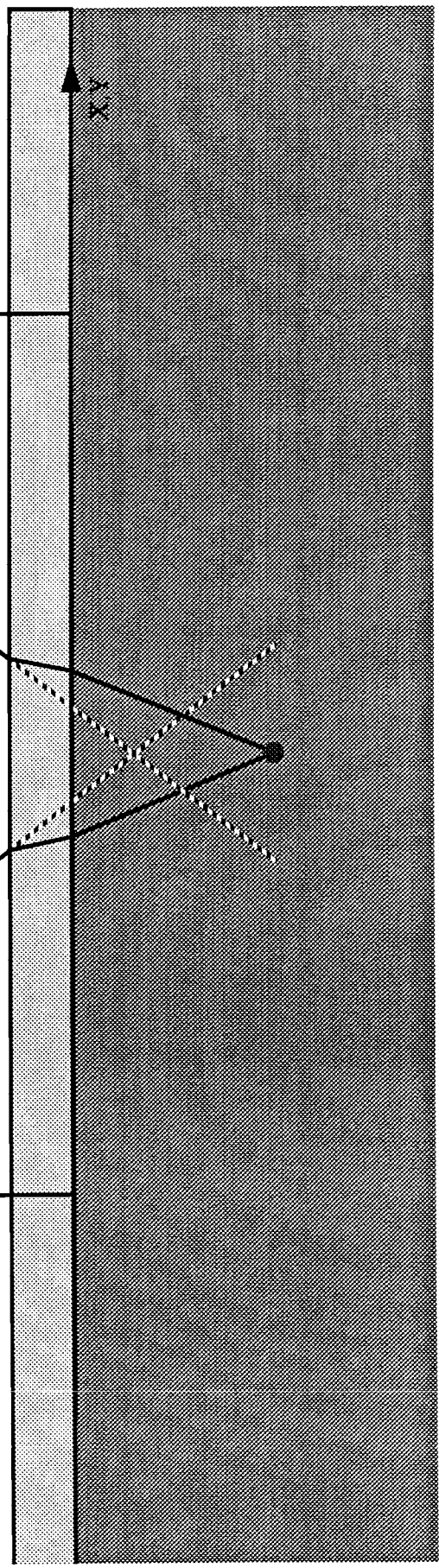
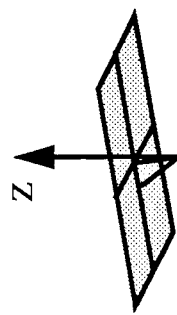
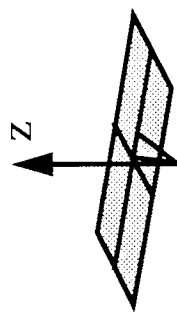
Selection of possible camera arrangements



Multimedia geometry

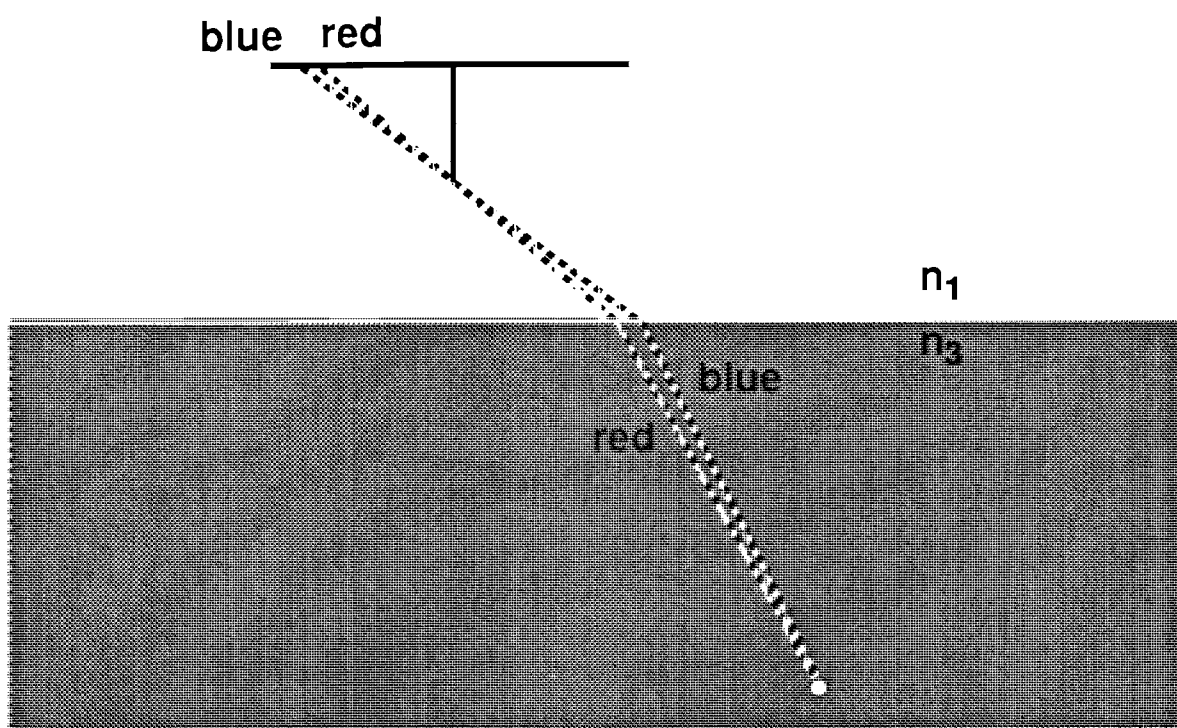


=> twice broken beam according to Snell's law



Effects of multimedia environment

- radial displacement with respect to the nadir point (strictly modelled)
- Aberration (asymmetric optical system *water - glass - air - lens*)
- Dispersion (variation of refractive index for blue \rightarrow red in water: 1,4%)

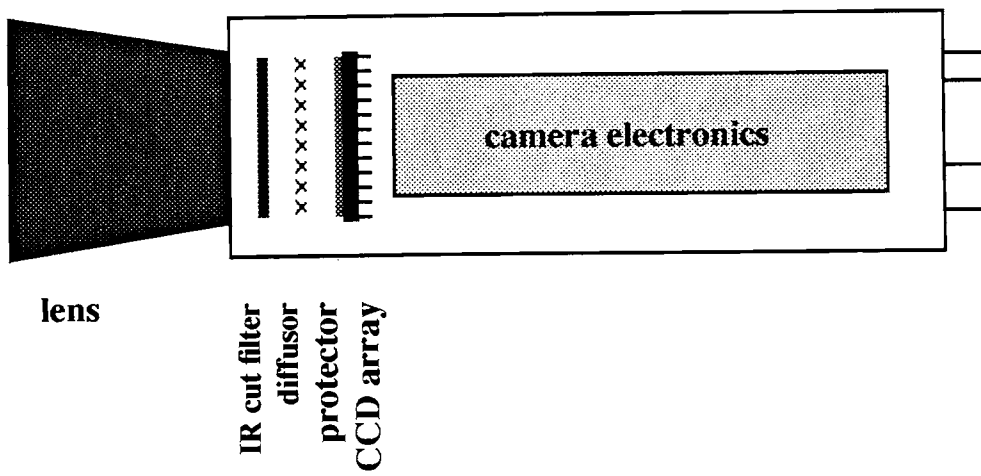


- Inhomogeneities of the refractive index
- Planeness of glass plates
- Network geometry (intersection angles)
- Diffusion and absorption (\rightarrow loss of contrast)

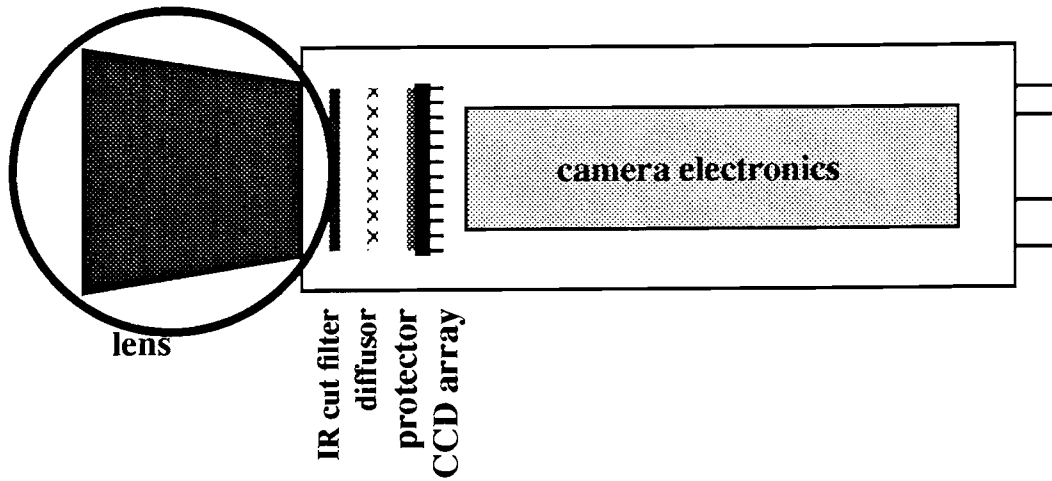
Calibration

Issues of calibration:

- Exterior orientation (projection center, direction of optical axis in space): only in testfield calibration or simultaneous calibration
- Interior orientation (camera constant, principle point): dependency on focussing, lens mounting, camera body temperature)
- lens / optics
- sensor
- data transmission and storage



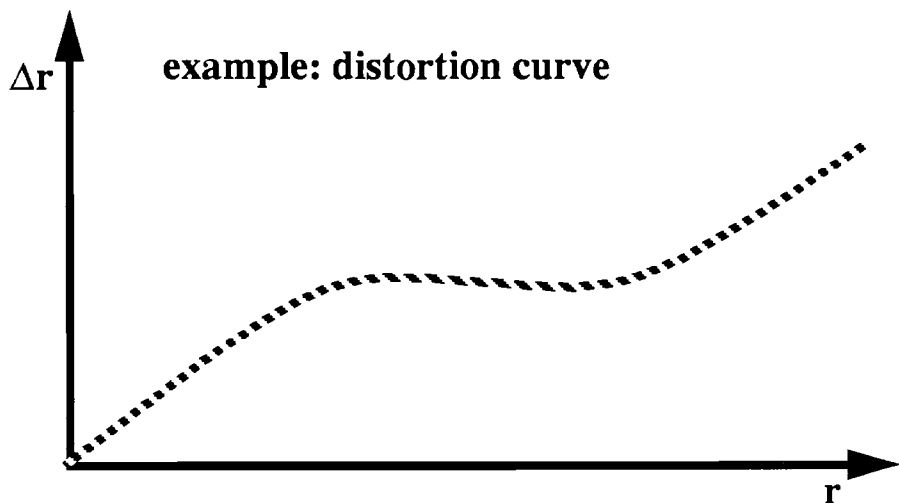
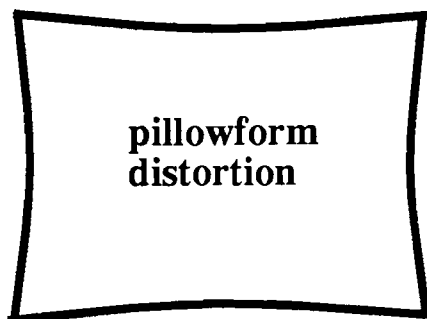
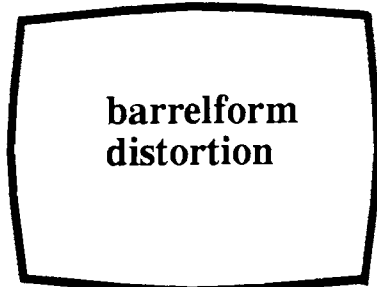
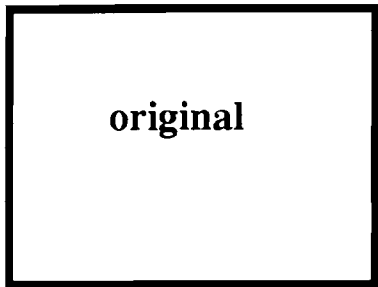
Lens:



Parameters influencing distortion

- **zooming**
 - **focussing**
 - **iris**
 - **(temperature)**
 - **shocks, damages ...**
-
- **radial distortion**
 - **decentering distortion**
(errors in the alignment of lenses on the optical axis)

effects of radial distortion:



Distortion correction:

- lookup-table (-> analytical plotter)
- additional parameters modelling distortion

common model: D. Brown

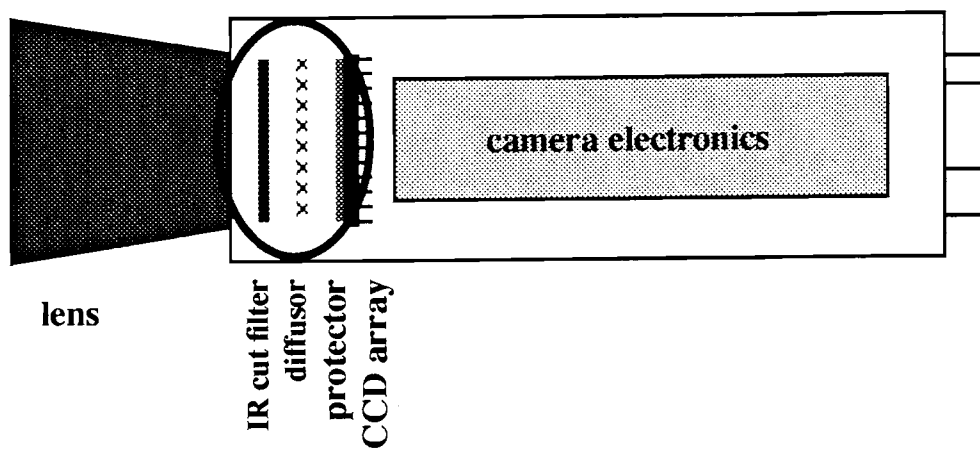
$$x'_i = x'_i + dx_i \quad y'_i = y'_i + dy_i$$

$$\text{with } dx_i = x'_i \cdot (k_1 r_i'^2 + k_2 r_i'^4 + k_3 r_i'^6) + p_1 \cdot (r_i'^2 + 2x_i'^2) + 2p_2 x_i' y_i'$$

$$dy_i = y'_i \cdot (k_1 r_i'^2 + k_2 r_i'^4 + k_3 r_i'^6) + 2p_1 x_i' y_i' + p_2 \cdot (r_i'^2 + 2y_i'^2)$$

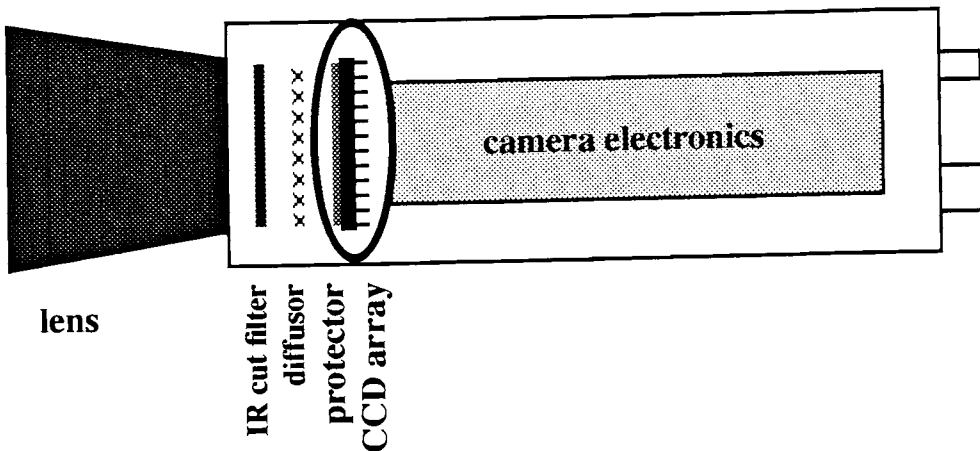
and $r_i'^2 = x_i'^2 + y_i'^2$ k_1, k_2, k_3 radial distortion
 p_1, p_2 : tangential distortion

Optical filters / diffusor / protector

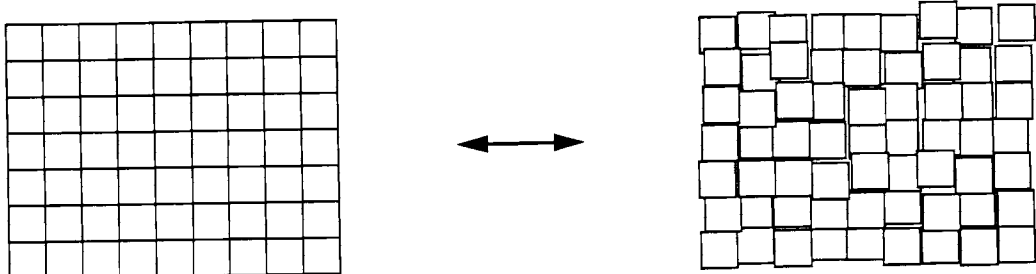


- must be plane and parallel with sensor plane
- radial effects (due to refractive index) contained in camera constant, when determined in simultaneous or testfield calibration
- IR cut filter manipulates radiometric characteristics

CCD-sensor geometry



- **pixel positions**



usually better than 1% of pixel spacing (i.e. ca. 100 nm)

- **sensor flatness (surface topography)**

usually not critical for standard CCD sensors, but might be a problem with high resolution CCDs

-> **sensor surface model?** (Advantage over film: surface topography can be considered stable)

-> **Réseau plate correction**

CCD sensor electronics

- transfer efficiency:

efficiency of charge transfer from one pixel to the next

reason: short time for charge transfer in combination with exponential charge decrease

today better than 99.9998%

-> transfer through 1000 pixels: $0.999998^{1000} \rightarrow 99.8\%$

- shot noise

due to statistical distribution of detected photons

$$\sigma = \sqrt{N_{e^-}}$$

-> $\sigma = 300 \text{ e}^-$, when max # $e^- = 100,000$

-> SNR = 300 : 1

- dark current noise

thermal generation of charges

grows exponentially with temperature

ca. 1000 e^- at room temperature -> $\sigma = \sqrt{N_{e^-}} = 30 \text{ e}^-$

-> limited max. image integration time (sensor full after 5 ... 50 sec)

-> cooled CCD sensors (integrate over hours, astronomy)

- read-out noise

noise generated in the readout process

50 ... 200 e^- for CCDs, more for CID, MOS structures

decreases only with \sqrt{T}

- static noise

different characteristics of neighbouring pixels (up to 1%)

causes fix pattern noise

can be calibrated by computing offset and gain for each individual

pixel from a dark and a uniformly bright image

- **dynamic range**

$$\frac{\text{max. signal}}{\text{min. noise}}$$

$$\text{CCDs: } \frac{100,000}{\sqrt{(3002 + 302 + 1002)}} = 250 \dots 300$$

newer MOS-sensors: up to 1000

- **linearity**

deviations from linearity (signal / input) of only 0.03% !

- **resolution**

penetration depth of photons

green $\rightarrow 1 \mu\text{m}$

near IR (800 nm) $\rightarrow 10 \mu\text{m}$

\rightarrow better resolution with blue light (standard CCDs)

- **blooming**

effect of local overexposure: charge flows into neighbouring pixels

\rightarrow sensors with anti-blooming (drainage into substrate)

- **smearing**

exposure during charge transfer (only for frame transfer CCDs)

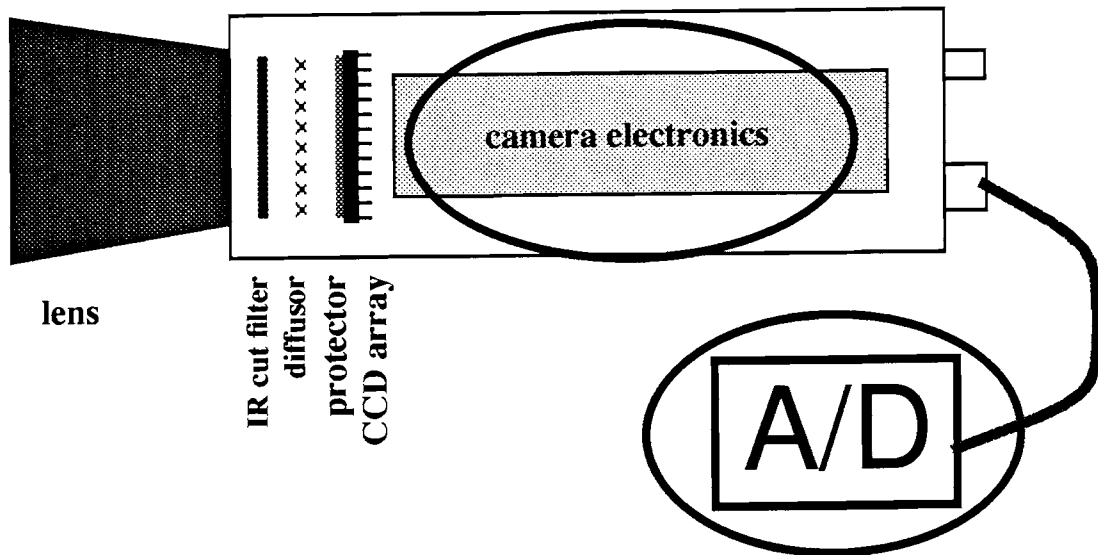
\rightarrow bright vertical stripes in the image

- **“dead” pixels**

defect pixels which give a constant white or black signal independent on the incident light

\rightarrow manufacturer specifications on number of dead pixels, for standard chips today often = 0

Video signal / frame grabbing



Distinguish:

- a.) pixel synchronous readout
- b.) h-sync generated on framegrabber board (i.e. camera synchronized by framegrabber)
- c.) h-sync derived from video signal

- Differences between camera pixel rate and framegrabber clock rate
-> scale factor in x' coordinate direction (subsampling, oversampling), except when using pixelclock

- Linejitter
error in h-sync detection of analog video signal, not stable in time
worst effect when h-sync has to be derived from video signal
(ca. 0.05 pixel rms with Matrox MVP framegrabber), effect almost vanishes when using pixelclock

compensation:

- a.) by imaging a vertical line in object space
- b.) by a vertical line on the sensor
- c.) by a vertical line electronically added to the video signal

=> more additional parameters:

$$\tilde{x}_i' = a_0 + a_1 x_i' + a_2 y_i' \quad \tilde{y}_i' = b_0 + b_1 x_i' + b_2 y_i'$$

$$\tilde{x}_i' = x_0 + s_x x_i' (\cos \alpha) - s_y y_i' (\sin (\alpha + \delta))$$

$$\tilde{y}_i' = y_0 + s_x x_i' (\sin \alpha) + s_y y_i' (\cos (\alpha + \delta))$$

or $a_0, a_1, a_2, b_0, b_1, b_2$: parameters of affine transformation
 $x_0, y_0, s_x, s_y, \alpha, \delta$

introduce only a_1 (x' - scale), b_1 (shear) resp. s_x, δ as unknowns

Further aspects

- **AGC (automatic gain control)**
changes radiometric characteristics
-> switch it off !
- **gamma correction**
due to non-linearity of TV-monitors, destroys linearity of signal
-> switch it off !
- **contour correction**
makes images look crisper for human perception (edge enhancement), but degrades signal
-> switch it off !
- **temperature**
warm-up effects of electronics (causes shifts of more than 1 pixel over the first 2 hours)
changes in camera body geometry
-> let camera warm up, keep surrounding temperature stable

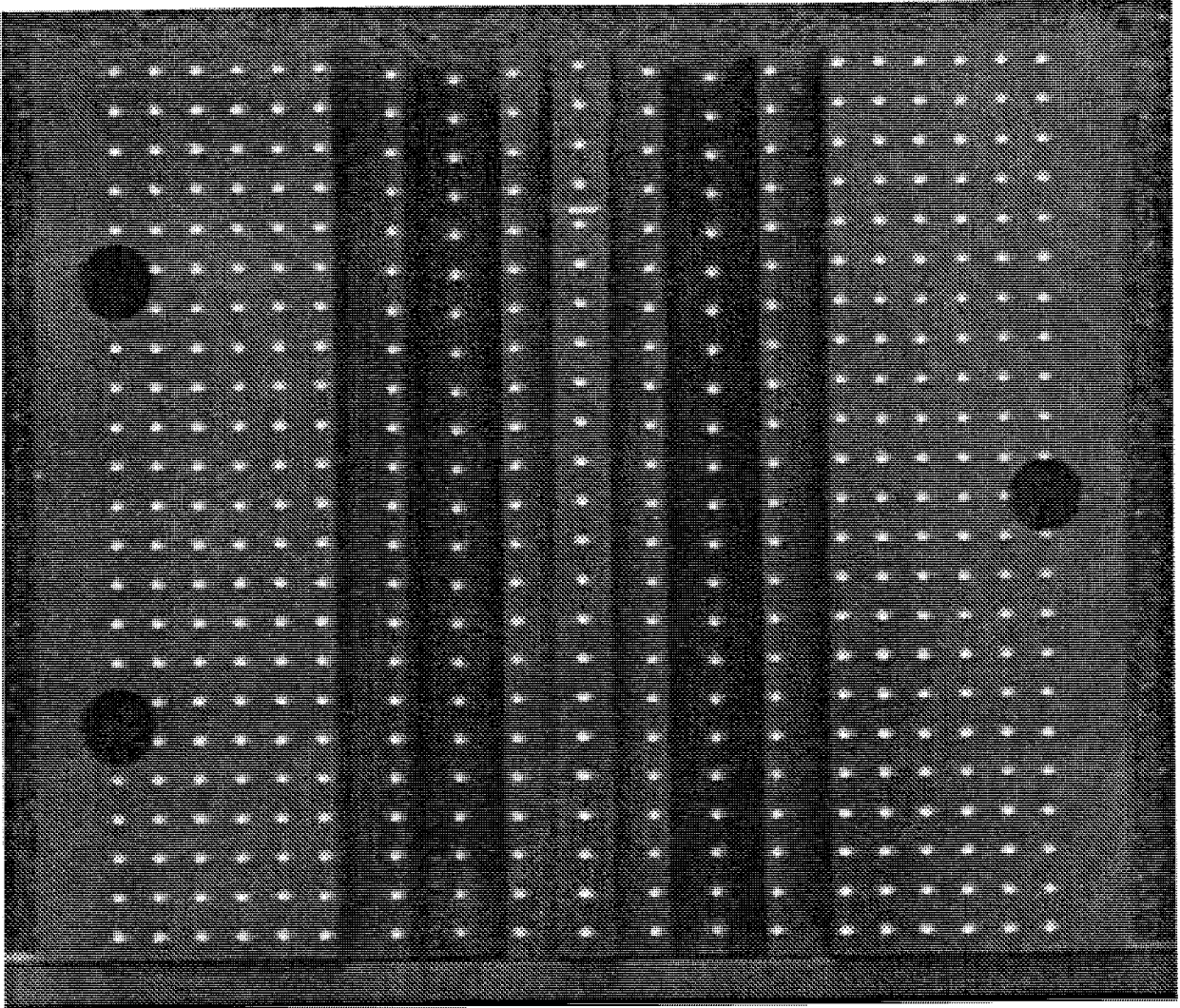
Calibration methods

- 1.) Laboratory calibration
- 2.) Testfield calibration
- 3.) Simultaneous calibration

Laboratory calibration

- advantages:
 - independent determination of calibration parameters
 - no calibration field required
 - disadvantages:
 - requires extensive laboratory equipment (goniometer etc.)
 - temporal stability of camera parameters often no guaranteed, camera parameters depend on focus, temperature, electronic and mechanical influences, ...
- rarely being used in digital close range photogrammetry

Testfield calibration



- **advantages:**

- stable network geometry**

- requires only few exposures (or even 1)**

- resection software sufficient**

- **disadvantages**

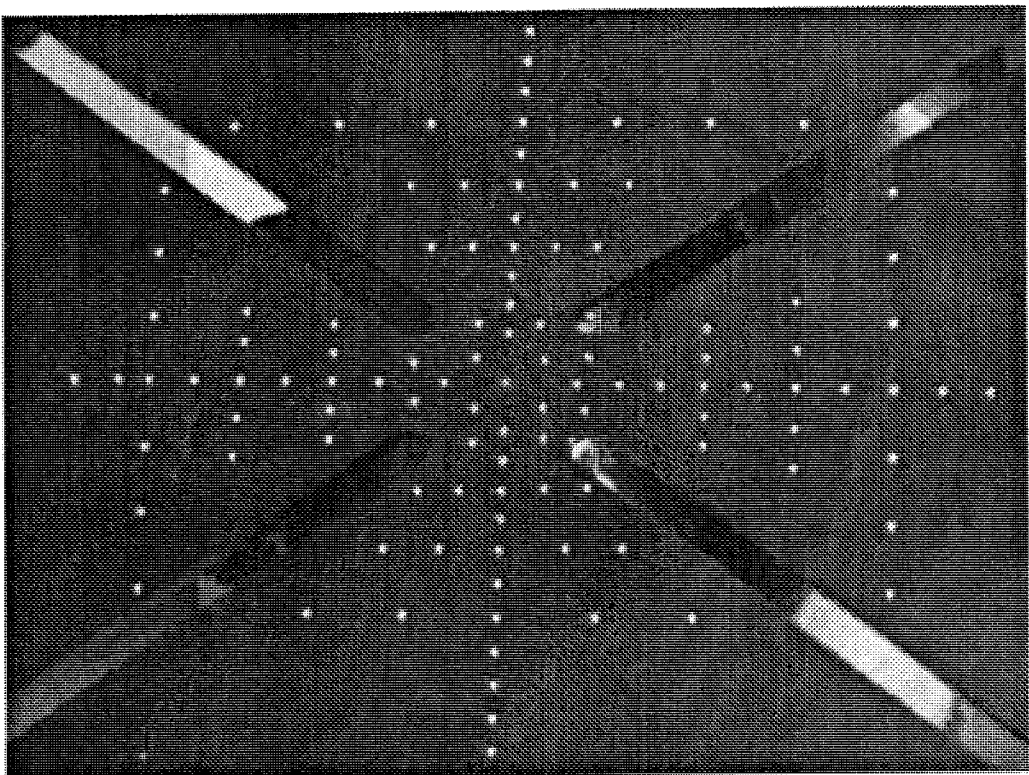
- testfield has to be very accurate and stable**

- testfield generation may be expensive**

- different tasks (scales) require different testfields**

Simultaneous calibration

idea: use a field of targets without the necessity of exact target coordinates, determine camera parameters and object coordinates simultaneously in photogrammetric bundle solution



- **advantages:**

- requires only a stable target field

- only rough approximate values of target positions are needed

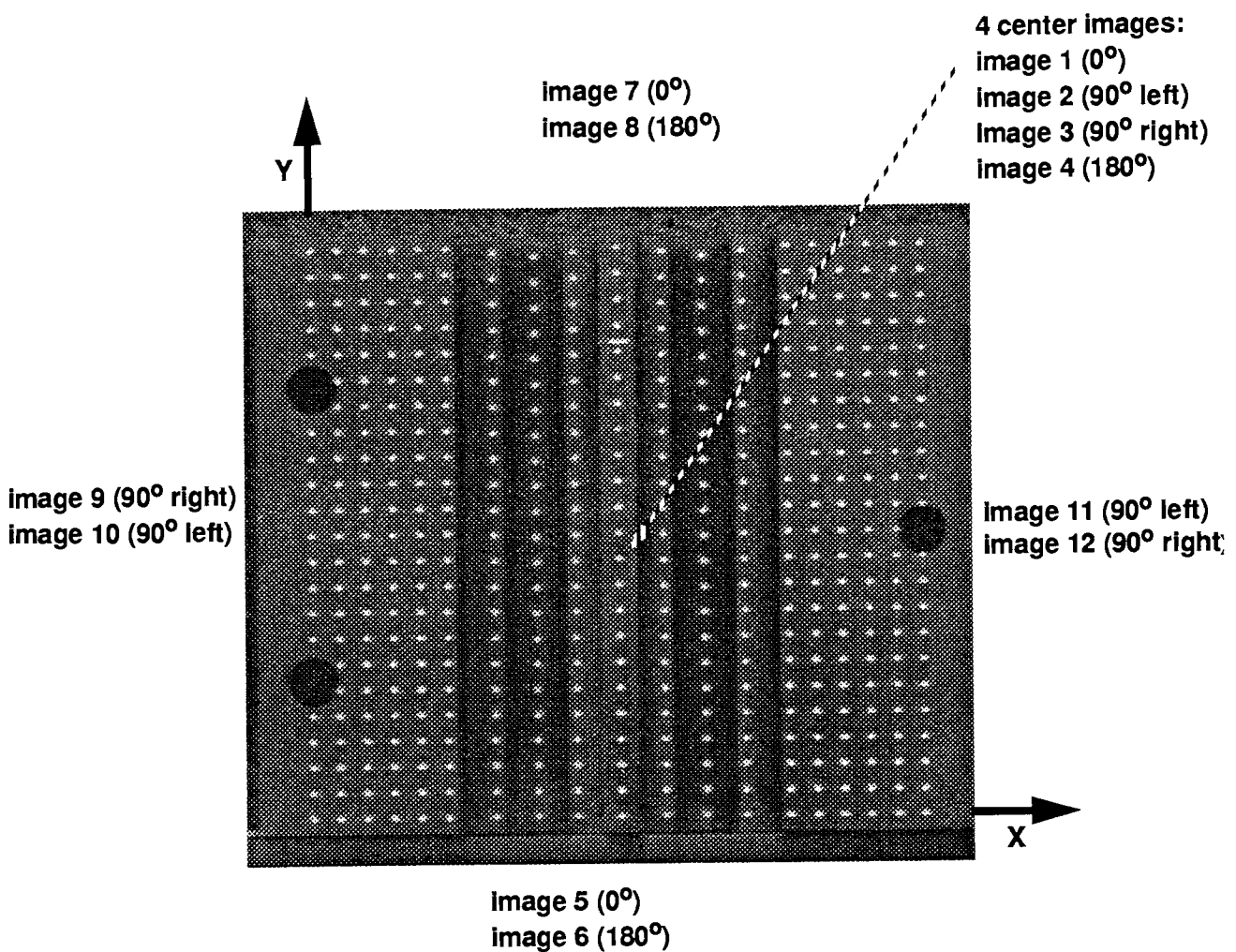
- **disadvantages:**

- requires a larger number of exposures at different camera orientations

- bundle adjustment software required

- correlations between unknowns may lead to model deformations

Example -> simultaneous calibration (1 camera)



camera and station parameters:

$X_0 = 26.651 \pm 0.046$
 $Y_0 = 12.567 \pm 0.046$
 $Z_0 = 227.097 \pm 0.056$
 $\omega = 6.0641 \pm 0.0153$
 $\phi = -2.5813 \pm 0.0156$
 $\kappa = 0.4846 \pm 0.0026$
 camera const = 17.78756 ± 0.00456
 $x_h = -0.14285 \pm 0.00279$
 $y_h = 0.15556 \pm 0.00270$
 $k_1 = -0.0002647 \pm 0.0000197$
 $k_2 = -0.0000060 \pm 0.0000022$
 $k_3 = 0.0000002 \pm 0.0000001$
 $p_1 = -0.0000485 \pm 0.0000028$
 $p_2 = 0.0000010 \pm 0.0000024$
 scale for x' = 0.9997263 ± 0.0000146
 shear [gon] = -0.0047464 ± 0.0006662

$\sigma_0 = 0.62$ micron (0.70 | 0.54)

(~ 1/20 pixel)

average standard deviations of point coordinates:

$s_x = 0.0034$ mm
 $s_y = 0.0033$ mm
 $s_z = 0.0114$ mm

(object size: ~ 90 x 70 x 12 mm³)

Additional option: simultaneous determination of the refractive index

Digital photogrammetric 3-D PTV -> potential

> True 3-D system:

all 3 components of velocity vector in a 3-D observation volume

> Up to 1000 particles simultaneously

(system with four standard-CCD-cameras)

> Accuracy potential:

relative accuracy of vector components ~ 1 : 4000

> Temporal resolution = image rate ($\frac{1}{25}$ sec with CCIR CCD-cameras)

variations:

high resolution CCD-cameras -> e.g. 2048 x 2048 pixel rather than 512 x 51

high speed CCD-cameras -> up to 1000 images/sec rather than 25

> Arbitrary sequence length (in case of analogue storage)

> Fully automatic system after initialization by the user

Particle Tracking Velocimetry in Three-dimensional Flows

- Part I: Photogrammetric Determination of Particle Coordinates -

Hans-Gerd Maas, Armin Gruen, Dimitris Papantoniou
Swiss Federal Institute of Technology
ETH - Hoenggerberg, CH - 8093 Zurich

Abstract:

Particle Tracking Velocimetry (PTV) is a well known technique for the determination of velocity vectors within a observation volume. However, for a long time it has rarely been applied because of the intensive effort necessary for measuring coordinates of a large number of flow marker particles in many images. With today's imaging hardware in combination with methods of digital image processing and digital photogrammetry, however, new possibilities have arisen for the design of completely automatic PTV systems. A powerful 3-D PTV has been developed in a cooperation of the Institute of Geodesy and Photogrammetry with the Institute of Hydromechanics and Water Resources Management at the Swiss Federal Institute of Technology. In this paper hardware components for 3-D PTV systems will be discussed, and a strict mathematical model of photogrammetric 3-D coordinate determination taking into account the different refractive indices on the optical path will be presented. The system described is capable of determining coordinate sets of some 1000 particles in a flow field at a time resolution of 25 datasets per second and almost arbitrary sequence length completely automatically after an initialization by an operator. The strict mathematical modelling of the measurement geometry together with a thorough calibration of the system provide for a coordinate accuracy of typically 0.06 mm in X,Y and 0.18 mm in Z (depth coordinate) in a volume of 200 x 160 x 50 mm³.

1. Introduction

3-D PTV is based on discrete visualization of flows with small, reflecting, neutrally buoyant tracer particles and a stereoscopic recording of image sequences of the particles marking the flow with the aim of determining 3-D coordinates of the tracers to derive their trajectories. Compared with competing flow measurement techniques, PTV shows some interesting advantages, as shown in Table 1.

Table 1: Comparison of performance features of some flow measurement techniques

	Hotwire	LDA	PIV	PTV
spatial resolution	low	low	very high	high
temporal resolution	high	very high	very low	low
velocity range	high	very high	very high	low
dimensions of observation volume	-	-	2	2-3
dimensions of velocity field	1-3	1-3	2	2-3
result	vectors	vectors	vectors	trajectories

While Hotwire-Anemometry and Laser-Doppler-Anemometry (LDA) allow for large temporal resolutions of a velocity measurement at a point and Particle Imaging Velocimetry (PIV, Adrian 1986) yields a very high spatial resolution of velocity vectors in a 2D observation sheet, 3-D PTV is a technique which allows the determination of a large number of long 3-D trajectories of discrete particles in a fully 3-D observation volume. The temporal resolution, however is limited to the imaging rates of solid state sensor cameras. Unlike other methods, PTV is based on the coordinate measurement and tracking of individual particles, which requires a reliable identification, multi-image matching, coordinate determination and multi-temporal matching of each individual particle. With large numbers of particles in the flow this process leads to ambiguities which cannot always be resolved, so that the spatial resolution of PTV will always be somewhat limited. Therefore, the main effort in the development of algorithms for a high resolution 3-D PTV must be focused on a careful handling of these ambiguities, which necessitates a strict geometric modelling of the multimedia environment, the use of at least three synchronous cameras imaging the flow and a thorough calibration of the system. Figure 1 shows a flow chart of such a system, whose components will be described in this article, except the tracking in object space and the 3-D interpolation, which will be addressed in part II of this publication (Malik et al., 1993):

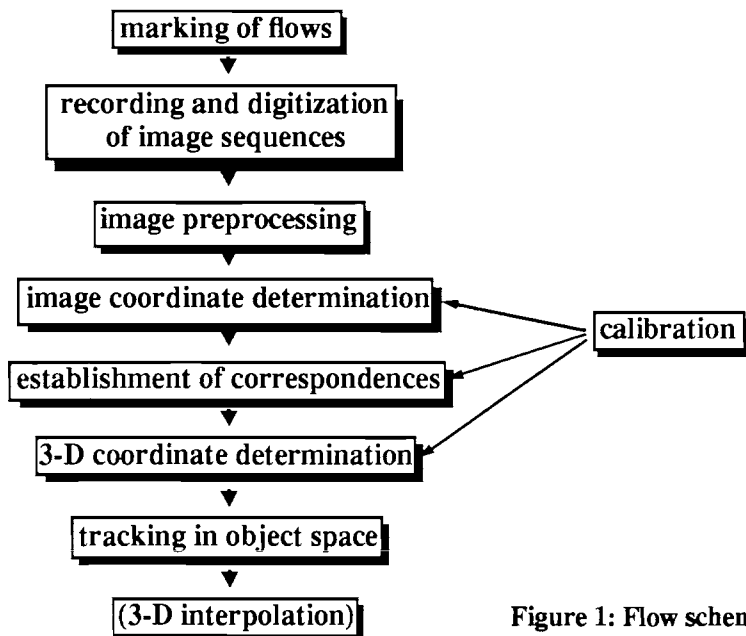


Figure 1: Flow scheme of 3-D PTV

2. Previous works

Though Particle Tracking Velocimetry is one of the oldest techniques of flow measurement, the acquisition of quantitative information with high density at a reasonable effort has only become possible in the last two decades. The methods and applications reported in literature show a transition from systems with completely manual data processing (i.e. a human operator measures coordinates and defines correspondences) towards completely automated systems. Besides the degree of automation the reported methods differ in the spatial and temporal information density achieved and the quality of the geometric modelling. Many of the methods are restricted to two-dimensional velocity measurements, while three-dimensional approaches often observe trajectories of only a few particles. Early applications use movie cameras or photos and pulsed illumination and the images are measured manually. Later users turned to digitization of film and automatic or semi-automatic image processing. Recent applications often use solid state sensor cameras, which allow on-line data processing.

An early application based on stereoscopic imaging is reported by Chiu and Rib (1956); their method requires manual measurements in the images. O. Jacobi (1980) reports a first application with strict photogrammetric modelling of the multimedia geometry; the evaluation is also performed manually, but Jacobi is working with only one particle at a time. Many systems use a Bolex stereo lens with two parallel optics arranged on a base which corresponds to the human eye disparity of about 65 mm imaging onto the left and right half of one film. Due to the parallel optical axis this lens can save some calibration effort, but the short baselength leads to very inhomogeneous accuracies of the three coordinates: the error in the depth coordinate will usually be by an order of magnitude larger than the error in the plane coordinates. Sheu et al. (1982) used such a lens to image particles in a volume of $200 \times 160 \times 15 \text{ mm}^3$; the manual measurement of 70 trajectories takes about 20 hours. Chang et al. (1985a,b) used similar equipment, but they digitize the film onto 2048×2048 pixels and apply simple image processing methods to derive the particle image coordinates. They achieve 92 trajectories with an estimated accuracy of $25 \mu\text{m}/25 \mu\text{m}/1046 \mu\text{m}$ in the X/Y/Z components. A system based on electronic imaging is presented by Adamczyk & Rimai (1988); they strictly limit the number of particles to avoid problems with unresolvable ambiguities and determine up to 16 trajectories. Koyabashi et al. (1989) use two CCD cameras to measure a flow between rotating disks and achieve an average of 51 simultaneous velocity vectors. An advanced development has been presented by a group at Tokyo University (Nishino & Kasagi 1989, Sata et al. 1989, Nishino et al. 1989, Kasagi & Nishino 1990). Nishino et al. have developed a completely automatic 3-D PTV, which allows the determination of up to 440 simultaneous velocity vectors.

The development of the 3-D PTV system described here started in 1987 (Papantoniou & Dracos, 1990a,b; Papantoniou & Maas, 1990; Maas, 1990). It is based on methods of digital photogrammetry and recording particle image sequences by three synchronized CCD cameras. It has been applied to the measurements of velocity fields in test volumes of $120 \times 120 \times 15$ to $200 \times 200 \times 40 \text{ mm}^3$ seeded with about 1000 - 1500 particles in a 24 m laboratory channel and in a stirred aquarium.

3. Hardware

The hardware components of a 3-D PTV system consists of flow markers, an illumination facility, an imaging system, an image digitization and storage unit and a data processing unit. In order to reduce costs it is desirable to use off-the-shelf components as far as possible.

3.1 Flow markers:

To visualize a flow for PTV it has to be seeded with small, neutrally buoyant tracer particles. The physical density of the particles should correspond to the one of the flow medium and their size should be as small as possible to guarantee for good follower behaviour, but large enough to be made visible by suitable illumination. Their shape should be spherical and the surface should be reflecting to maximize the amount of scattered light. In the experiments described here Pliolite particles (Goodyear Chemical) with mean diameters of either 50 or 200 μm were used. Pliolite particles are not perfectly spherical in shape, but their reflection properties proved to be good.

3.2 Illumination

One of the most important parts of the hardware configuration is the illumination system. To get sufficient signal from small, moving particles in an extended 3-D observation volume a light source is necessary which fulfills the following requirements:

- High intensity to enable the use of small tracers.
- The light source should be a point light source, which makes it easier to shape the light output to a 3-D lightsheet collecting the whole output into the desired test volume via an optical system without iris elements blocking the light.
- To reduce motion effects the light source should be pulsed synchronously with the cameras in frequency and in phase.
- The emission spectrum should match the sensitivity spectrum of the imaging sensors (with a maximum in the red if solid state sensors are used).
- Homogeneous intensity distribution to ensure uniform illumination of the whole observation volume.

Light sources often used in PTV systems are:

- Lasers: They offer the advantage of a monochromatic light source and their beam can be shaped into a 3-D lightsheet without excessive loss of energy. Disadvantages are the gaussian intensity profile of the beam and the costs (for example the illumination of a 200 cm^3 volume with 50 μm Pliolite particles requires a 5W Argon-Ion Laser).
- Strobelights: They operate in very short pulses and are more flexible than lasers. The energy per pulse however is often too small.
- Lamps with continuous emission: They reduce costs and show often better intensity distributions as compared to strobes. The pulsing however can only be performed by mechanical shuttering of the beam or electronic shuttering of the cameras; both options lead to a linear loss of light energy.

Fiber optics mouthpieces enable versatile shaping of the beam to achieve an optimal lightsheet

with almost rectangular intensity profile.

3.3 Cameras

Only cameras with solid state sensors are suitable if an automatic on-line data processing is envisaged. Tube cameras show larger geometric instabilities and drift behaviour. Film still offers higher resolution but the processing and digitizing of film is usually too time consuming.

Different kinds of solid state sensor cameras can be considered:

- Black-and-white CCD cameras with consumer electronics video norms (CCIR 25 img/sec, NTSC 30 img/sec) mean minimum cost, offer high flexibility and are compatible with many display and storage devices. Typical sensors have respectively 756 x 581 pixels (CCIR) and 768 x 493 pixels (NTSC). The interlacing of the video signal causes some problems, if moving objects need to be imaged with full spatial resolution, which can be circumvented if an interline transfer type camera is used in combination with an appropriately pulsed light source.
- High resolution cameras offer sensor sizes up to 2048 x 2048 pixels, but at lower temporal resolution and at much higher costs.
- High Speed cameras offer imaging rates of up to 1000 images per second, but at reduced spatial resolution (e.g. 1000 img/sec with 240 x 192 pixels) and also high costs.
- Intensified cameras can operate at very low light levels and usually come with standard video norm. Due to the intensifier tube and the fiber connection to the CCD chip the image quality is reduced.

3.4 Camera Lenses

CCD cameras usually have a standard C-mount, which offers a wide variety of lenses with focal lengths of 3.5 to 1200 mm. Macro and close-up lenses may be interesting for imaging small volumes, but the reduced depth of focus has to be considered.

3.5 Image digitization and storage

A wide range of framegrabbers are available for the A/D-conversion of standard video signal, some of them with interesting additional features like real-time low level image pre-processing. High resolution and high speed cameras usually have their own computer interfaces.

As the processing of the PTV image data will not be possible in video real-time in most cases, image sequences have to be stored. The high data rates (standard video ca. 11 MByte/sec, high resolution or high speed systems up to 46 MByte/sec) pose severe problems, especially when three or four cameras are used simultaneously. A storage on standard computer harddisks in real-time is generally impossible. The following options can be chosen:

- Real-time disks: Disk arrays with a special controller distributing the data on many single disks. Data rates and storage capacities are large enough for all imaginable systems, but costs are high.
- RAM-storage offers data rates, which are comparable with real-time disks, but with lower storage capacities.
- Analogue videorecorders (one per camera) can be used only for standard CCD cameras or

intensified cameras. The storage capacity on video-tape is very large, the costs are low, but the analogue storage leads to a certain degradation of the image quality. To allow the digitization of synchronous image sequences from more than one videorecorder, a time code has to be supplied to the images before storage.

- Analogue videodiscs also offer large storage capacities, but at higher costs for the device and the disks (write once). The larger bandwidth as compared with videorecorders means less image quality degradation. Unlike videorecorders, videodiscs offer random access to images.

3.6 Implementation at ETH Zurich

The configuration of the 3-D PTV implemented at ETH Zurich is shown in Figure 2. The system consists of three or four interline transfer CCD cameras, a 5W Argon-ion laser with a zoomline projector for the illumination of an extended 3-D testvolume and U-matic videorecorders for analogue image sequence storage. A pattern generator generates a binary pattern as a code for the sequential image number, which is added to the videosignal before storage to allow for the recognition of corresponding images on the three or four video tapes. The flow is imaged through a glass section of the channel bottom. Both imaging and illumination system together can be moved with average flow velocity on a carriage parallel with the channel bottom. After recording of a full experiment image sequences are digitized from all videotapes by a PC equipped with a framegrabber board with RAM storage for only 4 images and a board giving access to the remote control port of the videorecorder. By playing the recorder, continuously grabbing images and evaluating the binary code pattern (which is easily possible from the running video-tape in real-time), digitizing 4 images, writing them to harddisk, rewinding the tape, playing it again, tracing the image number pattern and digitizing the next 4 images, etc., image sequences of arbitrary length can be digitized completely automatically from all tapes. Data processing is computationally very intensive and should be performed on a powerful computer workstation.

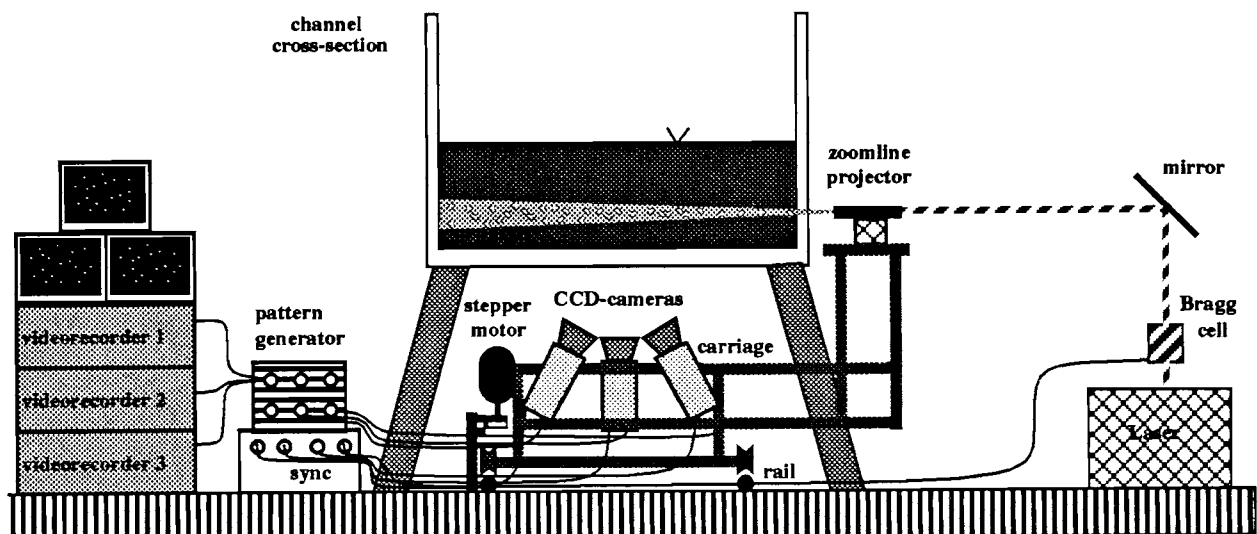


Figure 2: Hardware installation at laboratory channel

4. Mathematical Model

The fundamental mathematical theorem of photogrammetric 3-D coordinate determination is the collinearity condition (Figure 3, eq.1), which states that object point, camera projective centre and image point lie on a straight line.

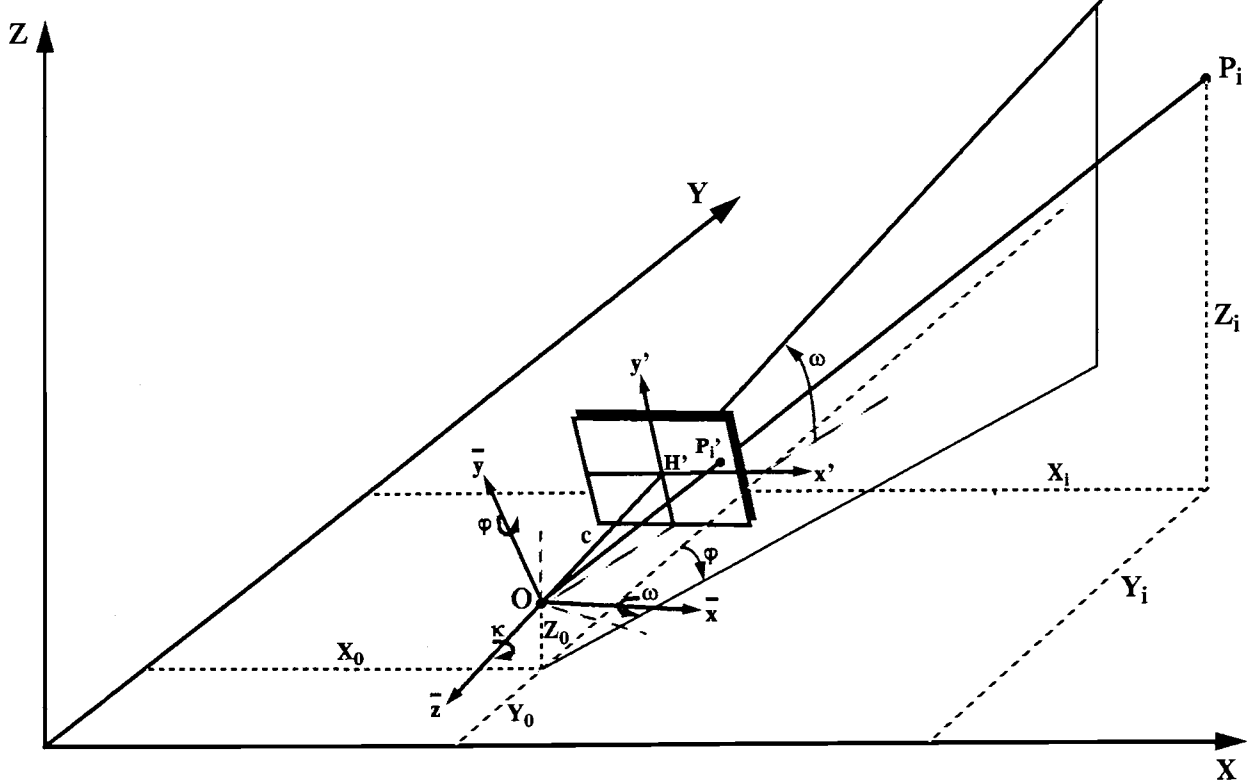


Figure 3: Collinearity condition (camera model inverted for drawing purposes)

$$\begin{bmatrix} x'_i - x_h \\ y'_i - y_h \\ -c \end{bmatrix} = \lambda_i \cdot R \cdot \begin{bmatrix} X_i - X_0 \\ Y_i - Y_0 \\ Z_i - Z_0 \end{bmatrix} \quad (1)$$

- (X_i, Y_i, Z_i) : object point coordinates
 - (X_0, Y_0, Z_0) : camera projective center coordinates
 - $R = r_{ij}$: elements of 3x3 rotation matrix with angles ω, φ, κ
 - (x'_i, y'_i) : image coordinates
 - (x_h, y_h) : image principle point
 - c : image principle distance
 - λ_i : scale factor
- } camera exterior orientation
- } camera interior orientation parameters

To serve as observation equations in a least squares adjustment for the determination of the unknown parameters (camera orientation $X_0, Y_0, Z_0, \omega, \varphi, \kappa, c, x_h, y_h$ in the calibration, object coordinates X_i, Y_i, Z_i in the particle positioning), equation (1) has to be solved for the image coordinates:

$$x'_i = x_h - c \cdot \frac{r_{11}(X_i - X_0) + r_{21}(Y_i - Y_0) + r_{31}(Z_i - Z_0)}{r_{13}(X_i - X_0) + r_{23}(Y_i - Y_0) + r_{33}(Z_i - Z_0)} \quad (2)$$

$$y'_i = y_h - c \cdot \frac{r_{12}(X_i - X_0) + r_{22}(Y_i - Y_0) + r_{32}(Z_i - Z_0)}{r_{13}(X_i - X_0) + r_{23}(Y_i - Y_0) + r_{33}(Z_i - Z_0)}$$

This mathematical formulation has to be extended to meet the physical realities. One has to consider the fact that each ray from a particle to the sensor passes the three optical media water, glass and air with different refractive indices, which causes a twice broken beam to be handled in the collinearity equation. Furthermore, the image coordinates have to be corrected for effects of lens distortion and effects of the digitization

4.1 Additional parameters for systematic image deformation

The effects caused by lens distortion (e.g. barrel or pillow form distortion) and image digitization are usually compensated by a set of additional parameters, which have to be determined in the calibration together with the parameters of exterior and interior orientation of the cameras. Lens distortion is compensated by a set of 5 additional parameters modelling radial and tangential distortion (Brown, 1971):

$$\begin{aligned} \bar{x}'_i &= x'_i + dx_i & \bar{y}'_i &= y'_i + dy_i \\ \text{with } dx_i &= x'_i \cdot \left(k_1 r_i'^2 + k_2 r_i'^4 + k_3 r_i'^6 \right) + p_1 \cdot \left(r_i'^2 + 2x_i'^2 \right) + 2p_2 x_i' y_i' & & \quad (3) \\ dy_i &= y'_i \cdot \left(k_1 r_i'^2 + k_2 r_i'^4 + k_3 r_i'^6 \right) + 2p_1 x_i' y_i' + p_2 \cdot \left(r_i'^2 + 2y_i'^2 \right), \\ \text{and } r_i'^2 &= x_i'^2 + y_i'^2 & k_1, k_2, k_3 &: \text{radial distortion} \\ & & p_1, p_2 &: \text{tangential distortion} \end{aligned}$$

For compensation of effects of image digitization and storage, especially of the often a priori unknown difference between the pixel rate of the CCD cameras and the clock rate of the framegrabber and the global effect of linejitter, an additional affine transformation is performed (El-Hakim, 1986):

$$\tilde{x}'_i = a_0 + a_1 \bar{x}'_i + a_2 \bar{y}'_i \quad \tilde{y}'_i = b_0 + b_1 \bar{x}'_i + b_2 \bar{y}'_i \quad (4)$$

or - more transparent, but non-linear - following Albertz and Kreiling (1989):

$$\tilde{x}'_i = x_0 + s_x \bar{x}'_i (\cos \alpha) - s_y \bar{y}'_i (\sin (\alpha + \delta)) \quad (5)$$

$$\tilde{y}'_i = y_0 + s_x \bar{x}'_i (\sin \alpha) + s_y \bar{y}'_i (\cos (\alpha + \delta))$$

$$\begin{aligned} a_0, a_1, a_2, b_0, b_1, b_2 &: \text{parameters of affine transformation.} \\ \text{or } x_0, y_0, s_x, s_y, \alpha, \delta & \end{aligned}$$

Due to linear dependencies on the parameters of the collinearity condition only two of the six parameters of the affine transformation can be introduced as unknowns: for instance scale in x'-image coordinate direction and a shear (s_x and δ resp. a_1 and b_2).

All together one receives 16 parameters modelling the geometry of each camera: 6 for exterior

orientation, 3 for interior orientation, 5 for lens distortion, 2 for electronic influences. These parameters have to be determined in a system calibration before an experiment is performed.

4.2 Multimedia geometry

The effect of a ray being twice broken due to different refractive indices on the optical path through water, glass and air leads to a multimedia geometry model. Knowing the camera calibration data, the refractive indices and the interfaces between the different optical media, this effect can be modelled strictly.

4.2.1 Development of a multimedia module

If the glass wall separating water and air can be considered a plane parallel plate, a simple module based on Snell's Law can be developed, which can be implemented into the collinearity condition equation (2). This module computes a radial shift of each object point relative to the nadir point of the respective camera (Figure 4), which can be used as a correction term in (2). If the X-Y plane of the coordinate system is chosen parallel with the plane interface glass/water (resp. air/glass), some simplifications are possible. The procedure is shown in Figure 4: If the point $P(X, Y, Z)$ in object space is shifted to $\bar{P}(X, Y, Z)$, the collinearity condition can be applied for P using the object coordinates of the shifted point \bar{P} . Only a radial shift by ΔR ($\Delta R > 0$ if $n_2 > n_1$ and $n_3 > n_1$) parallel to the X-Y plane has to be computed for each point relative to the nadir point of each camera. Thus, rays from different cameras C_j to an object point P are calculated with different points \bar{P}_j with the broken beams still intersecting in P .

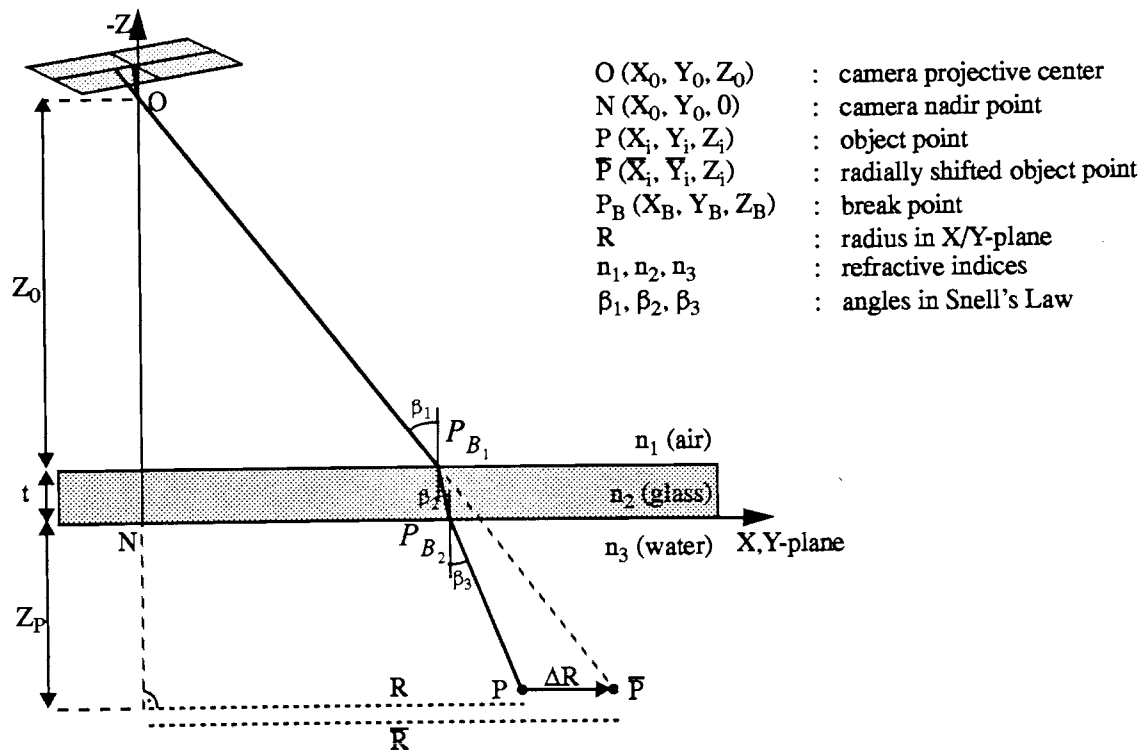


Figure 4: Radial shift for compensation of multimedia geometry

From Figure 4 can be derived:

$$Z_0 \cdot \tan\beta_1 + t \cdot \tan\beta_2 + Z_p \cdot \tan\beta_3 = R \quad R = (Z_0 + t + Z_p) \cdot \tan\beta_1 \quad (6)$$

With Snell's Law

$$n_1 \cdot \sin\beta_1 = n_2 \cdot \sin\beta_2 = n_3 \cdot \sin\beta_3 \quad (7)$$

the system describing the multimedia geometry is complete. Equations (6), (7) can only be solved iteratively due to the trigonometric functions. If P is chosen as a first approximation for \bar{P} and

$$R_{(0)} = \sqrt{(X_P - X_0)^2 + (Y_P - Y_0)^2}, \quad (8)$$

the angle of incidence in the medium n_1 in the first iteration becomes

$$\beta_1 = \arctan\left(\frac{R_{(0)}}{Z_0 + t + Z_p}\right). \quad (9)$$

From Snell's Law one gets the angles of incidence and refraction in the other two media:

$$\beta_2 = \arcsin\left(\frac{n_1}{n_2} \cdot \sin\beta_1\right), \quad \beta_3 = \arcsin\left(\frac{n_1}{n_3} \cdot \sin\beta_1\right) \quad (10)$$

and the correction for $R_{(0)}$:

$$dR = R - (Z_0 \cdot \tan\beta_1 + t \cdot \tan\beta_2 + Z_p \cdot \tan\beta_3). \quad (11)$$

The equations (8) - (11) are used iteratively

$$R_{(1)} = R_{(0)} + dR \quad \Rightarrow \beta_1, \beta_2, \beta_3 \quad \Rightarrow dR \quad \text{etc.}$$

until $dR < \epsilon$ (e.g. with $\epsilon = 0.001$ mm).

Transforming back from polar coordinates to the cartesian system one obtains the coordinates of the radially shifted point P

$$X_P = X_0 + (X_P - X_0) \cdot \frac{R}{R} \quad , \quad Y_P = Y_0 + (Y_P - Y_0) \cdot \frac{R}{R} \quad , \quad Z_P = Z_P \quad (12)$$

The nadir point N is defined herein as the orthogonal projection of the camera projective centre O onto the X-Y plane of the chosen local coordinate system. The collinearity condition can then be used with the radially shifted point \bar{P} (\bar{X} , \bar{Y} , Z) instead of P (X, Y, Z).

The convergence of the iterative scheme equations (8) - (11) can be accelerated considerably by introducing an overcompensation-factor ($ocf \approx 1.1 \dots 1.8$) for the calculation of ΔR . The choice of ocf however depends on the refractive indices, the ratio of the light pathlengths in water and air and the incidence angle itself, so that a constant ocf can only represent an average state. A consequent extension of this idea is the implementation of the radial shift into a lookup-table (input: Depth in water Z_i and radial distance R from nadir point, output: Radial displacement factor \bar{R}/R). The computational effort needed for the initialization of these lookup-tables (one for each camera) will be compensated by the reduced processing time for the particle image sequences, even if they are short.

A more general treatment of the multimedia problem has been published by Kotowski (1988). Kotowski allows for an arbitrary number of optical media with different refractive indices separated by plane interfaces, which do not have to be parallel.

4.2.2 Direct solution for the spatial intersection

If short computation times are required and the least squares adjustment consumes too much computation time, a direct ray tracing and intersection solution can be developed for the spatial intersection following Okamoto and Hoehle (1972) under the premises of plane parallel interfaces as made before. This solution however can only be implemented as a spatial intersection and does not represent a functional model suited for a least squares adjustment.

From the image coordinates x' , y' of a point corrected for the influence of lens distortion and digitization, equations (3), (4), one can calculate the direction cosine in air

$$\begin{bmatrix} a_1 \\ b_1 \\ c_1 \end{bmatrix} = A \cdot \begin{bmatrix} x'/s' \\ y'/s' \\ -c/s' \end{bmatrix} \quad \text{with} \quad s' = \sqrt{x'^2 + y'^2 + c^2} \quad (13)$$

and determine the intersection of the ray with the air/glass interface (Figure 4)

$$\begin{bmatrix} X_{B_1} \\ Y_{B_1} \\ Z_{B_1} \end{bmatrix} = \frac{Z_0 - t}{c_1} \cdot \begin{bmatrix} a_1 \\ b_1 \\ c_1 \end{bmatrix} + \begin{bmatrix} X_0 \\ Y_0 \\ Z_0 \end{bmatrix}, \quad (14)$$

where the beam is broken.

The new direction cosine in glass becomes

$$\begin{bmatrix} a_2 \\ b_2 \\ c_2 \end{bmatrix} = \frac{n_1}{n_2} \cdot \begin{bmatrix} a_1 \\ b_1 \\ c_1 \end{bmatrix} - \left(\frac{n_1}{n_2} \cos i_1 - \sqrt{1 - \left(\frac{n_1}{n_2} \right)^2 + \left(\frac{n_1}{n_2} \cos i_1 \right)^2} \right) \cdot \begin{bmatrix} \lambda_1 \\ \mu_1 \\ v_1 \end{bmatrix} \quad (15)$$

with $(\lambda_1, \mu_1, v_1) = (0, 0, 1)$ in the chosen local coordinate system (plane normal on interface), so that the cosine of the incidence angle i_1 becomes $\cos i_1 = a_1 \lambda_1 + b_1 \mu_1 + c_1 v_1 = c_1$.

The intersection of the ray with the glass/water interface is

$$\begin{bmatrix} X_{B_2} \\ Y_{B_2} \\ Z_{B_2} \end{bmatrix} = \frac{d}{c_2} \cdot \begin{bmatrix} a_2 \\ b_2 \\ c_2 \end{bmatrix} + \begin{bmatrix} X_{B_1} \\ Y_{B_1} \\ Z_{B_1} \end{bmatrix}, \quad (16)$$

and the direction cosine in water becomes

$$\begin{bmatrix} a_3 \\ b_3 \\ c_3 \end{bmatrix} = \frac{n_1}{n_2} \cdot \begin{bmatrix} a_2 \\ b_2 \\ c_2 \end{bmatrix} - \left(\frac{n_2}{n_3} \cos i_2 - \sqrt{1 - \left(\frac{n_2}{n_3} \right)^2 + \left(\frac{n_2}{n_3} \cos i_2 \right)^2} \right) \cdot \begin{bmatrix} \lambda_2 \\ \mu_2 \\ \nu_2 \end{bmatrix}. \quad (17)$$

again with $(\lambda_2, \mu_2, \nu_2) = (0, 0, 1)$ and $\cos i_2 = a_2 \lambda_2 + b_2 \mu_2 + c_2 \nu_2 = c_2$.

Having performed this ray tracing procedure (13) - (17) for two corresponding points of two images (the indices l, r denote the left and right image), a spatial intersection can be computed:

$$Z_P = \frac{Y_{B_{2(r)}} - Y_{B_{2(l)}}}{\frac{b_{3(l)}}{c_{3(l)}} - \frac{b_{3(r)}}{c_{3(r)}}}, \quad (18)$$

if the larger component of the baseline between the two cameras is in Y-coordinate direction, and

$$Z_P = \frac{X_{B_{2(r)}} - X_{B_{2(l)}}}{\frac{a_{3(l)}}{c_{3(l)}} - \frac{a_{3(r)}}{c_{3(r)}}}, \quad (19)$$

if the larger component is in X-coordinate direction. With the appropriate Z_P , we obtain

$$X_P = \frac{1}{2} \left(X_{B_{2(r)}} + X_{B_{2(l)}} + Z_P \cdot \left(\frac{a_{3(l)}}{c_{3(l)}} + \frac{a_{3(r)}}{c_{3(r)}} \right) \right) \quad (20)$$

$$Y_P = \frac{1}{2} \left(Y_{B_{2(r)}} + Y_{B_{2(l)}} + Z_P \cdot \left(\frac{b_{3(l)}}{c_{3(l)}} + \frac{b_{3(r)}}{c_{3(r)}} \right) \right).$$

This direct solution is considerably faster than the least squares adjustment with the collinearity condition, but it is not a strict solution due to the neglection of the redundant information, and it can only be used (optionally) for the spatial intersection in the particle positioning procedure, but not for the spatial resection in the calibration.

4.2.3 Further influences of the multimedia environment

Besides these exactly modelled effects the multimedia environment causes some problems which are not contained in the mathematical model but do have a non-negligible influence on the accuracy of results:

- Aberrations: The optical system (water - glass - air - camera lens) passed by each ray is not corrected for aberrations if lenses are corrected for the use in air. This leads to a degradation of image quality, especially as the cameras are arranged convergently.
- The dispersion in water is much larger than in air. The variance of the refractive index in water over the visible spectrum of light is 1.4% in contrast to 0.008% in air (Hoehle, 1971). This leads to colour seams at the edges of imaged objects which will appear as blur in black-and-white images.
- Inhomogenities of the refractive index (due to local pressure and temperature differences)

cause deviations from the strict mathematical model, which cannot be modelled.

- Deviations from the planeness of the glass walls falsify the incidence angles.
- The network geometry is deteriorated by the smaller intersection angle of rays due to the fact that rays are broken towards the optically denser medium. This causes larger errors in the Z-coordinates.
- Diffusion and absorption in water cause an extinction of light and reduce the image contrast.
- The diffraction is not rotationally symmetric with convergent camera arrangement (Meid, 1991).

All these effects cause a degradation of image quality of multimedia images and systematic errors, which necessarily leads to larger errors in the particle coordinate determination compared with applications in air.

4.3 Handling of the mathematical model

The collinearity condition equation (2) in combination with the additional parameters equations (3), (4) and the multimedia module equations (6) - (12) represents a functional model, which is suited to be linearized as observation equations in a least squares adjustment.

$$(x'_i, y'_i) = f(X_0, Y_0, Z_0, \omega, \varphi, \kappa, c, x_h, y_h, k_1, k_2, k_3, p_1, p_2, s_x, \delta, X_i, Y_i, Z_i). \quad (21)$$

In the calibration procedure this model is being applied for a spatial resection using control points on a calibration frame with known coordinates (X_i, Y_i, Z_i) and introducing the 16 parameters of exterior and interior orientation, lens distortion and affine transformation as unknowns. After the calibration the same model can be used for a spatial intersection introducing the coordinates of a particle as unknowns. In a photogrammetric bundle solution (e.g. Gruen, 1978) resection and intersection for an arbitrary number of cameras and object points can be solved in one system making the solution more accurate and stable.

The stochastic model for the least squares adjustment of the redundant information contained both in the spatial intersection and the resection is the Gauss-Markov model (e.g. Koch, 1980; Slama, 1980, pp. 77 ff):

$$-e = Ax - l \quad (22)$$

with e: true error
 A: design matrix
 x: unknown parameters
 l: observation vector

which leads to the least squares estimation of the unknown parameters

$$\hat{x} = (A^T P A)^{-1} A^T P l = Q_{xx} A^T P l. \quad (23)$$

Besides the estimations of the unknown parameters the Gauss-Markov model gives estimations for the accuracy and reliability of the determined parameters and allows for the detection of gross errors in the observations.

For the procedure of linearization of the observation equations, inversion of the normal equation system, parameter estimation etc. see (Koch, 1980) or (Slama, 1980, pp. 88 ff).

5. System Calibration

To fully exploit the accuracy potential of the method and to get an estimation of the achievable accuracy the imaging system has to be thoroughly calibrated. For this purpose a calibration frame (Figure 5) spanning the entire observation volume is being placed into the object space and imaged by all cameras.

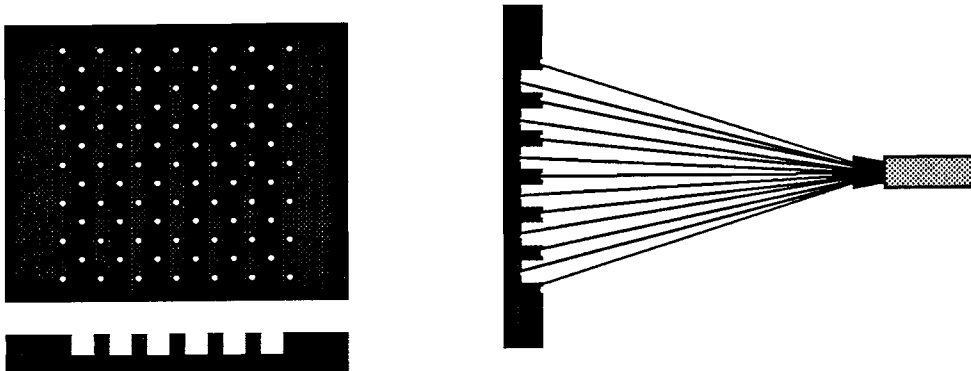


Figure 5: Calibration frame with 85 known control points separated in two planes

The processing of the calibration images is performed automatically after a user supported pre-orientation of the cameras. After the calibration, the 16 parameters describing exterior and interior orientation, lens distortion and affine transformation for each camera are known and can be used for the spatial intersections in the particle positioning. The large number of targets on the calibration frame allows half of the points to be used as control points and the rest as check points. If these check points are treated like unknown points (i.e. their coordinates are determined by spatial intersection using the calibration parameters determined from the resection with the other points) the rms deviations between determined coordinates and the given point coordinates are a good estimate for the accuracy potential of the method.

To test the accuracy potential of the method under ideal conditions a calibration was performed with the calibration frame in air avoiding the problems of the multimedia environment mentioned in 4.2.3. This experiment yielded the following results:

- The estimated standard deviation of measured image coordinates was $\hat{\sigma}_0 = 0.49 \mu\text{m}$, i.e. about 1/25 of a sensor pixel.
- The RMSE at the introduced check points was 0.013 mm in X, 0.011 mm in Y and 0.024 mm in Z. Divided by a the sidelength of the field of view of about 200 mm this corresponds to a relative lateral accuracy of about 1 : 15,000 - 1 : 20,000.

A calibration in water with identical equipment and the same field of view yielded significantly less accurate results:

- The standard deviation of measured image coordinates was $\hat{\sigma}_0 = 1.10 \mu\text{m}$.
- The RMSE at the check points was 0.021 mm (X), 0.034 mm (Y), 0.044 mm (Z).

This shows that the accuracy potential of the hardware system is degraded by about a factor of two by the influences of the multimedia environment. In addition, the additional parameters for lens distortion and affine transformation of the calibration in water were significantly different

from those determined in air, although the lenses had remained untouched. Moreover, if the exterior orientation of the calibration in water was combined with the interior orientation and the additional parameters determined in air, the check point differences were increased considerably and showed a strongly systematic pattern. This proves that the influence of aberration etc. (see 4.2.3) is partly compensated by the set of additional parameters. Therefore it is crucial that the calibration of the system is performed *in situ* under the optical conditions of the experiment.

The mathematical model also allows the refractive index of water to be introduced as an unknown to be determined together with the other calibration parameters. However tests (Maas, 1992a) proved that the correlations between the refractive index and other parameters are too high, so that a reliable determination of the refractive index was not possible.

Another problem is the intermediate storage of the image data on analogue video-tapes. Some tests to quantify the degradation of the image quality due to the analogue storage showed the following results:

- The noise in the greyvalues was increased by 50% (from 0.4 to 0.6 greyvalues).
- Linejitter (Beyer, 1987) was increased by 200% (from 0.04 to 0.12 pixel) due to the smear in the h-sync of the videosignal.
- The RMS of image coordinates of a group of targets measured in each of a sequence of 16 images (i.e. the repeatability of image coordinate measurement in an image sequence) was 0.021/0.010 pixel in the horizontal/vertical image coordinate direction when the image was digitized directly from the camera, and 0.050/0.016 pixel when digitized after intermediate storage on video.
- $\hat{\sigma}_0$ and the rms of the check point differences was increased by about 30%.

This shows clearly that the image quality is significantly degraded by the intermediate analogue storage. However, for many users digital storage facilities are still too expensive to make it a viable alternative.

6. Algorithmic Aspects

The chain of automatic data processing from the digitized images to the 3-D particle trajectories can be subdivided into the following steps:

- Image preprocessing
- Particle detection, determination of particle image coordinates
- Establishment of stereoscopic correspondences
- 3-D coordinate determination
- Tracking in object space

6.1 Image preprocessing

Figure 6 shows an example of a digitized image. Essentially the task of automatic particle identification and particle image coordinate determination in the digital images is trivial, as the particles appear as bright stains on dark background. After highpass-filtering of the images to remove non-uniformities of the background intensity level due to reflections and the non-uniform intensity

profile of the light sheet, particle images can be segmented by a simple thresholding algorithm, and image coordinates can be determined with subpixel accuracy by using the greyvalue-weighted centre of gravity of the segmented blobs.

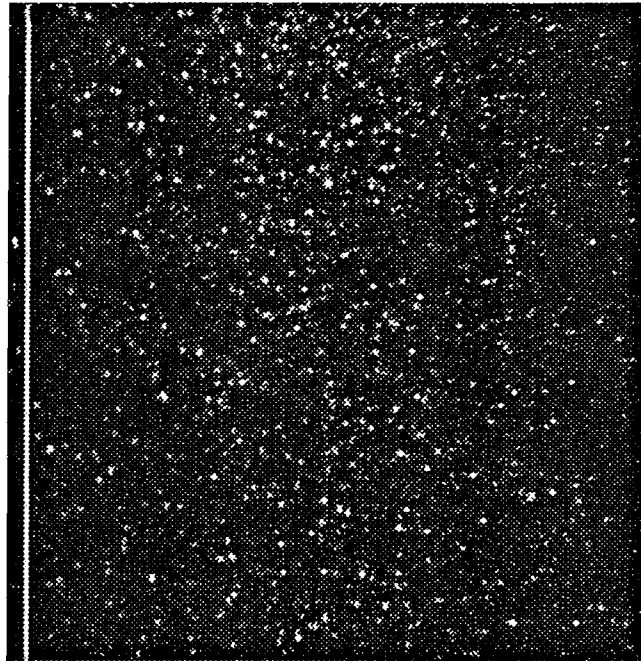


Figure 6: Digitized image (512 x 512 pixel)

With the large number of particles employed here (typically more than 1000 particles in the illuminated section), however, a problem of particles optically blocking or overlapping each other in one or more views occurs (Figure 7).



Figure 7: Examples of overlapping particle images

The problem of overlapping particles has rarely been treated in the PTV literature dealing with automatic systems. However it can be shown (Maas, 1992b), that in a 512 x 512 pixel image with 2000 particles each covering 10 pixel on average, almost 300 cases of overlapping particles can be expected. The number grows linearly with particle image size and with the square of the number of particles per image. This shows clearly that the problem has to be accounted for if the spatial resolution of the system is to be optimized without loss of reliability. Several methods of digital image analysis have been tested to detect and split overlapping images of two or more particles.

- Filtering the images with differential operators proved to be inadequate as they do well in detecting particle image borders but may fail at pixels where particles touch each other, if the contrast is low.
- Template matching (Gruen and Baltsavias, 1988), morphological operators (Ogniewicz and

Kübler, 1989) and Hough transform (Hough, 1962) failed due to the small target size of only 3 x 3 pixels on average.

- Fourier analysis of the particle image border line (Kuhl and Giardina, 1982) worked well with sharp particle images but failed with slightly defocussed images of overlapping particles where the characteristic waist in the border line is blurred.
- Invariant greyvalue moments (Teh and Chin, 1988) do not show this sensitivity to defocusing, but higher order moments are rather noise sensitive. For the recognition of overlaps second order moments proved to be sufficient if only two particles were overlapping, but failed if more than two particles formed a blob.

These problems lead to the development of a modified anisotropic thresholding operator, which searches for discontinuities in the greyvalues inside segmented blobs and splits blobs if a discontinuity exceeding a certain empirically determined limit is detected. The operator can be characterized by some rules describing a particle image:

- all pixels of a particle image have a greyvalue which is larger than a preset threshold
- a particle image shows exactly one local maximum
- greyvalues drop continuously inside a particle image
- a pixel representing a local greyvalue minimum belongs to the particle containing its neighbour pixel with the largest greyvalue

This operator can be implemented very efficiently and performed satisfactorily. From comparisons with a human supervisor it can be said that in all cases where the human could make a clear decision the operator made the same decision. Most importantly, unlike some of the other methods mentioned above, it does not only indicate cases of overlapping particle images but splits them correctly at local greyvalue minima.

6.2 Establishment of stereoscopic correspondences

To compute 3-D particle coordinates a spatial intersection has to be performed with corresponding image coordinates of a stereopair. The establishment of those stereoscopic correspondences however poses some problems. The particle images do not show any characteristic features (like colour, size, shape, etc.), which could allow for a reliable distinction of particles. The only criterion which can be applied is the geometric constraint of the epipolar line. Knowing the orientation parameters of the cameras from the calibration procedure, proceeding from a point P' in one image an epipolar line in an other image can be calculated, on which the corresponding point has to be found. In the strict mathematical formulation this line is a straight line, in the more general case with convergent camera-axes, non-negligible lens distortion and multimedia geometry, the epipolar line will be a slightly bent line (Figure 8), which can be approximated by a polygon. Its length l can be restricted if approximate knowledge about the depth range in object space coordinates is available, which is determined from the knowledge of the illuminated test section (Figure 9). Adding a certain tolerance width ϵ to this epipolar line segment (due to data quality) the search area for the corresponding particle image becomes a narrow two-dimensional bandshaped window in image space.

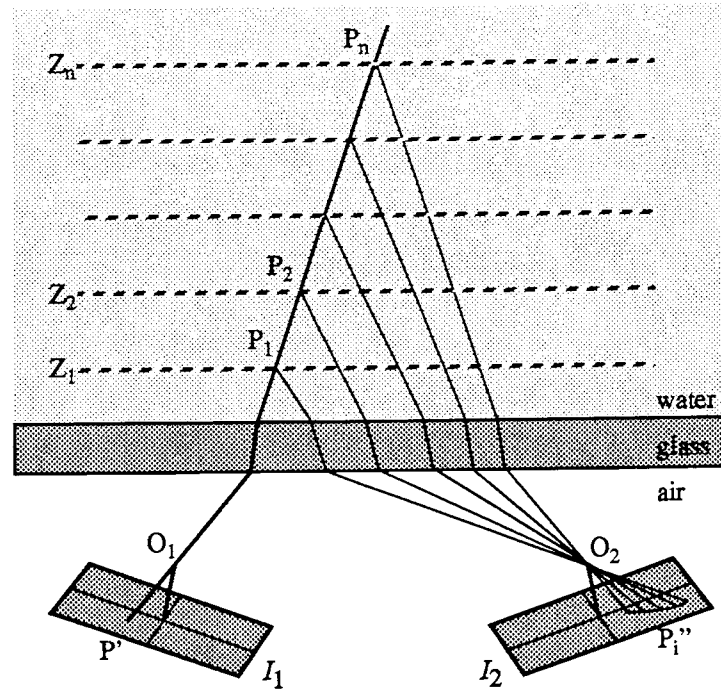


Figure 8: Derivation of epipolar lines in multimedia geometry

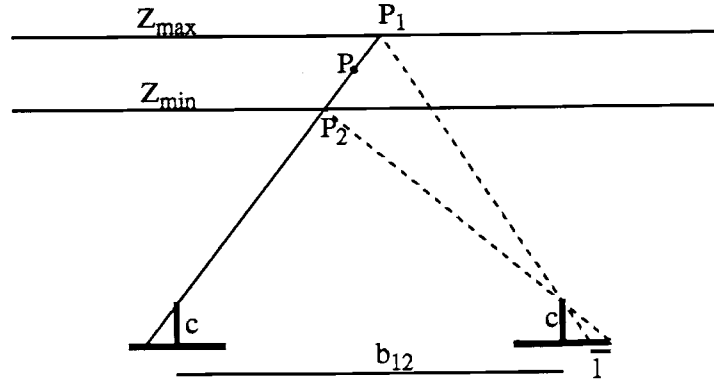


Figure 9: Length of epipolar search window

Due to the large number of imaged particles a second problem of ambiguity occurs, as often two or more particle images will be found in the search area. The number of ambiguities grows (Maas, 1992b)

- approximately with the square of the number of particles
- linearly with the length of the epipolar line segment
- linearly with the width of the epipolar search window.

If the particle features do not allow a reliable distinction of particles, these ambiguities cannot be resolved by a system based on two cameras only. With realistic estimates for the number of particles per image and the dimensions of the epipolar search window in a reasonable camera setup the expected number of ambiguities becomes too large for a two-camera-system to yield a robust solution of the correspondence problem (see Table 2).

A consequent solution of the ambiguity problem is the use of a third camera in a setup as shown in

Figure 2 with the camera projective centres forming a triangle (in the ideal case an equilateral triangle) and the camera axes approximately forming a tetrahedron (Figure 10).

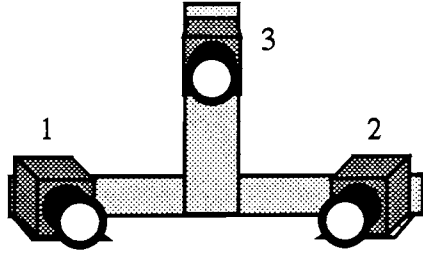


Figure 10: Arrangement of three CCD cameras for the method of intersection of epipolar lines

This setup allows the calculation of epipolar line segments intersecting in the image, which can be exploited as shown in the example in Figure 11:

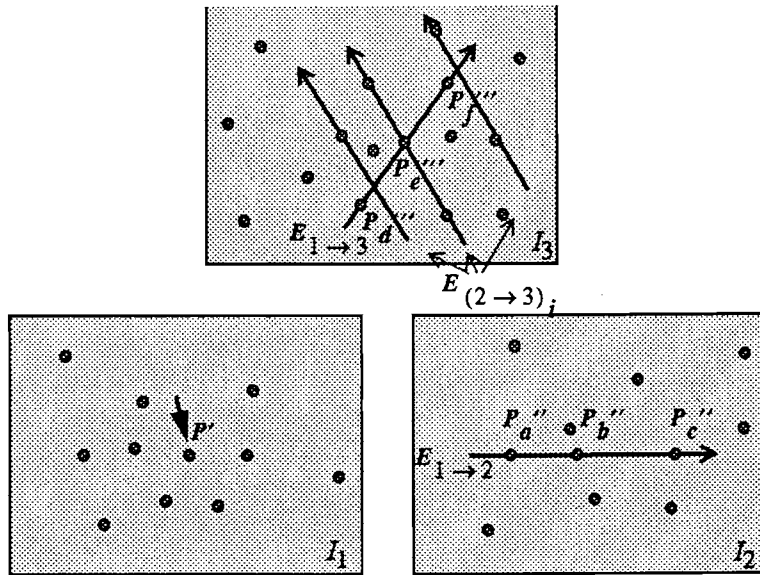


Figure 11: Principle of intersection of epipolar lines

Proceeding from a point P' in the image I_1 all epipolar lines $E_{1 \rightarrow 2}$ in I_2 and $E_{1 \rightarrow 3}$ in I_3 are derived, on which respectively candidates P_a'' , P_b'' , P_c'' , and P_d'''' , P_e'''' , P_f'''' will be found in Figure 11. An unambiguous determination of the particle image corresponding to P' can neither be found in I_2 nor in I_3 . However if all epipolar lines $E_{(2 \rightarrow 3)_i}$ of all candidates P_i in I_2 are being intersected with the epipolar line $E_{1 \rightarrow 3}$, there will be a large probability that only one of the intersection points will be close to one of the candidates in I_3 (in Figure 11: P_e''''). This consideration has been implemented via a combinatorics algorithm which tries to find such consistent triplets in the three particle image coordinate datasets and rejects points which are members of more than one consistent triplet. Such an unambiguous consistent triplet is a necessary and sufficient condition for the establishment of correct correspondence. A similar, but iterative approach can be found in (Kearney, 1991). It can be shown, that the method of intersection of epipolar lines can reduce the number of remaining ambiguities by at least one order of magnitude (Maas, 1992b); these remaining ambiguities cause inconsistent triplets and can thus be rejected.

The method described above is the most evident, but not the only way of exploiting a third

camera. Employing a different algorithm one can also work with three cameras which are arranged such that their projective centres are lying on a straight line (Maas, 1992b). The expectable numbers of remaining ambiguities for the methods discussed above are compiled in Table 2 for realistic assumptions for the number of particles (n), the depth range in object space (ΔZ) and the width of the epipolar search area (ε) for a base $b_{13} = 200$ mm and a camera constant $c = 9$ mm:

Table 2: Remaining numbers of ambiguities in the establishment of correspondences

	2 cameras	3 cameras collinearly	3 cameras in equilateral triangle
$n = 1000, \varepsilon = 10 \mu\text{m}, \Delta Z = 40 \text{ mm}$	401	40	35
$n = 2000, \varepsilon = 10 \mu\text{m}, \Delta Z = 40 \text{ mm}$	1605	160	140
$n = 1000, \varepsilon = 5 \mu\text{m}, \Delta Z = 40 \text{ mm}$	201	10	9
$n = 1000, \varepsilon = 10 \mu\text{m}, \Delta Z = 80 \text{ mm}$	802	40	35

The number of remaining ambiguities is reduced by at least one order of magnitude for both of the three-camera arrangements compared with a two-camera arrangement. If the number is still considered too large it can be reduced straightforwardly by the use of a fourth camera with the aim of establishing consistent quadruplets in the four sets of particle image coordinates. The projective centres of a four-camera system can be arranged in a square (Figure 12), collinearly or in a combination of both.

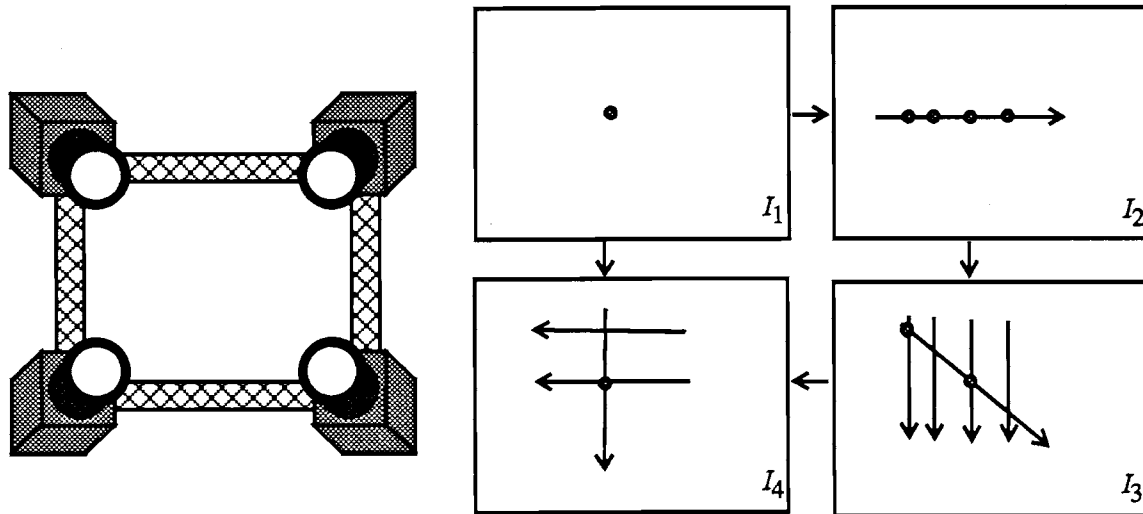


Figure 12: Example of a four camera arrangement

The principle allows to use an arbitrary number of cameras, but more than four will rarely be necessary. A four-camera arrangement can be considered ideal: it reduces the number of remaining ambiguities to almost zero, and it even allows a reliable determination of most of those particles which are completely hidden in one of the four images.

6.3 3-D coordinate computation

After the establishment of correspondences the 3-D coordinates for the non-ambiguous quadru-

plets (triplets, pairs) can be determined by spatial intersection using either the strict solution via least squares adjustment or bundle solution using equations (1) - (12) or the faster, but less accurate solution equations (13) - (20). Another benefit of the three- and four-camera systems as compared with a two-camera-system is improvement of the accuracy of the coordinates of a point by a factor of approximately 1.3 or 1.7, respectively.

The results are datasets with 3-D particle coordinates, which are passed to the tracking module to establish correspondences in time (see Malik et al., 1993, part II of this publication).

7. Results

With our PTV-method 3-D coordinates of up to 1300 particles could be determined with a three-camera arrangement. The main limitations were the sensor size, the number of overlapping particles and the image quality, which was usually degraded by the fact that none of the light sources mentioned in (3.2) yielded an ideal illumination. The standard deviations of the particle coordinates determined from the least squares adjustment were typically 0.06 mm for the X and Y coordinates and 0.18 mm for the Z coordinate (depth direction perpendicular to camera base) in an observation volume of $200 \times 160 \times 50 \text{ mm}^3$. This is worse than the values for check points on the calibration frame, but one has to consider that a moving particle is a much worse target than a well-defined static point. The standard deviations of the particles are for example influenced by the not perfectly spherical shape of particles, but one can expect that these effects are highly correlated in consecutive datasets. To prove the existence of this correlation a test was performed by recording stationary targets with a similar image quality like particles from a moving carriage under illumination conditions of the real experiment (Papantoniou and Maas, 1990). The RMS variation of 458 determined velocity vectors were 0.028, 0.055, 0.042 mm for the X,Y,Z vector components in a volume of $140 \times 120 \times 10 \text{ mm}^3$. This suggests, that the correlation between consecutive time steps is relatively high and that the accuracy of the determined velocity vectors is significantly better than the coordinates of a single determined particle. The largest RMS error occurs in the moving direction of the carriage, which can be explained by unsteadiness of the carriage velocity due to the stepper motor drive. More importantly, errors in velocity vectors due to coordinate determination do not propagate along trajectories.

The computation times for the 3-D coordinate determination on a SUN 4/490 are:

• Highpassfiltering	2.0 sec/img
• Image segmentation	2.2 sec/img
• Establishment of correspondences	5.3 sec
• Spatial intersection (see 3.2.2)	1.8 sec
• Total	20 sec

The initialization of the multimedia lookup-table (4.2.1) takes 8.3 seconds, but it has to be performed only once in combination with the calibration.

8. Conclusion

A digital photogrammetric three-dimensional particle tracking velocimetry system is a powerful

and versatile flow measurement instrument. To fully exploit the potential of the technique an installation should be based on three or four CCD-cameras. An exact mathematical modelling of the multimedia environment and a thorough calibration of the system was found to be crucial for the success of the method. A key point is the careful handling of ambiguities occurring both in the identification of particles and in the establishment of stereoscopic correspondences. With standard CCD-cameras up to 1000 simultaneous particles could be tracked with a temporal resolution of 25 velocity fields per second; the lateral accuracy of the determined velocity vectors was about 1:4000 of the camera's field of view, while the depth accuracy was about a factor of 2 worse than the lateral accuracy. High resolution CCDs with up to 4096 x 4096 pixels or high speed CCDs with up to 1000 images per second (Maas, 1992c) allow variations of the resolution towards higher spatial resolution on cost of temporal resolution or vice versa. Recent developments in hardware will considerably influence the design of PTV-systems and improve their performance: HDTV (high definition television) will soon make cameras available with sensors of more than one megapixel at temporal resolutions of nowadays standard cameras. Digital storage facilities will become viable as well if their costs drop further, and progress in computer workstation performance will make data processing much faster.

Acknowledgement: This work has been supported by the Swiss National Foundation for Scientific Research.

References:

1. Adamczyk, A., Rimai, L., 1988: Reconstruction of a 3-Dimensional Flow Field from Orthogonal Views of Seed Track Video Images. *Experiments in Fluids* 6, pp. 380 - 386.
2. Adrian, R., 1986: Multi-Point Optical Measurements of Simultaneous Vectors in Insteady Flow - a Review. *The International Journal of Heat and Fluid Flow*, Vol. 7, No. 2, S. 127 - 145
3. Albertz, J., Kreiling, W., 1989: Photogrammetrisches Taschenbuch. Wichmann Verlag, Karlsruhe
4. Beyer, H., 1987: Some Aspects on the Geometric Calibration of CCD-Cameras. *Proceedings Intercommission Conference on Fast Processing of Photogrammetric Data*, Interlaken, Schweiz, 2-4 Juni, S. 68 - 81
5. Brown, D., 1971: Close-Range Camera Calibration. *Photogrammetric Engineering*, Vol. 37, No. 8
6. Chang, T., Watson, A., Tatterson, G., 1985a: Image Processing of Particle Motions as Applied to Mixing and Turbulence Flow - 1. *Chemical Engineering Science*, Vol 40, No. 2, pp 269-275
7. Chiu, W., Rib, L., 1956: The Rate of Dissipation of Energy and the Energy Spectrum in a Low Speed Turbulent Jet. *Transactions of the Americal Geophysical Union*, Vol. 37/1

8. El-Hakim, S.F., 1986b: Real-Time Image Metrology with CCD Cameras. Photogrammetric Engineering and Remote Sensing, Vol. 52, No. 11, pp. 1757 - 1766.
9. Gruen, A., 1978: Accuracy, Reliability and Statistics in Close-Range Photogrammetry. International Archives of Photogrammetry, Vol. 22, Part V
10. Gruen, A., Baltsavias, E., 1988: Geometrically Constrained Multiphoto Matching. Photogrammetric Engineering, Vol. 54, No. 5, pp. 633 - 641
11. Hoehle, J., 1971: Zur Theorie und Praxis der Unterwasser-Photogrammetrie. Schriften der DGK, Reihe C, Heft 163.
12. Hough, P., 1962: Method and Means for Recognizing Complex Patterns. U.S. Patent 3069654
13. Jacobi, O., 1980: Photogrammetric Tracking of a Moving Particle in Running Water. International Archives of Photogrammetry, Vol. XXIII, pp. 369-374
14. Kasagi, N., Nishino, K., 1990: Probing Turbulence with Three-Dimensional Particle Tracking Velocimetry. Proceedings International Symposium on Engineering Turbulence - Methods and Measurements, Dubrovnik, September 24-28
15. Kearney, J.K., 1991: Trinocular Correspondence for Particles and Streaks. Dept. of Computer Science, The University of Iowa, Technical Report 91-01
16. Koch, K.R., 1980: Parameterschätzung und Hypothesentests in linearen Modellen. Dümmler Verlag, Bonn.
17. Kotowski, R., 1988: Phototriangulation in Multi-Media-Photogrammetry. International Archives of Photogrammetry and Remote Sensing, Vol. XXVII
18. Koyabashi, T., Sata, T., Sekimoto, K., 1989: Velocity Measurement of Three-dimensional Flow around Rotating Parallel Disks by Digital Image Processing. Flow Visualization 1989
19. Kuhl, F., Giardina, Ch., 1982: Elliptic Fourier Features of a Closed Contour. Computer Graphics and Image Processing 18, pp. 236 - 258
20. Maas, H.-G., 1990: Digital Photogrammetry for Determination of Tracer Particle Coordinates in Turbulent Flow Research. ISPRS Com. V Symposium Zürich, 3.-7. 9. 1990, published in SPIE Proceedings Series Vol. 1395, Part I
21. Maas, H.-G., 1992a: Digitale Photogrammetrie in der dreidimensionalen Strömungsmesstechnik. Ph.D. Thesis No. 9665, ETH Zurich
22. Maas, H.-G., 1992b: Complexity analysis for the determination of image correspondences in dense spatial target fields. International Archives of Photogrammetry and Remote Sensing, Vol. XXIX
23. Maas, H.-G., 1992c: High-Speed Solid State Camera Systems for Digital Photogrammetry. International Archives of Photogrammetry and Remote Sensing, Vol. XXIX
24. Malik, N., Dracos, T., Papantoniou, D., Maas, H.-G., 1993: Particle Tracking Velocimetry in Three-dimensional Turbulent Flows - Part II: Particle Tracking and Lagrangian Trajectories

25. Meid, A., 1991: Wissensgestützte digitale Bildkoordinatenmessung in aberrationsbehafteten Messbildern. Ph.D. Thesis University of Bonn
26. Nishino, K., Kasagi, N., Hirata, M., 1989: Three-Dimensional Particle Tracking Velocimetry Based on Automated Digital Image Processing. *Journal of Fluid Engineering*, Vol. 111, pp. 384-391.
27. Nishino, K., Kasagi, N., 1989: Turbulence Statistics in a Two-Dimensional Channel Flow Using a Three-Dimensional Particle Tracking Velocimeter. *Proceedings on the Seventh Symposium on Turbulent Shear Flows*, Stanford University, August 21-23
28. Ogniewicz, R., Kübler, O., 1989: Lage- und Skalierungsinvariante Skelette zur Robusten Beschreibung und Erkennung binärer Formen. *Mustererkennung 1989*, Springer Verlag
29. Okamoto, A., Höhle, J., 1972: Allgemeines analytisches Orientierungsverfahren in der Zwei- und Mehrmedien-Photogrammetrie und seine Erprobung. *Bildmessung und Luftbildwesen* 2/1972, 3/1972.
30. Papantoniou, D., Dracos, T., 1990a: Analyzing 3-D Turbulent Motions in Open Channel Flow by Use of Stereoscopy and Particle Tracking. in: *Advances in Turbulence 2*, Editors H.-H. Hernholz, H.E. Fiedler, Springer Verlag, Heidelberg
31. Papantoniou, D., Dracos, T., 1990b: Lagrangian Statistics in Open Channel Flow by 3-D Particle Tracking Velocimetry. in: *Eng. Turb. Model. Expt.* Elsevier
32. Papantoniou, D., Maas, H.-G., 1990: Recent Advances in 3-D Particle Tracking Velocimetry. *Proceedings 5th International Symposium on the Application of Laser Techniques in Fluid Mechanics*, Lisbon, July 9-12
33. Sata, Y., Nishino, K., Kasagi, N., 1989: Whole Field Measurement of Turbulent Flows Using a Three-Dimensional Particle Tracking Velocimeter. *5th International Symposium on Flow Visualization*, Prague, August 21-25
34. Sheu, Y., Chang, T., Tatterson, G., 1982: A Three-Dimensional Measurement Technique for Turbulent Flows. *Chemical Engineering Communications*, Vol. 17, pp. 67-83
35. Slama, C., 1980 (Ed.): *Manual of Photogrammetry*. American Society of Photogrammetry, Falls Church, Virginia
36. Teh, Ch., Chin, R., 1988: On Image Analysis by the Method of Moments. *IEEE PAMI*, Vol. 10, No. 6, pp. 496 - 513

LAGRANGIAN STATISTICS IN OPEN CHANNEL FLOW BY 3-D PARTICLE TRACKING VELOCIMETRY

D. Papantoniou and Th. Dracos

Institute for Hydromechanics and Water Resources Management
ETH Hönggerberg, 8093 Zürich, Switzerland

1 Introduction

The turbulent boundary layer flow has been studied for quite some time both experimentally and numerically. The availability of a numerical turbulent flow data base (e.g., [1]) has fuelled a renewed experimental interest in this flow, especially by use of whole field techniques. Numerical techniques based on direct solutions to the N-S equations have also been applied to the study of the Lagrangian turbulent statistics via numerically computed particle trajectories in an isotropic turbulent flow [5]. Three component velocity measurements in the b.l. flow have been performed by point-measurement techniques [2,3,4] and recently by the 3-D particle tracking velocimetry (PTV) method [6]. We have developed a 3-D PTV system which is capable of measuring a fine series of instantaneous 3-component velocity distributions over an extended flow volume, with a data density exceeding 10 vectors per cubic cm. It is based on stereoscopic recording and analysis of small neutrally buoyant particle positions and subsequent tracking in the time domain. The method is non-intrusive and has the advantage of being able to follow (track) a spatially dense set of individual particles for a sufficiently long period of time to permit a Lagrangian description of the flow process. We are reporting on the basic features of the system and present results from its application in the fully developed open channel flow.

2 Three-dimensional whole field velocimetry and PTV

Virtually all whole field velocimetry methods rely on the measurement of the displacement field of optical tracers suspended in the flow over a time interval. Since the time interval is usually known with good precision, the overall error depends on the accuracy of determination of the tracer displacements, which is often done manually. Most of the whole field velocimetry methods reported so far are two-component methods. These are primarily applicable to flows which are basically two-dimensional, where information is gathered on a selected flow plane. In some cases the out-of-plane velocity component has been derived from the in-plane components via the application of the continuity equation [7]. In contrast, 3-D methods are gathering information over a flow volume and rely on holography or stereoscopy to determine successive 3-D tracer positions. Results using such a method were published more than 35 years ago [13]. However, it is only recently with the use of digital techniques that the degree of automation and resulting measurement accuracy has advanced to a point that their application is fruitful.

The implementations reported so far, while sharing the basic conceptual steps, have varied considerably in their details; others relied on cameras and film as the recording medium [8,9,10,13], while more recent ones use video cameras and recorders [6,12]. The degree of automation has been increasing; the original method [13] was entirely manual, while the most recent approaches tend towards complete automation. The implementations also vary in the degree of success, as measured by the attained accuracy and the resultant information yield. The last issue has been one of the drawbacks of the technique so far, since the information density which has been reported (in some cases only 10–20, in general less than 150 vectors per instant) is not sufficient to describe the instantaneous features and the evolution of various three-dimensional turbulent flow events.

Stereoscopic methods share the following basic steps:

- a) stereoscopic imaging and recording of a suitably illuminated particle-laden flow
- b) subsequent photogrammetric analysis of the resulting images to derive the instantaneous 3-D particle positions and
- c) tracking of the 3-D coordinate sets in time to derive the tracer trajectories.

Small neutrally buoyant particles are used as optical tracers, which are excellent flow trackers; the resulting displacement field thus matches the instantaneous flow displacement field at the particle positions. An inherent strength of the technique is that in addition to offering instantaneous spatially dense 3-D velocity field information, it is capable of yielding a Lagrangian flow field description in terms of long particle trajectories. In fact, photographic recording of tracks in two orthogonal views has been used to measure Lagrangian correlation coefficients and turbulent dispersion in an open channel flow [14]. Lagrangian statistics may be obtained with a relatively sparse particle distribution. Results based on tracking of a single particle have been reported [18]. On the other hand, the distribution of flow quantities based on velocity derivatives, such as the vorticity, may be estimated with sufficient accuracy only if the velocity field is sampled with adequate density at any instant. This implies that the attainable spatial data density becomes of paramount importance if such quantities are to be estimated for a given flow [15].

The development goals for our own implementation of the 3-D PTV were focused on the obtainable accuracy and ease of use; at the same time a considerable increase over the previously reported information density was sought.

3 Experimental method and conditions

The experimental data were obtained at the 24 m open channel flume of the ETH, (60 cm wide, tilting). A 3 W argon-ion laser beam, with externally triggerable intensity modulation was used to illuminate a $10 \times 10 \times 1.5$ cm flow volume, parallel to the bottom of the channel. Three synchronized video cameras, mounted in a stereoscopic arrangement with their axes intersecting at about 50 degrees, were used to image this flow volume. A carriage system driven by a stepper motor was used to translate both the illumination optics and the 3 cameras on precision rails running along the channel. The translation speed was monitored with very good precision and was about 2.5 cm/sec less than the mean flow speed. A video coding/synchronization circuit uniquely marked each synchronous frame and provided external triggering source to the Bragg cell modulating the laser beam. The three video channels were recorded on U-matic video recorders at 25 frames/sec. Poliolite particles, of nominal size $50 \mu\text{m}$ were used as flow tracers. The streamwise extent of the test section of the channel is 2 m, permitting continuous observation, in the translating volume, during at least 15 seconds. The illuminated volume extended from 5 mm above the channel bed to about 20 mm. The mean flow speed, based on volume rate and cross-sectional area, was 8.3 cm/sec, and the total flow depth was 5.35 cm. The friction velocity u^* was 5.2 mm/sec, and the Reynolds number, Re^* , was 270. The experimental arrangement is shown schematically in Figure 1.

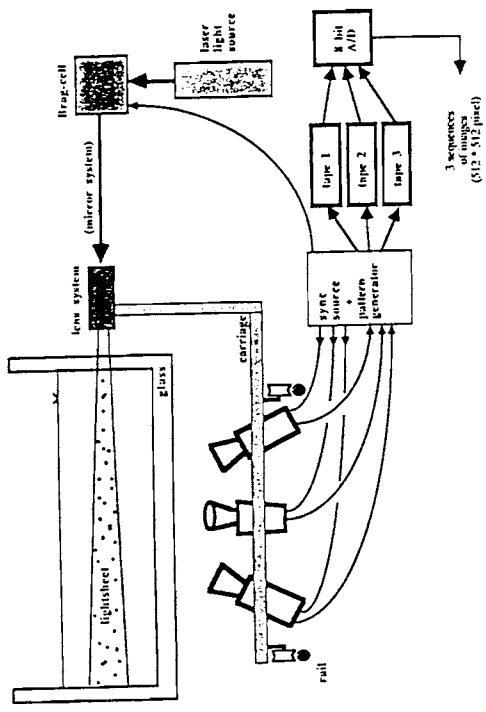


Figure 1. Experimental arrangement.

Major improvements over previously reported implementations, including our own [16], have been the employment of three video cameras in the stereoscopic arrangement and the use of a strobed illumination source. The photogrammetric analysis used to derive the instantaneous 3-D positions can accurately handle three different media (in the present case: water, glass, air) in the light path between the light scattering particles and the video sensor. This makes the method quite versatile, offering an advantage over methods where a single optical medium can only be handled so that the cameras have to be immersed in the liquid medium and necessarily remain at a fixed position [6]. The use of the third camera has proved very valuable in increasing both the positioning accuracy and the velocity vector yield. The yield depends partly on the number of reconstructed 3-D particle coordinates per sample, which is equal to the number of particle images that can be successfully matched between the three stereo views. In a two camera arrangement the search area for a stereo match candidate of a particle image in a frame is along the entire length of the epipolar segment corresponding to the particle image in the other stereo frame. Multiple candidates, the possibility for which is rapidly increasing with increasing particle image density, lead to match ambiguities. In the three camera arrangement, the search area for match candidate in a one of the stereo frames is reduced to a small image area around the intersection of the two epipolar segments corresponding to possible match candidates in the other two stereo frames. This considerably reduces the chance for ambiguities during stereo matching in frames crowded with particle images. The increase of positioning accuracy is due to the increased redundancy, since there are six observations (image coordinates) for the three unknown object coordinates, compared with four observations for the same three unknowns for a two camera system.

Strobing the illumination synchronously to the video framing with the digitally controlled light pulse duration kept under 4 ns, results to sharp particle images for a wide range of particle velocities. The sampling interval is 40 ms as defined by the video frame time. If the illumination is not pulsed and the camera sensors are allowed to integrate for the entire 20 ms of the video field time, streaks may form resulting to particle positioning ambiguity. For large enough particle velocities, the streaks may become disconnected

between the two video fields, dictating treatment of the individual video fields instead of frames. This would result to a severe drop in spatial resolution for a certain class of video sensors.

Digitization of the long video sequences is effected automatically by real time identification of the sequence frame number coded on each frame, and computer control of the video tape recorder functions during playback. The digital image sequences are also processed automatically on a Sun workstation. For each image triplet, image coordinates of the particles are determined by adaptive thresholding and connectivity analysis, used with peak fitting for merged images. Detected images of size less than a preset minimum are discarded. These lists of image coordinates are then stereo-matched using the calibration model and the epipolar geometry. After matching, a least squares adjustment using the six observations for each particle yields the object-space coordinates. The calibration of the three-camera system is affected by imaging, prior to each experiment, a plate with a large number of optical targets placed in the test section. The positions of the targets are known with very high precision, allowing the derivation of an accurate photogrammetric model for the entire optical system which is used for the stereo matching and the least squares adjustment.

The 3-D trajectories are established automatically by a tracking system that uses three successive data sets at a time (Sct_0, Sct_1, Sct_2) to derive the connections between Sct_0 and Sct_1 . Then Sct_1 and Sct_2 replace Sct_0 and Sct_1 , the next set becomes Sct_2 , etc. There is an advantage in tracking 3-D positions over tracking the path projections in image space as has been done in some implementations [9,10,11]. Tracking ambiguities increase in the projected view since tracer positions may appear to coincide or cross; such overlaps are very improbable in space [6,8]. It has been pointed out [16] that a parameter describing tracking difficulty is the ratio of the average distance between particles, D_o , to the average distance, D_t , traveled between frames. For turbulent flow motions tracking clearly becomes impossible if $D_o \ll D_t$. There are also other factors affecting tracking difficulty, most notably the presence of "noise" in the form of coordinates that are not matchable to any coordinate in an adjacent frame. Such cases arise from the use of thresholds during the particle image identification and stereo-matching. For a given image sequence the amount of such noise presented to the tracking code increases with lower values of these thresholds. With a nominal number of 850 coordinates per set, it is estimated that at least 40% of the particle positions presented to the matching code are not matchable, which in fact represents a rather high level of noise. The tracking code is designed to operate in the presence of such noise by utilizing a model of particle motion. It operates quite comfortably with D_o/D_t about 2. Basic elements of this model are that the velocity and acceleration of fluid elements are bounded as well as that spatial velocity differences are bounded. The drawbacks of using a model which employs thresholds on turbulence quantities is that some turbulent motions may be excluded, e.g., motions corresponding to very sudden high accelerations. Thus, the statistical results may become biased towards the more "regular" motions, i.e., motions conforming to the model. The code is "adaptive" in the sense that it derives estimates of local turbulent quantities, such as the local velocity and a measure of the local rms kinetic energy, and uses them during tracking. These local estimates of course vary both in space and time. The entire data reduction system is automated, and can process a sequence of 3x100 frames in about 3 hours. The accuracy of the determined coordinates is 0.08 mm for the x and z coordinates and 0.23 mm for the y coordinate. Since the y coordinate is derived from observations in x and y its accuracy is expected to be less than the accuracy of the planimetry coordinates. The number of erroneous connections in each set is a very small percentage of the total connections in the set (less than 1%). What is more

important, is that errors cannot and do not propagate into erroneous trajectories. But for a single vector connection, especially when it is a new, isolated connection and not a continuation of a trajectory, the possibility for committing a tracking error exists and, with increasing "noise", the percentage of such isolated errors is in fact increasing if the model parameter thresholds are increased. However, if tracking parameters are set rather conservatively, the percentage of erroneous connections is maintained at a very low level. The final operational values of the model parameter settings were determined after careful examination of the actual results obtained when these were varied. A significant criterion that may be used to determine a posteriori the success of tracking is the percentage of vectors which are part of a trajectory. In fact, more than 80% of the tracked vectors belong to trajectories, or portions of a trajectory, composed of at least four vectors.

4 Results and discussion

The results of each experiment forms a database of particle trajectories. Figure 2 shows a

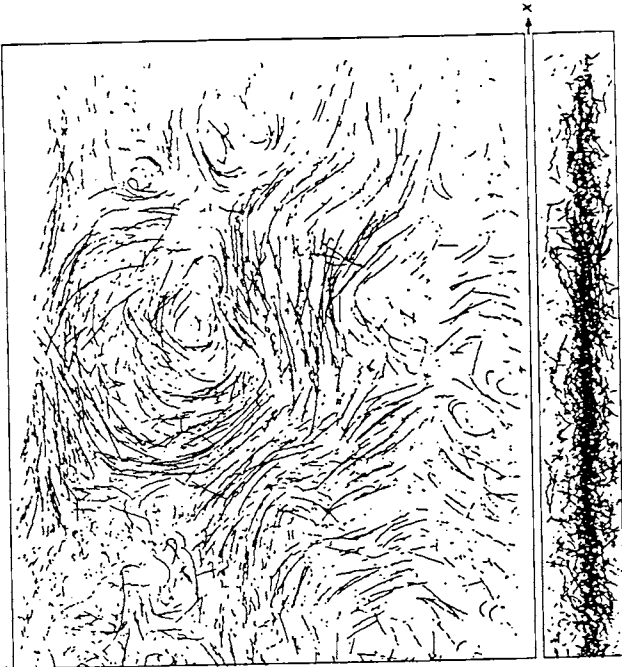


Figure 2. A 1.2 sec portion of the track database.

portion of the database, corresponding to 1.2 s of flow, as seen by a observer convection with the mean flow speed. The observation volume x, y, z dimensions are $120 \times 15 \times 90$ mm. The upper, $z-x$ view is the planimetry view, while the lower $y-z$ view is the side view of the observation volume with the depth coordinate, y , increasing downwards. Edges whose horizontal extent is comparable with the total depth of the flow are obviously present in these data.

The trajectories may be used to compute the conventional turbulence statistics that are usually obtained by an Eulerian measurement approach. Since a single run is limited to about 15 seconds of flow, convergence of the turbulence statistics to the values obtained by fixed probes would be expected if results from at least 10-20 experimental runs were ensemble averaged. In what follows we present statistical results based on conventional

averaging, as a function of distance from the boundary, of trajectories obtained from a single run corresponding to 15 seconds of observation. These are not directly comparable to results obtained by Eulerian averaging over the same time interval since in essence they record the evolution of almost the same eddy distribution during the observation time.

The statistics at a certain y -value were obtained by averaging over the number of vectors whose midpoint was within half a millimeter from y . This distribution almost Gaussian as a function of $(y - y_c)$ where y_c corresponds to 13 mm, due to the Gaussian light intensity profile in the illuminated layer. The number of vectors used for each y -value is presented in Figure 3. The value of the friction velocity u^* was obtained by

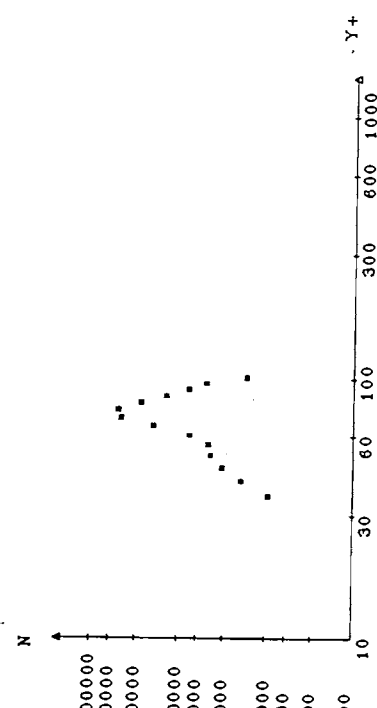


Figure 3. Number of vectors in each subset

two independent methods: (1) using Manning's formula to obtain the shear stress, and (2) fitting the $U'(y)$ data to the logarithmic profile with the constants recommended by Nezu and Rodi [17] obtained under very similar flow conditions. There was satisfactory agreement between the two estimates despite the limitations of the averaging procedure. The profiles of the average velocity components U , V , W are shown in Figure 4, along

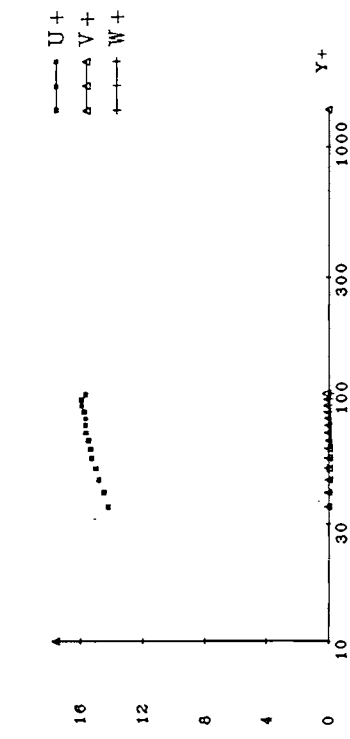


Figure 4. Average velocity profiles.

with the log-law estimate for U . It may be observed that they converge quite well to the conventional long-time Eulerian average values expected in this flow. In Figure 5 profiles

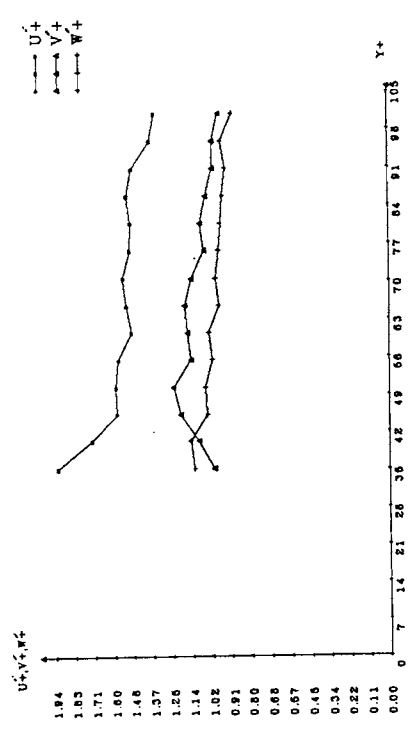


Figure 5. Rms velocity profiles.

for the 2nd order statistics are presented. The value of r may be overestimated due to the decreased positioning accuracy in y . The intensity fluctuation profiles tend to converge to their long-time Eulerian values, albeit not as fast as the 1st order profiles. However, the cross-term 2nd order statistics including the $-uv$ shear stress profile, (Figure 6)

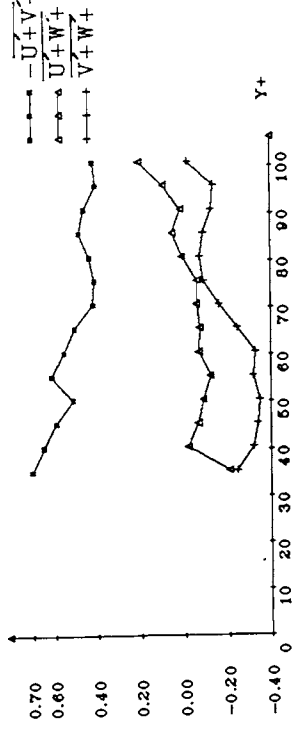


Figure 6. Shear stress profiles.

exhibit the expected non-stationarity. Even stronger non-stationarity is exhibited in the 3rd order turbulence statistics.

The trajectory data base can be used to compute the Lagrangian properties of the fluid element motions, of which the correlation functions and diffusion lengths are of fundamental importance.

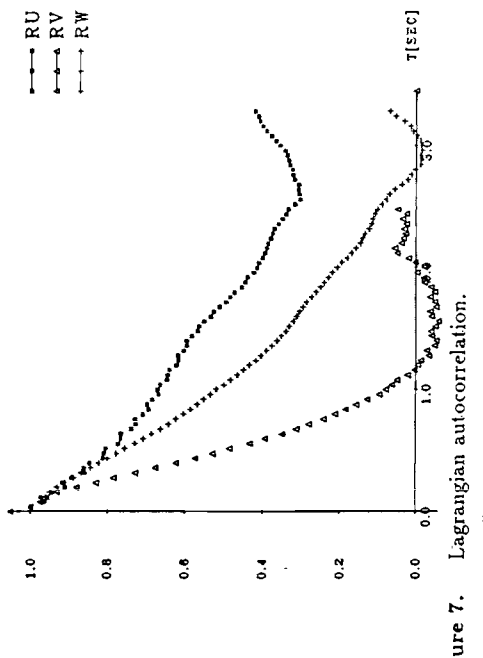


Figure 7. Lagrangian autocorrelation.

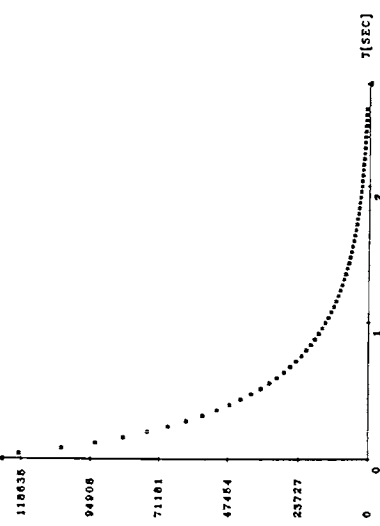


Figure 8. Number of products used for each lag value

The computed Lagrangian autocorrelation curves are presented in Figure 7 were we define as usual,

$$Ru(t) = \frac{u(t_0)u(t_0 + t)}{\overline{u^2}}$$

The unbiased estimator was used in the computation and the number of products used for each lag value is shown in Figure 8.

The Lagrangian autocorrelation compares well with the measurements of Sullivan [14] in an open channel flow. Sullivan's reported measurements have a maximum lag value corresponding to about 18.5 seconds under our flow conditions. However, 150 different records (sets) of trajectories were used to compile the statistics. It is observed that the autocorrelation decreases fastest for the v -component and that the u and w components show a periodicity, which may be caused by the largest scales contained in this flow sample. It is of interest that a similar behavior is exhibited to a large extent in Sullivan's u autocorrelation curve.

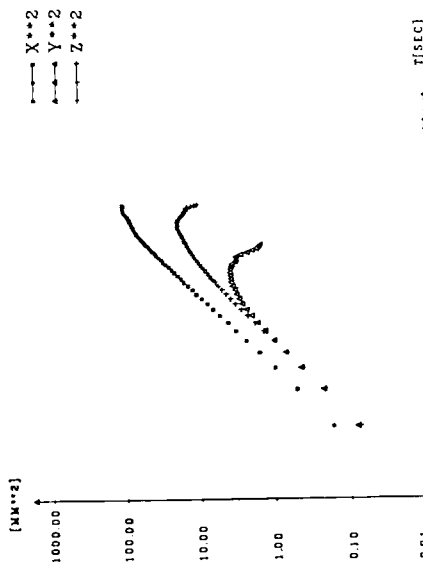


Figure 9. Lateral and streamwise diffusion from a fixed point in open channel flow turbulence.

In Figure 9, the diffusion as a function of time, where

$$\overline{X^2(t)} = 2u^2 \int_0^t (t - r) R(r) dr$$

is presented. The behavior for small times coincides with the predictions of Taylor's theory for homogeneous turbulence, i.e., for small t it is proportional to t^2 and for larger t it increases linearly with t . In that respect these results are in remarkable agreement with the results obtained in an isotropic turbulent flow behind a grid [18]. This shows that in a flow close to a boundary, up to a certain time after release the turbulence appears homogeneous to a particle. It is certainly not isotropic as evidenced by the different behavior of the three correlation curves. For times longer than that, the dimensions of the largest eddies are felt and the periodicity exhibited by the correlation coefficient results to a decrease in the diffusion lengths.

5 Conclusions

A database of 3-D particle trajectories in turbulent open channel flow was obtained by the PTV method. At each time step, a large number of particle positions are determined with good accuracy in the flow test section by a photogrammetric and stereo matching analysis. The particle positions are tracked in time to obtain the particle trajectories.

Analysis of the trajectories obtained during a 15 second interval during which the observation system convected at a speed almost equal to the speed of the mean flow revealed that mean and rms velocity values converge to their Eulerian long time averages. The Lagrangian autocorrelation and diffusion lengths computed from these trajectories show that the flow behavior at times up to the Lagrangian integral scale is identical to that of isotropic flow. For longer times, the dominant large eddies contained in this flow segment affect both the autocorrelation and the diffusion lengths.

This research was supported by the Swiss National Science Foundation through Grant No. 2.506-0.87 and by the ETH. The authors express their appreciation to their Photogrammetrist colleagues Prof. A. Gruen and H-G Maas who developed the calibration and positioning algorithms and contributed to the PTV development effort in a variety of ways.

6 References

1. J. Kim, P. Moin and R. Moser, 1987, *JFM* **177**, p. 133.
2. J.A. Clark 1968, A study of incompressible turbulent boundary layers in channel flow, *Trans. ASME, Ser. D* **90**, p. 455.
3. H.P. Kreplin and H. Eckelmann, 1979, *Phys. of Fluids* **22**, p. 1233.
4. E.G. Kastanakis and H. Eckelmann, 1983, *JFM* **137**, p. 165.
5. K. Nishino and N. Kasagi, Turbulence statistics measurement in a two-dimensional channel flow using a three-dimensional particle tracking velocimeter, 7th Symp. on Turb. Shear Flows, Stanford Univ., August 21-23, 1989.
6. T. Utani and T. Ueno, 1987, *JFM* **174**, p. 399.
7. R.G. Racca and J.M. Dewey, 1988, Exp. in Fluids **6**, p. 25.
8. R.E. Elkins III, G.R. Jackman, R.R. Johnson, E.R. Lindgren and J.K. Yoo, 1977, *Rev. Sci. Instrum.* **48**, 7, p. 738.
9. Y.H.E. Sheu, T.P.K. Chang and G.B. Tatterson, 1982, *Chem. Eng. Commun.* **17**, p. 67.
10. T.P.K. Chang, A.T. Wilson and G.B. Tatterson, 1985, *Chem. Eng. Sc.* **40**, 2, p. 269.
11. A.A. Adamczyk nad L. Rinaldi, 1988, Exp. in Fluids **6**, p. 373.
12. W.C. Chiu and L.N. Rib, 1956, *Trans. American Geophysical Union*, **37**, 1, p. 13.
13. P.J. Sullivan, 1971, *JFM* **49**, 3, p. 551.
14. J.C. Agui, and J. Jimenez, 1987, *JFM* **185**, p. 447.
15. D. Papantoniou and T. Dracos, 1989, "Analyzing 3-D turbulent motions in open channel flow by use of stereoscopy and particle tracking", *Advances in Turbulence 2*, Springer-Verlag Berlin, p. 278.
16. I. Nezu and W. Rodi, 1986, *J. Hydr. Eng. ASCE*, **112**, 5, p. 335.
17. Y. Sato and K. Yamamoto, 1986, *JFM* **175**, p. 183.

Establishment of a videogrammetric PTV system

Marko Virant

Institute of Hydromechanics and Water Resources
Management
ETH-Hönggerberg, CH-8093 Zürich, Switzerland

Handouts

Short Course
in
3-D.Velocimetry and Image Analysis Techniques
Zurich, March 1-3, 1995

Introduction

Observation volume

Optics

CCD sensor

Interlacing

Illumination

Flow markers

Exploitation of the dynamic range

Limitation of maximum number of particles

Calibration

Hardware setup

Smoothed and asynchronous digitization

Example of 3D PTV application

Introduction

A new system was to be implemented according to the theoretical considerations of the hydromechanical problem and the requirements of the image- and dataprocessing.

In this presentation the necessary considerations of the establishment of a 3D PTV system will be discussed.

Special focus will be led on building up a system with of-the-shelf products. Some features which are important for the image and data quality will be handled in more detail. It is very important to realize that a carefully established system and carefully performed experiments are the basis for the further processing and analysis and that it is usually not possible to recover from mistakes in the data acquisition.

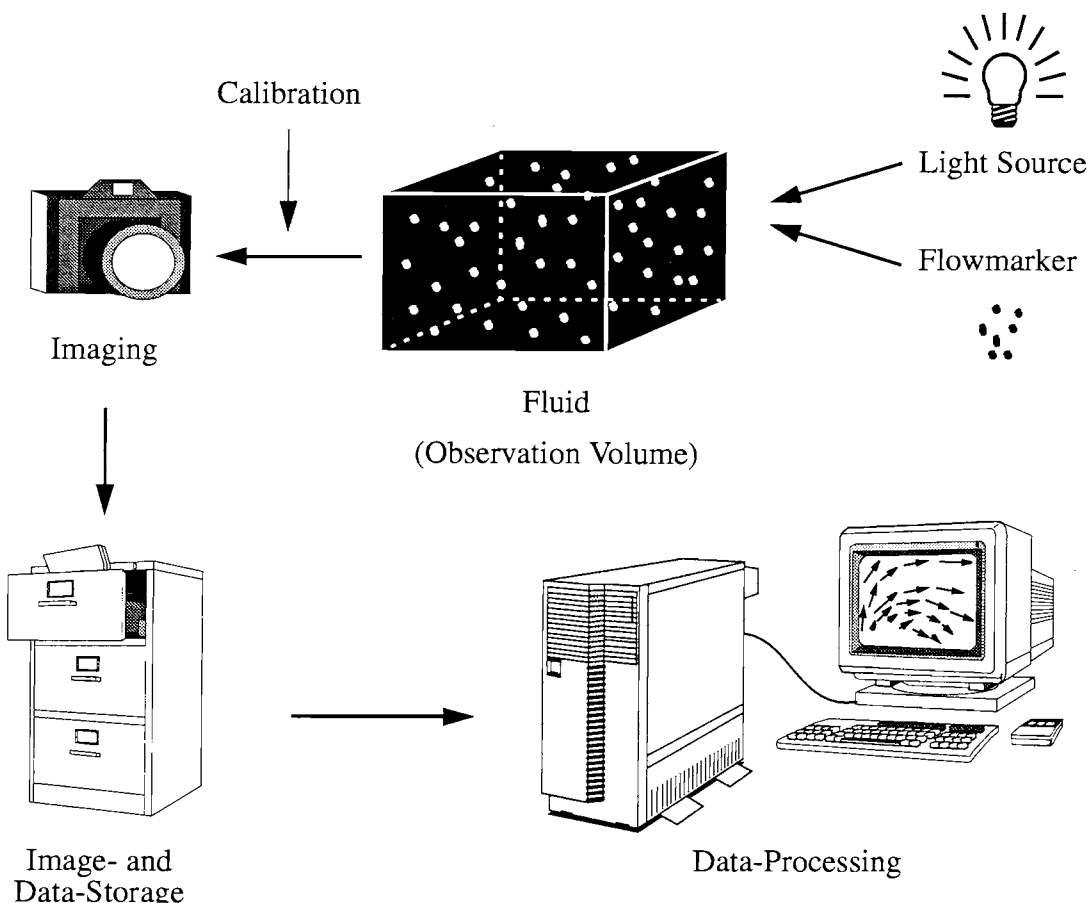


FIGURE 1. Basic elements of PTV

The obseravtion volume

The observation volume contains the area of the flow to be investigated. It is determined by the light sheet. The depth of focus of the cameras should be adapted to the thickness of this light sheet.

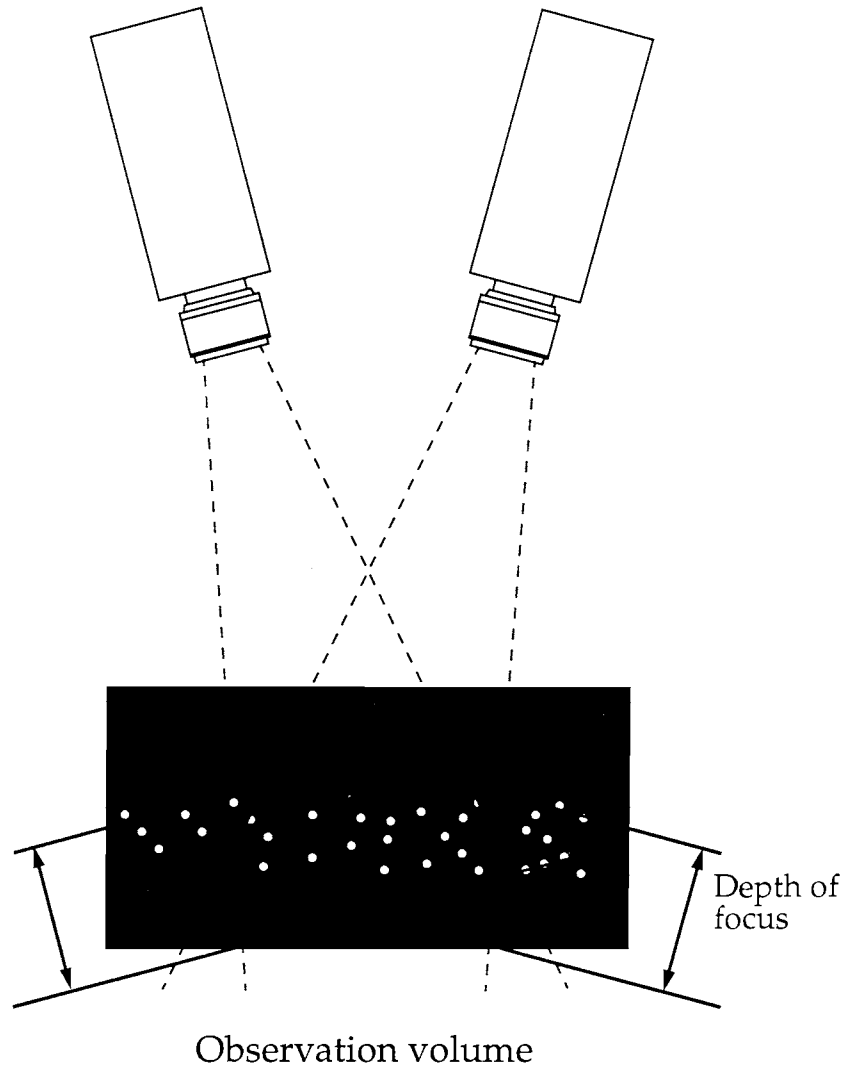


FIGURE 2. Principle determination of the observation volume

Optics

Focal length

$$f = \frac{a}{1 + \frac{1}{\beta'}} = \frac{a}{1 + \frac{y'}{y}}$$

Field of view

$$\omega = \text{atan} \frac{y'}{f}$$

Object size

$$a = \left(\frac{a}{f} - 1 \right) \cdot y'$$

Image size

$$y' = \frac{1}{\frac{a}{f} - 1} \cdot y$$

Object distance

$$a = \left(1 + \frac{1}{\beta'} \right) \cdot f = \left(1 + \frac{y}{y'} \right) \cdot f$$

Iris

$$k = \frac{f}{\varnothing_{EP}}$$

Depth of focus

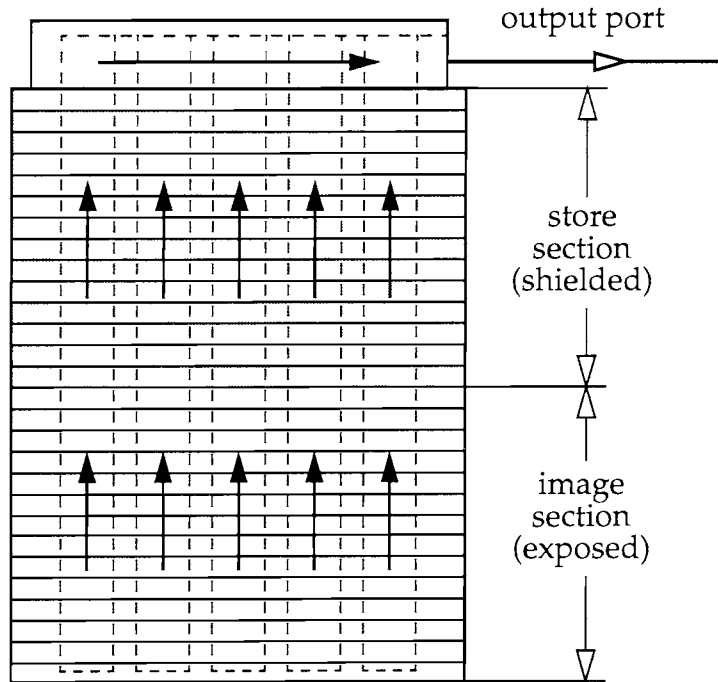
$$a_v = \frac{a \cdot f^2}{f^2 - u_{\varnothing'} \cdot k \cdot (a + f)}$$

$$a_h = \frac{a \cdot f^2}{f^2 + u_{\emptyset} \cdot k \cdot (a + f)}$$

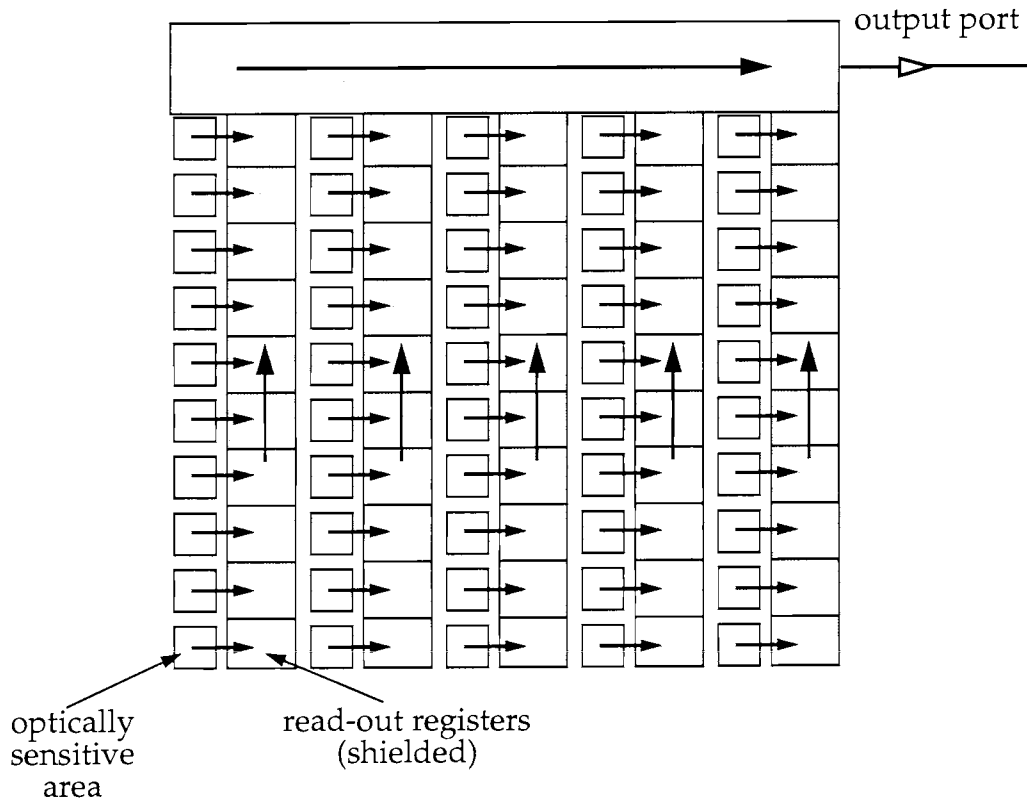
- a Object distance
y Object size (diagonal)
y' Image size (diagonal)
for 1/2" format $y'=8\text{mm}$
for 2/3" format $y'=11\text{mm}$
for 1/1"format $y'=16\text{mm}$
k f-step (Iris)
 β' Magnification $\beta'=y'/y$
 u_o' for example 2/3" format CCD $u_o'=30\mu\text{m}$

CCD sensor

Frame transfer CCD sensor (FT)



Interline transfer CCD sensor (ILT)



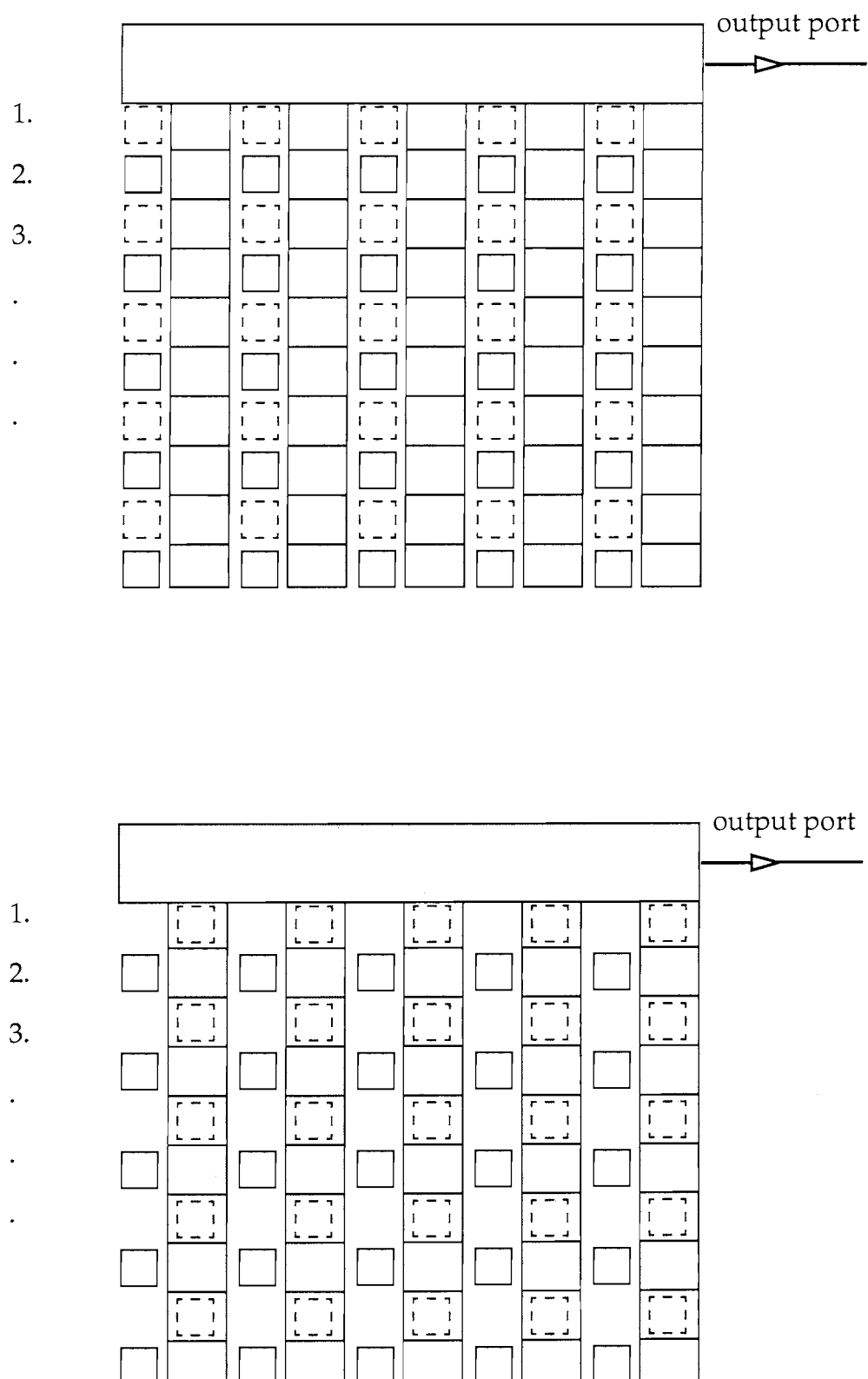
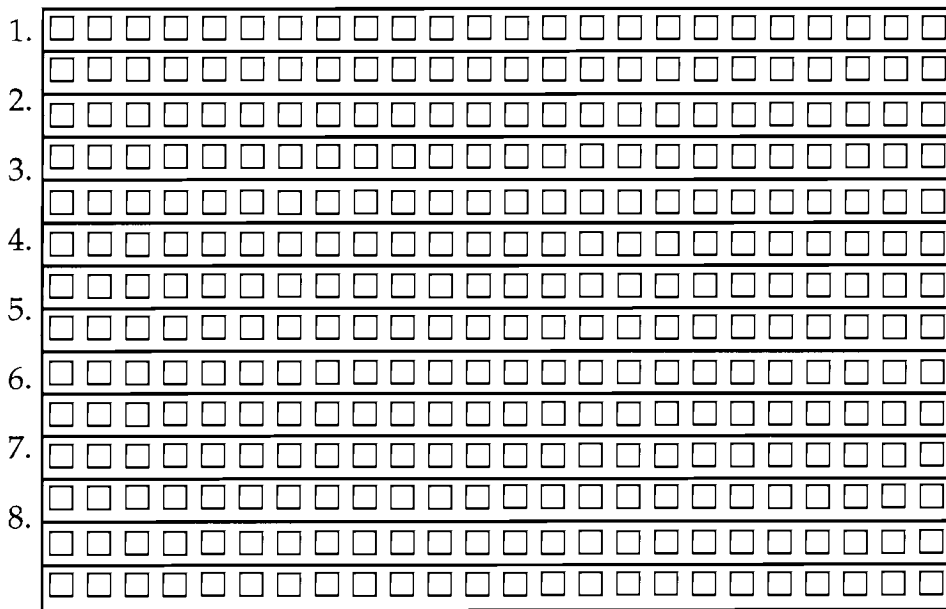


FIGURE 3. Integration scheme of a CCD sensor

Interlacing

In vertical interlace technique the odd and even lines of the frame are integrated, scanned and displayed alternately. This reduces the visible flicker for the human eye on the screen of a conventional TV display, in other words it increases the vertical resolution beyond the Nyquist limit imposed by the vertical separation of the elements.

The figure below sketches the separated integration of the odd and even lines.



Field 1 : odd numbered lines

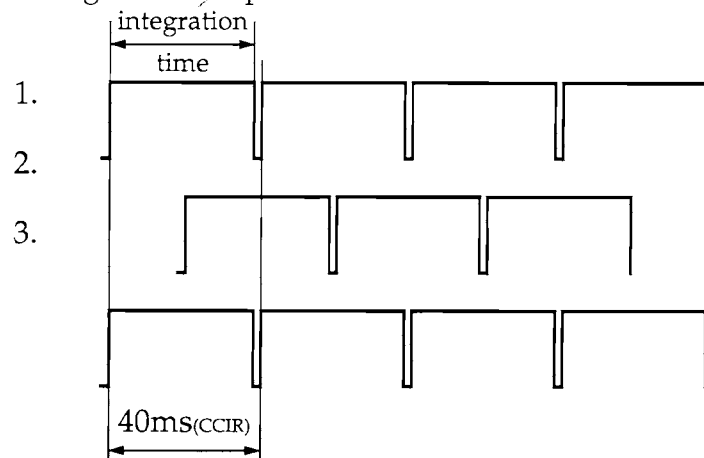
Field 2 : even numbered lines

Frame : Field 1 + 2

Standard CCD-cameras are working with a videonorm specifications:

	B/W	Color	
USA/ Japan	RS 170/EIA	NTSC	
Europe	CCIR	PAL/ Secam	
		RS 170/ EIA	CCIR
Frame Rate/ Field Rate		30/ 60 Hz	25/ 50 Hz
Number of lines		525	625
Number of active lines		480	576
Field time		16 2/3 ms	20 ms
Time per line		63.49 μ s	64 μ s
Active line period		~52.5 μ s	52 μ s
Nominal video bandwidth		4.5 MHz	5.5 MHz
Resolution(Nyquist)		472	572
Aspect Ratio		4 : 3	4 : 3

The scheme below shows the shifted integration times of the odd and even lines according to the european CCIR norm.



Imaging moving particles in frame integration mode with an integration time of ~38.2 ms (40ms minus 1.8ms readout time) leads at higher velocities to streaks and a displacement of the image on field 1 and field 2.

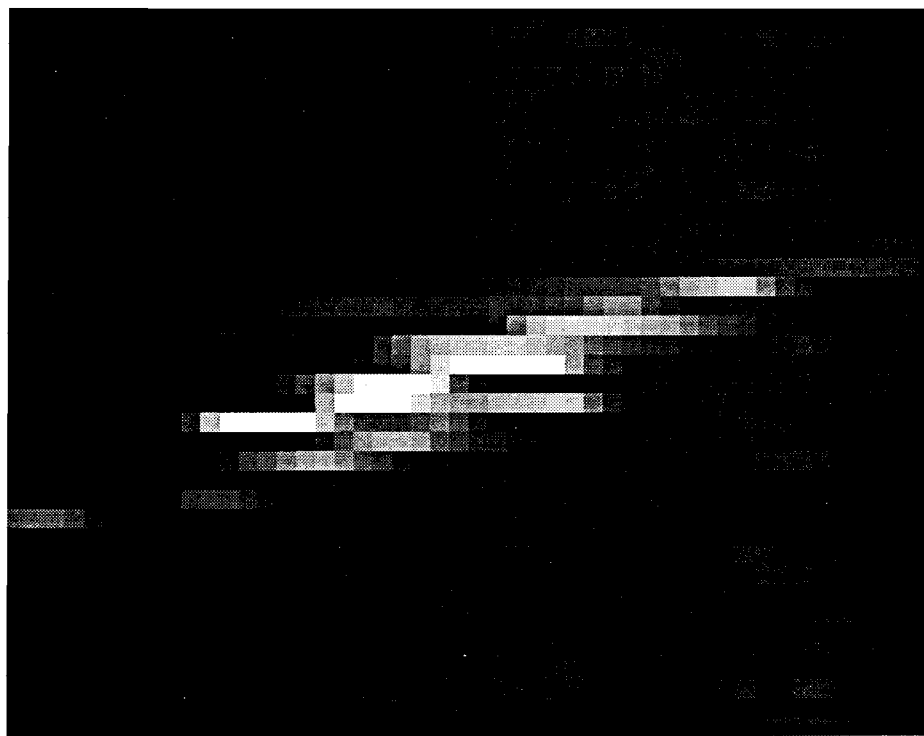


FIGURE 4. Image of a fast moving particle, recorded in frame integration mode

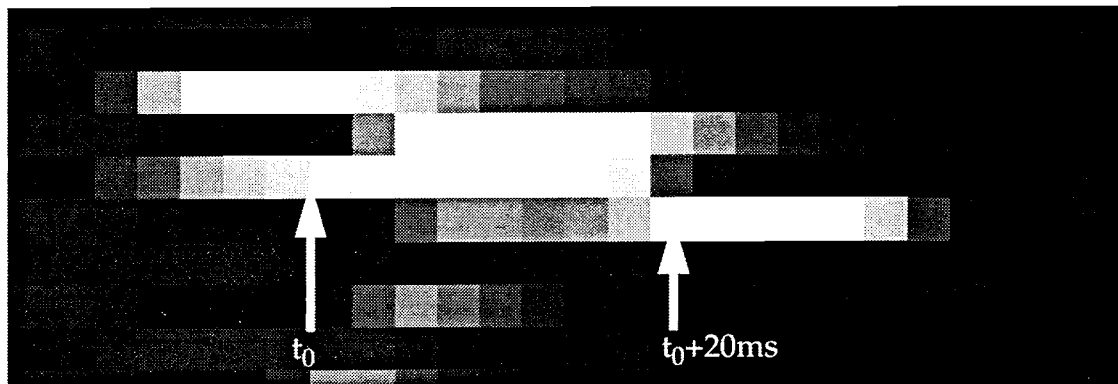


FIGURE 5. Image of a particle, recorded in frame integration mode

This distorted images of the particles cause errors and an unprecise determination of the position in the image. There are two possibilities to avoid this source of errors. First to flash or to chopper the light in phase and frequency of the frame rate of the CCD-devices. Secondly to shutter the integration time of the CCD-sensor. This is only possible with field rate. The time resolution is therefore doubled, but the spatial resolution decreases by a factor of 2.

1.

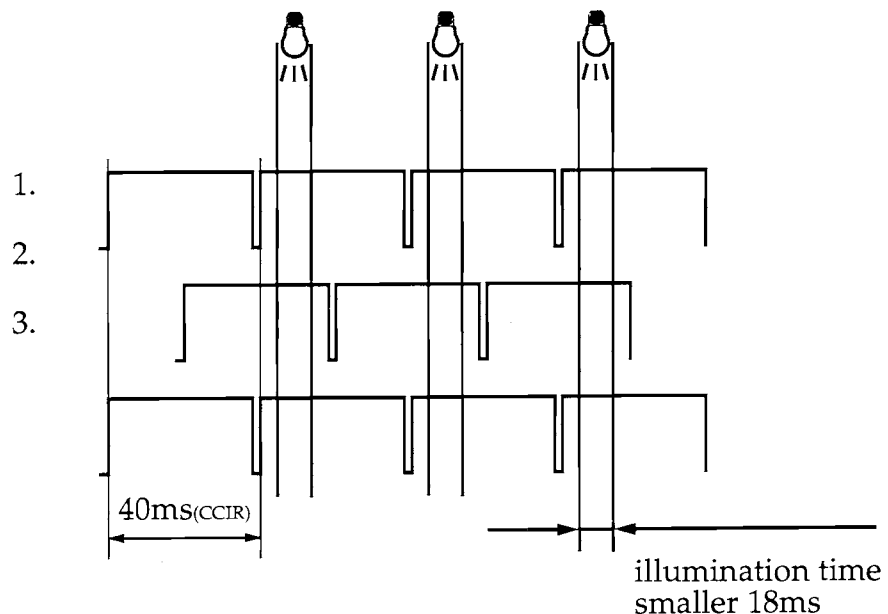


FIGURE 6. Pulsed illumination

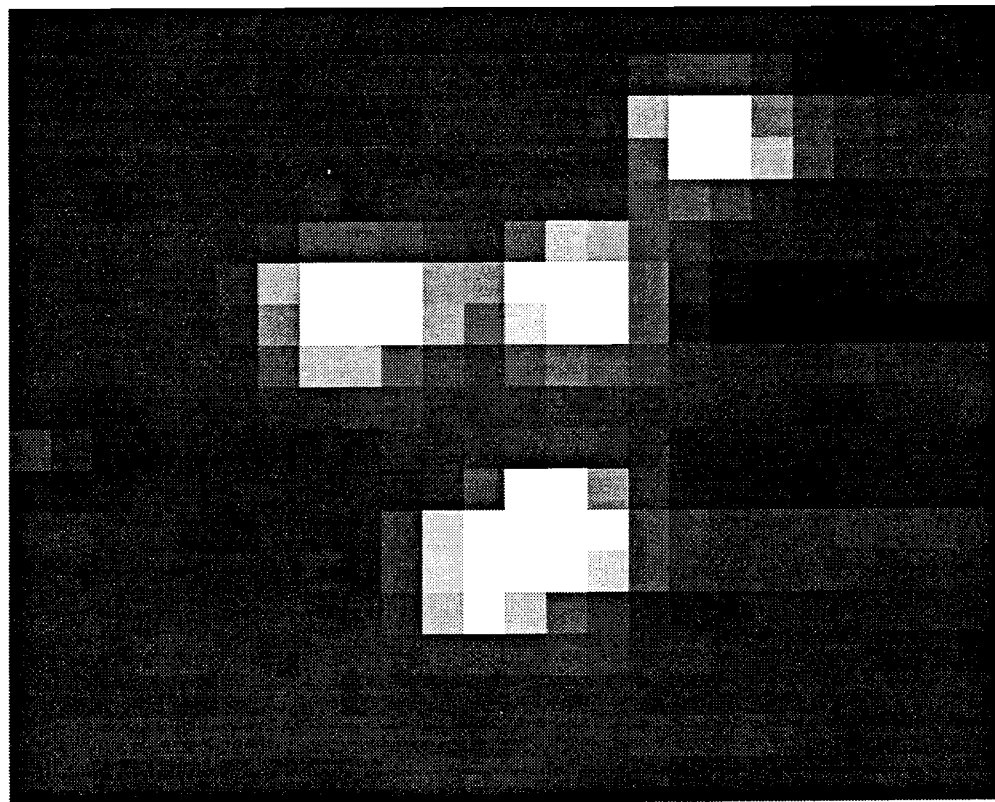


FIGURE 7. Properly illuminated and recorded particles

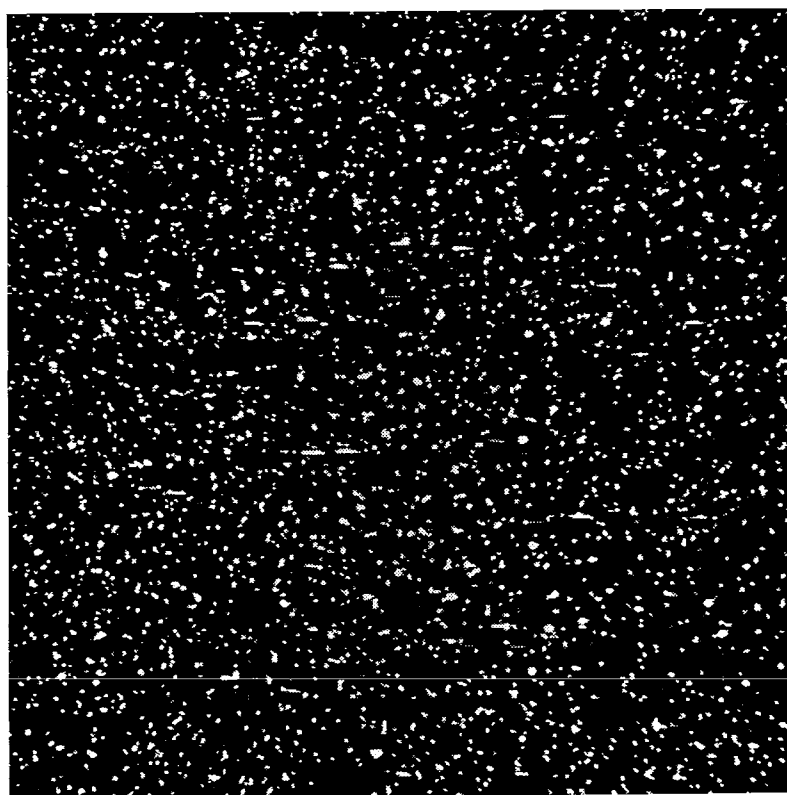


FIGURE 8. High-pass filtered particle image with a very high particle density

2.

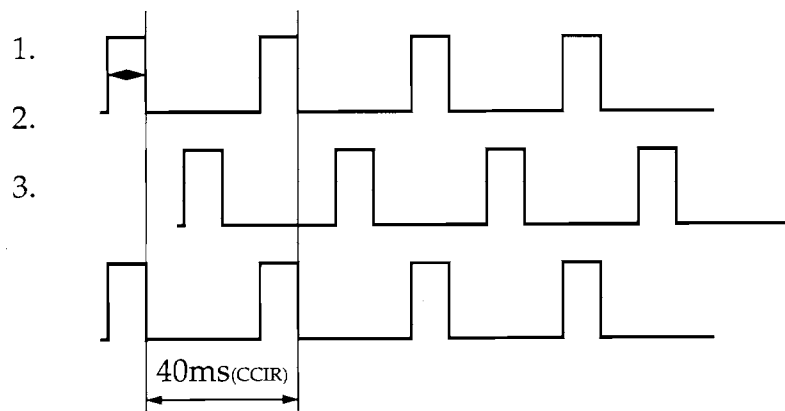


FIGURE 9. Integration time of electronically shuttered cameras

The integration times of the fields may overlap, the readout of the sensor and the display on a screen has to be sequential. The image below shows the normed TV scheme.

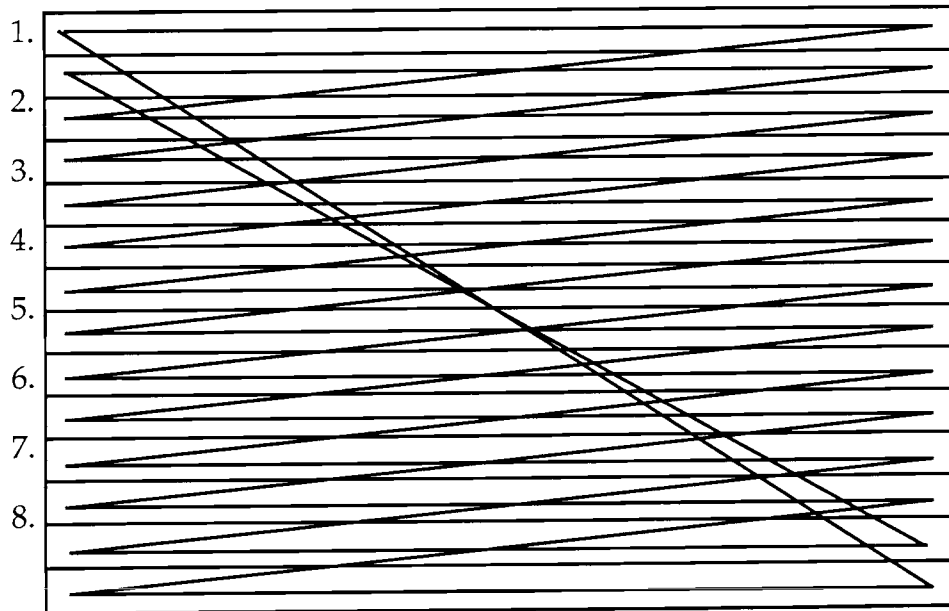


FIGURE 10. Readout and display mode of normed CCD Chips and TV screens

Spectral response

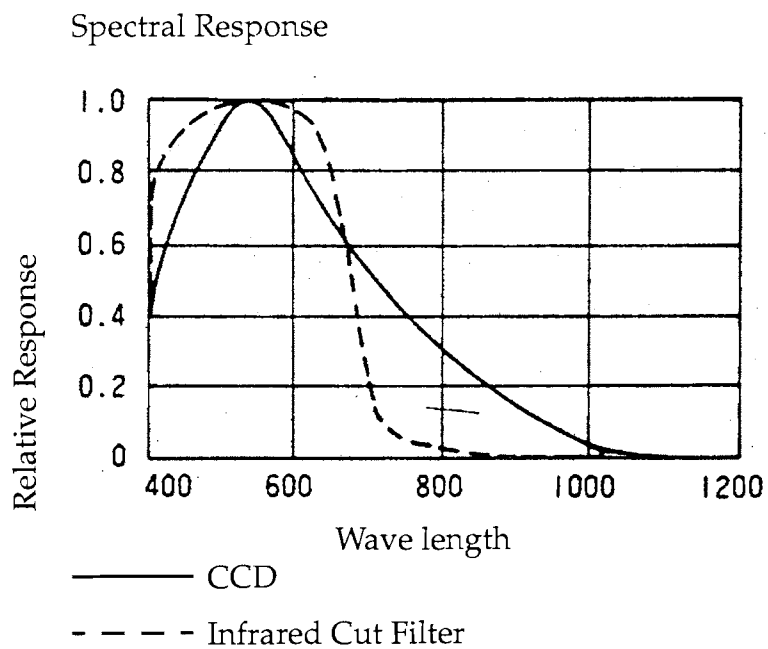


FIGURE 11. Spectral response of conventional CCD sensors

Illumination

Advantages and disadvantages of different light sources with respect to the requirements

of a homogenously illuminated observation volume.

	advantages	disadvantages
Argon-ion laser	<ul style="list-style-type: none"> • high intensity • exact positioning of the light-sheet • monochromatic light 	<ul style="list-style-type: none"> • inhomogeneous intensity distribution over the beam profile (Gaussian profile) • expensive • high energy consumption
diode laser	<ul style="list-style-type: none"> • high intensity • exact positioning of the light-sheet • monochromatic light • low power consumption (high efficiency) 	<ul style="list-style-type: none"> • inhomogenous intensity over the cross-section of the beam (Gaussian profile) • expensive • difficult handling
Halogen-wire-lamp	<ul style="list-style-type: none"> • easy handling • high flexibility in combination with glass-fibre optics, good intensity profile over lightsheet • inexpensive 	<ul style="list-style-type: none"> • relatively low intensity • disadvantageous spectral emission for CCD -sensor (light emits maximal in blue color - the highest CCD-sensitivity lies in the red band)
Halogen-short-arc-lamp	<ul style="list-style-type: none"> • high intensity • high flexibility in combination with glass-fibre optics, good intensity profile over lightsheet • inexpensive 	<ul style="list-style-type: none"> • difficult handling • disadvantageous spectral emission for CCD -sensor (light emits maximal in blue color - the highest CCD-sensitivity lies in the red band)

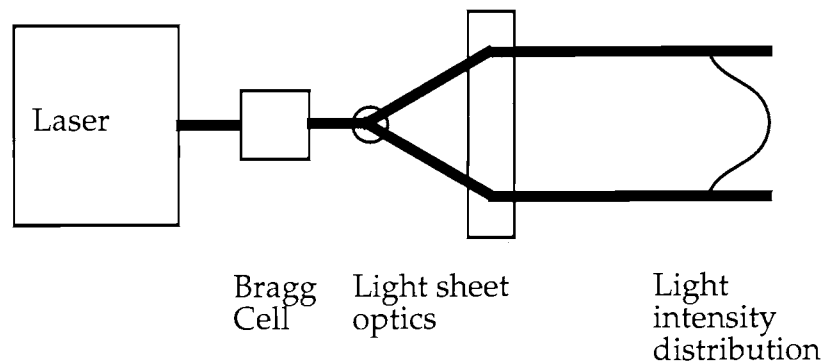


FIGURE 12. Light distribution in a laser sheet

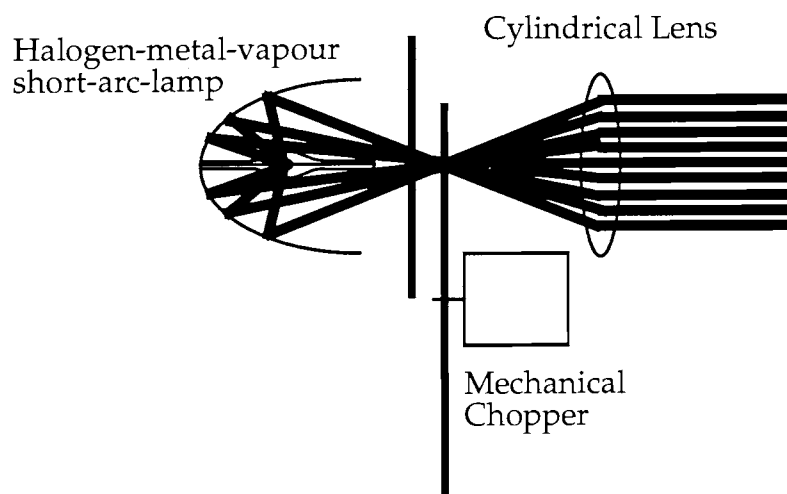


FIGURE 13. Light sheet generated by a arc lamp

Flow markers

Using the PTV system as a flow velocimetry and not as a particle velocimetry system (which is also possible) neutrally buoyant flow markers have to be used in order to visualize the flow. Thus they have to meet some interfering requirements. The main mechanical requirement to be posed to the markers is to follow the flow exactly without disturbing it. This means that the velocity difference $|v_p - u|$ between the velocity of the particle v_p and the velocity of the fluid u at any instant must be small, say less than 1 per-cent of $|u|$. For small particle Reynolds number (Adrian 1991):

$$|v_p - u| = \frac{\rho_p \cdot d_p^2 \cdot |\dot{v}_p|}{36 \cdot \rho \cdot v}$$

Some requirements of the imaging system are in contradiction to this mechanical tasks. The particles should be bright as possible to obtain the a good exploitation of the dynamic greylevel range. This exploitation should be reached with a large f-step in order to get a large depth of focus.

Further requirements are spherical shape of the particles to be identically visible from the different camera positions and in consecutive frames. A small variation of the size is also important to avoid this problems especially in the case, when the particle is so small to be near the lower recognizable size an thus disappearing.

For special applications of the PTV two small band distributed particles could be used to discriminate them and track them separately in the same observation volume. For the discrimination could be also the color be used, when filters would be applied in front of the cameras.

The following table shows some convenient particles for measurements in water

	spec. density	color/ brightness	shape	diameter/ range	remarks
Pliolite/ Vestosint	1.02	white	nearly spherical	1 - 500µm	have to be sieved
Hollow glass spheres	1	silver coated available	spherical	10µm	appropriate for thin laser sheet
Fluorescent particles	0.95 - 1.1	absorption peak 510 nm emission 530 -540 nm	nearly spherical	20 - 40µm 50 - 70µm	
Lycopodium	1	yellow		30µm	

Exploitation of the dynamic range

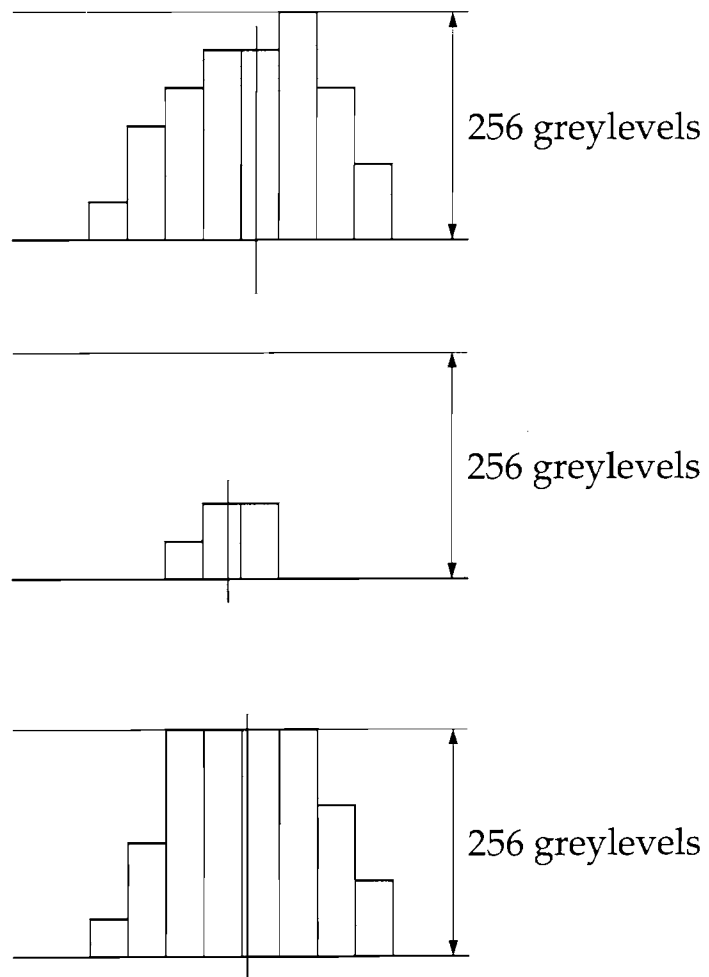


FIGURE 14. Optimal image of a particle

Limitation of maximum number of particles

The possible discrimination of the discrete particles on the image of the CCD-Sensor determines the maximal resolvable number of particles. The optimum size of the images of the particles is between a diameter of 3 - 4 pixel. This allows a good calculation of the center of gravity on the image with sub-pixel accuracy. With a resolution of 512x512 pixel up to 2000 particles can be used. The size of the observation volume does not have an influence of this number. The size of the observation volume will be determined through the objectives.

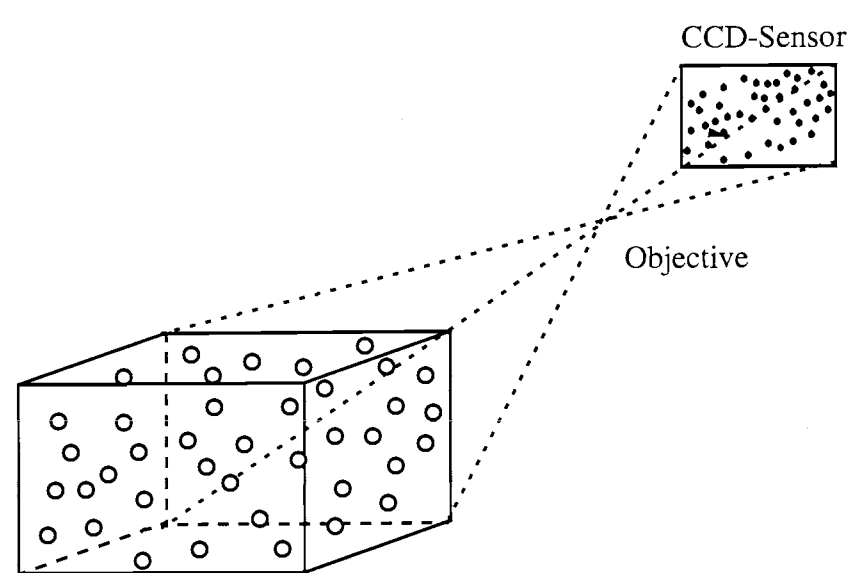
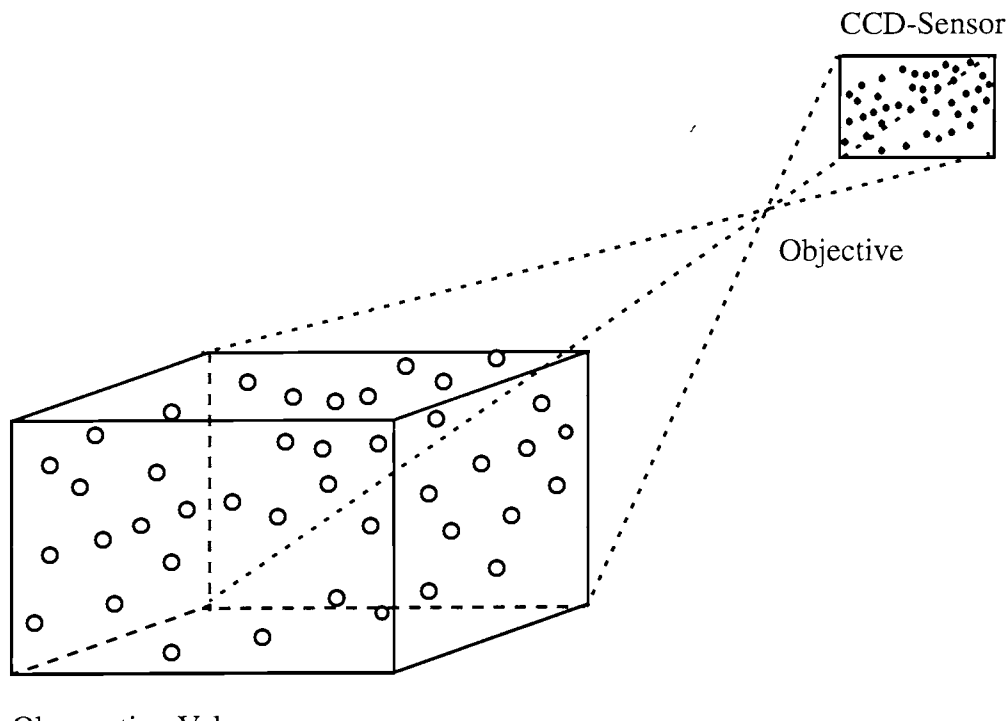


FIGURE 15. Conjugate ratio

Calibration

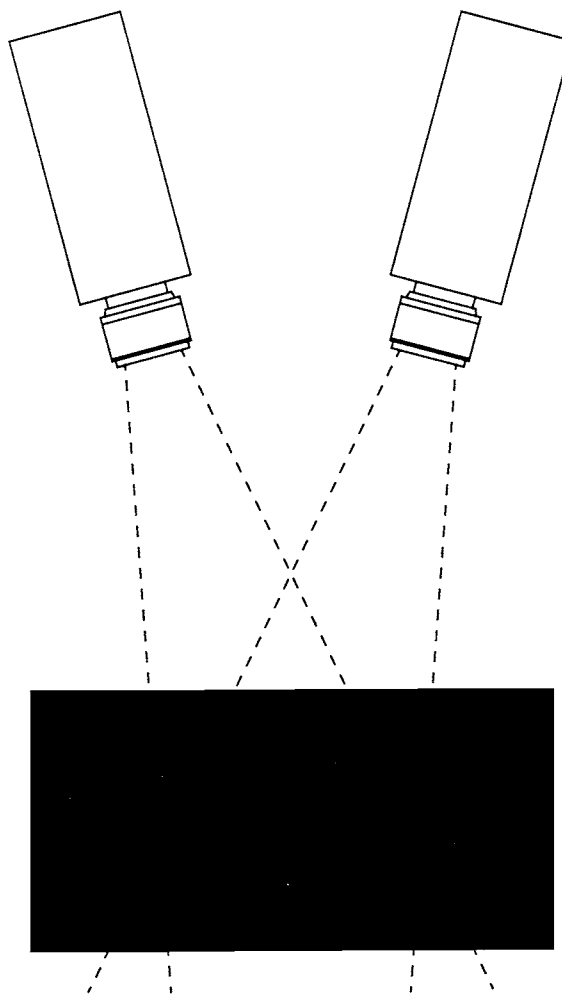


FIGURE 16. Calibration points in the observation volume

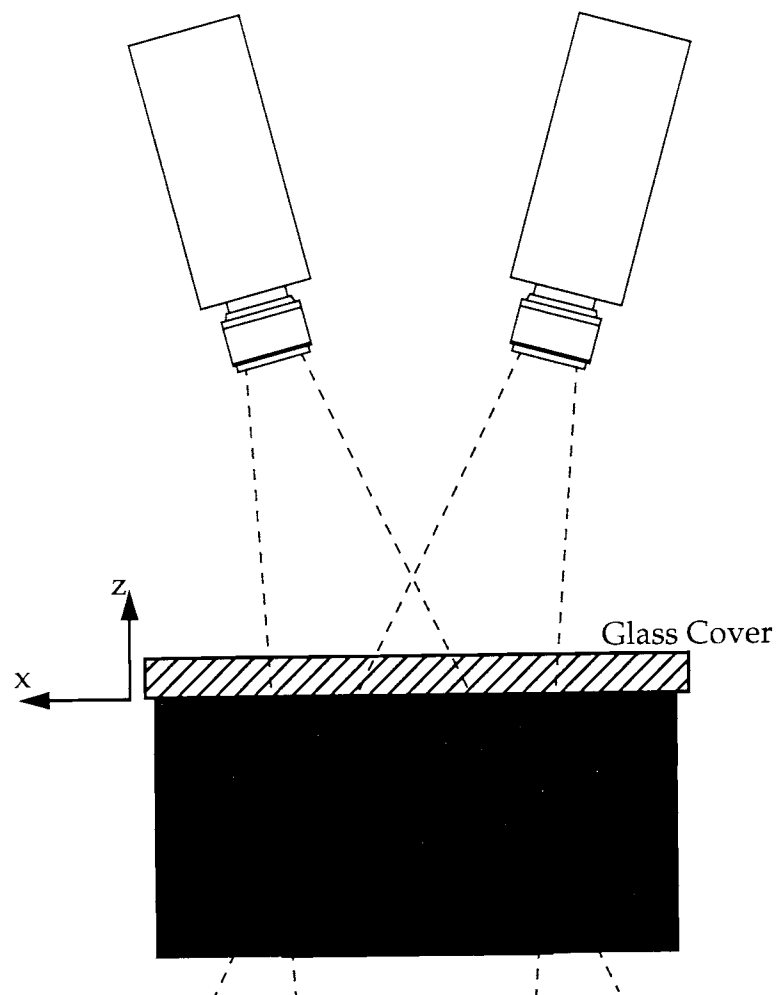


FIGURE 17. Calibration points generated by a 3-D reference body

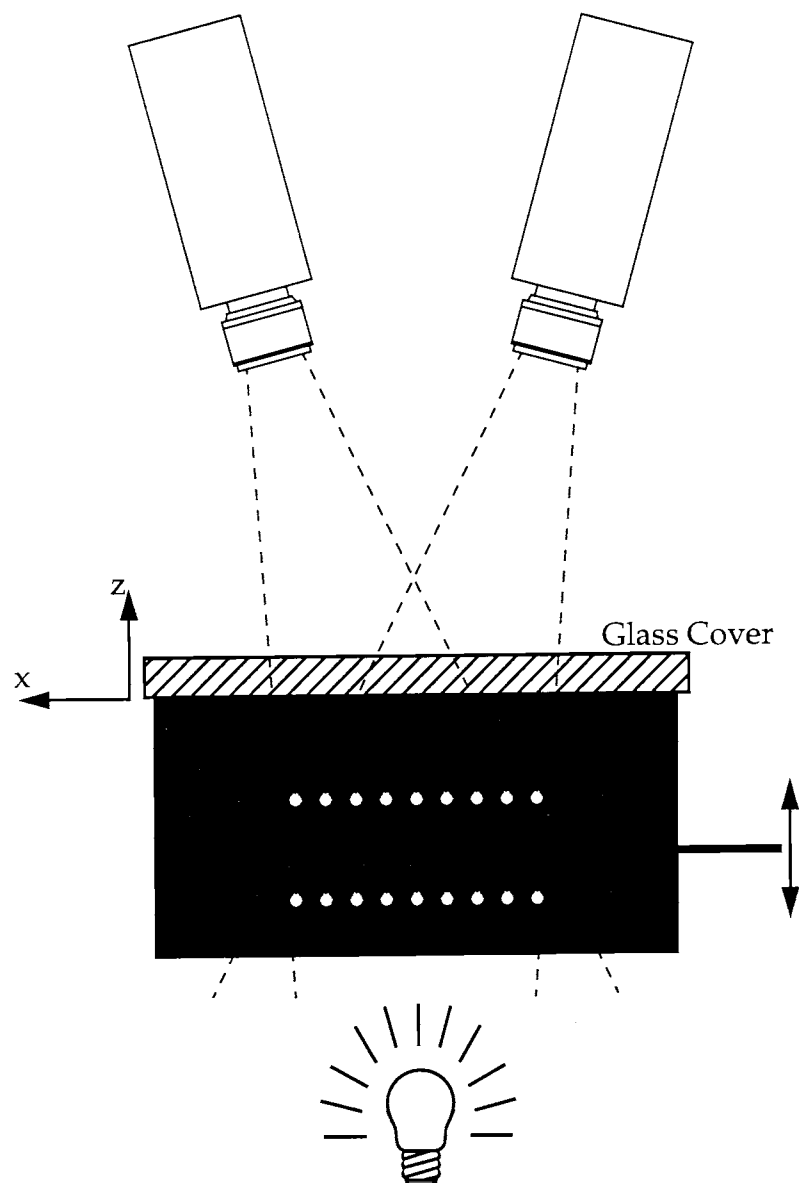


FIGURE 18. Calibration points generated by a moved 2d reference body

Hardware setup

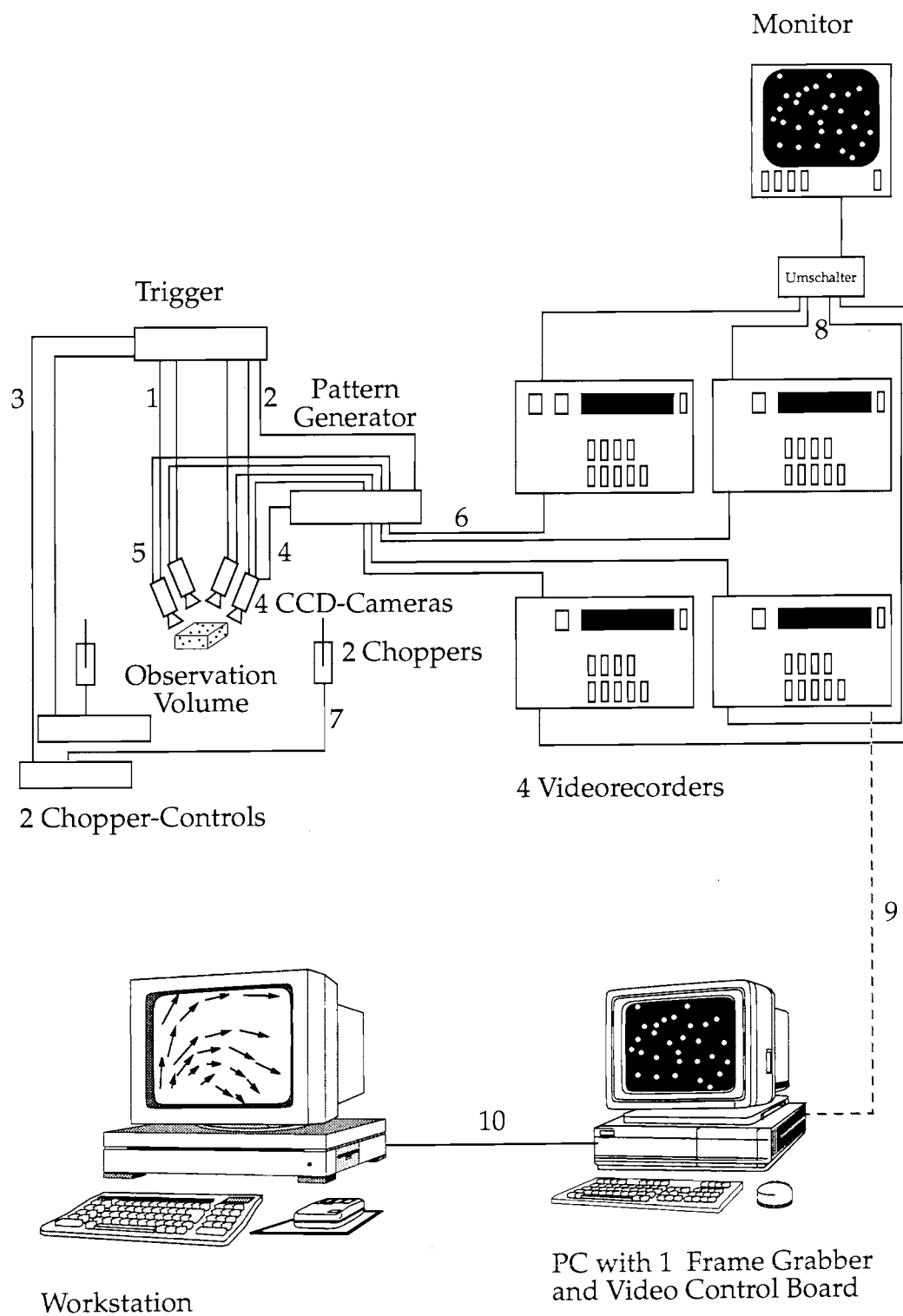
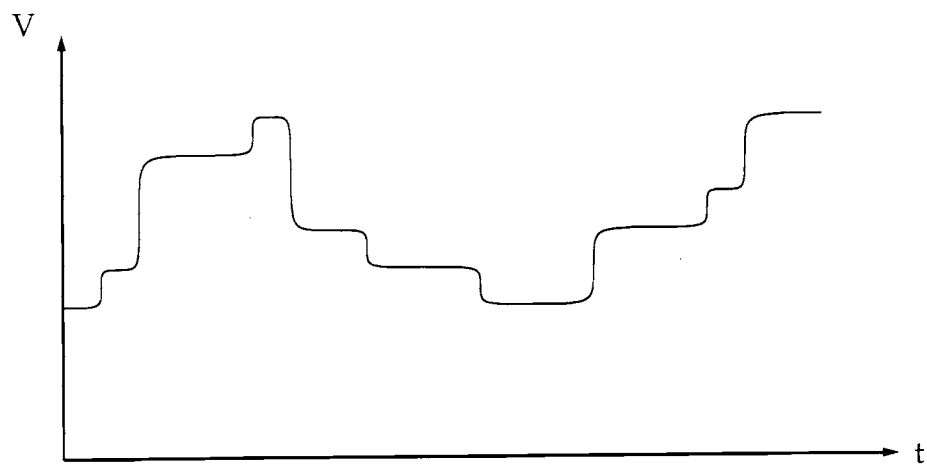
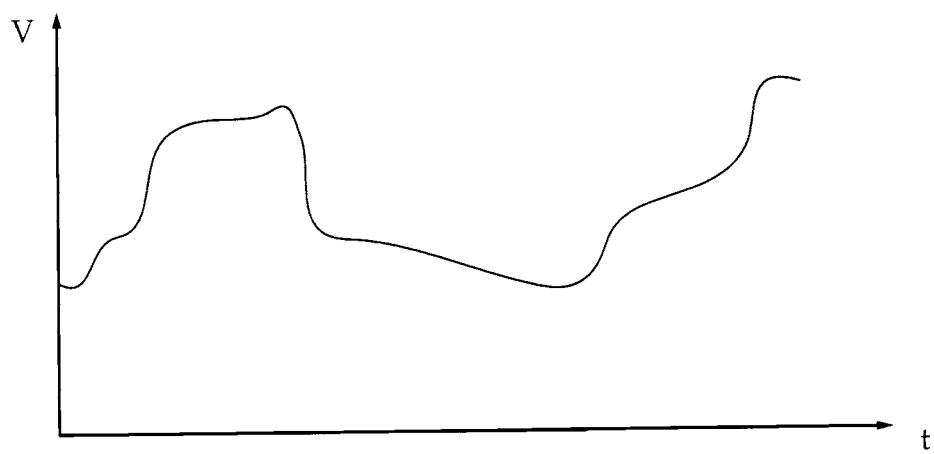


FIGURE 19. Hardware setup with analog storage

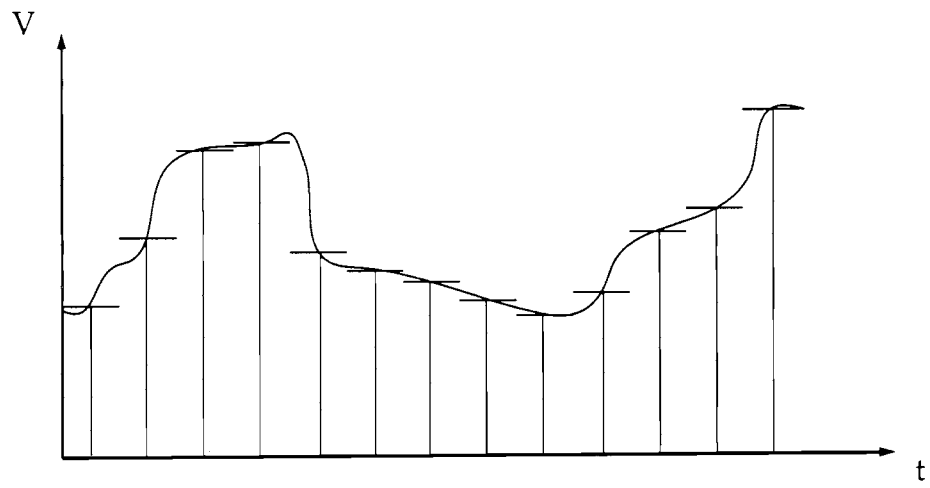
Smoothed and asynchronous digitization



The output signal of a CCD-Camera is a stepped analog Signal. Every step represents the brightness of a pixel. This signal also contains marks for the beginning of a new field and a line. (H and V Sync)



An analog storage smoothes this analog signal.



When this signal is A/D-converted, especially in another resolution like 512x512 from a 739x575 image, the information along a line will be changed. The rows are discrete and some lines of the top and the bottom of the image will be discarded..

The effect of a not exact matched digitization occurs also by a direct digitized CCD-signal, it could be avoided, when the digitizer will be synchronized from the camera by a pixel clock signal.

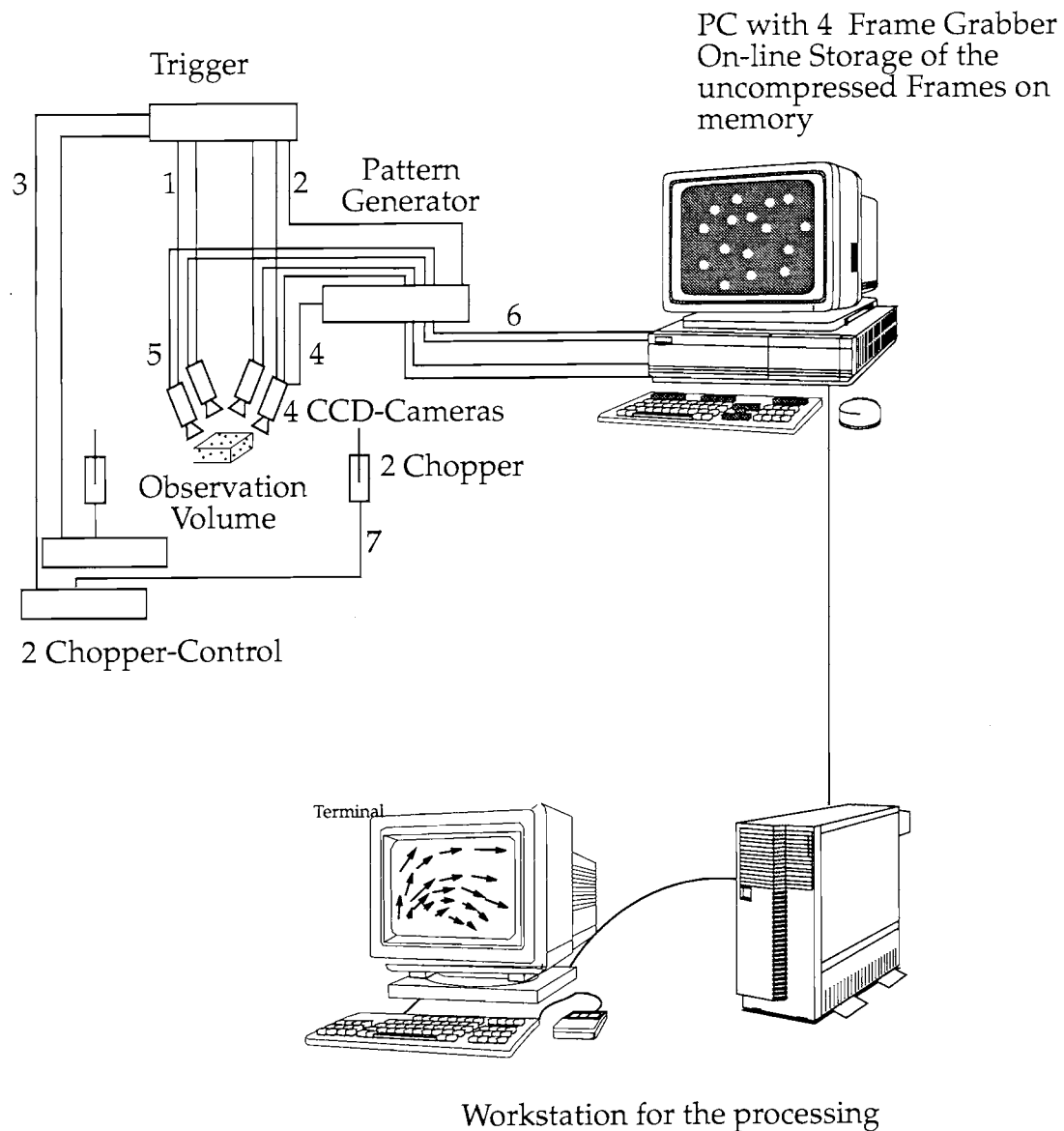


FIGURE 20. 1. Version of direct digitalization

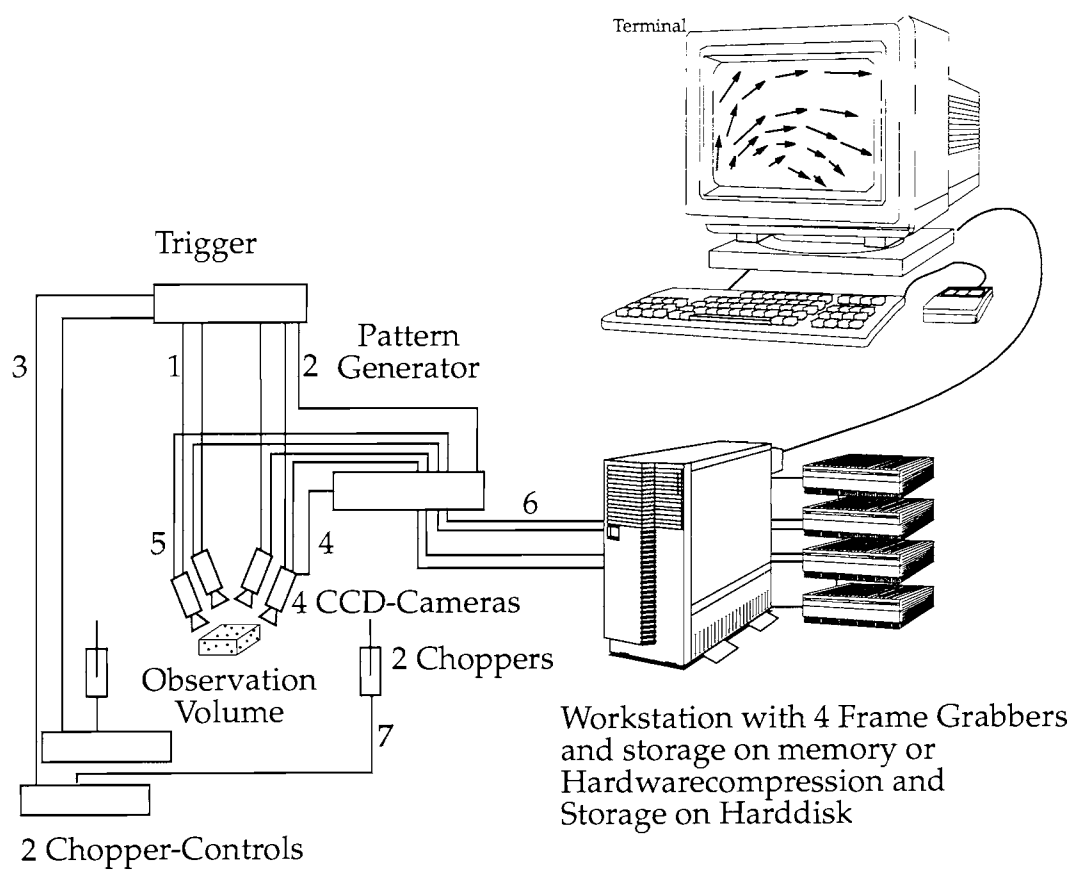


FIGURE 21. 2. Version of direct digitalization

Example of an 3D-PTV application open channel flow

One of the most important features of the 3D PTV is the tracking of individual particles over longer time periods in space. This makes the technique suitable for Lagrangian measurements. Such measurements with a moving observation volume were performed at the open channel of the IHW.

Two carriages, each independently driven by a stepper motor are moving on rails downwards the flow. The velocity of the carriages are about the mean discharge velocity of the flow and measured independently. To obtain a flat optical interface, a glass-plate covers the water surface.

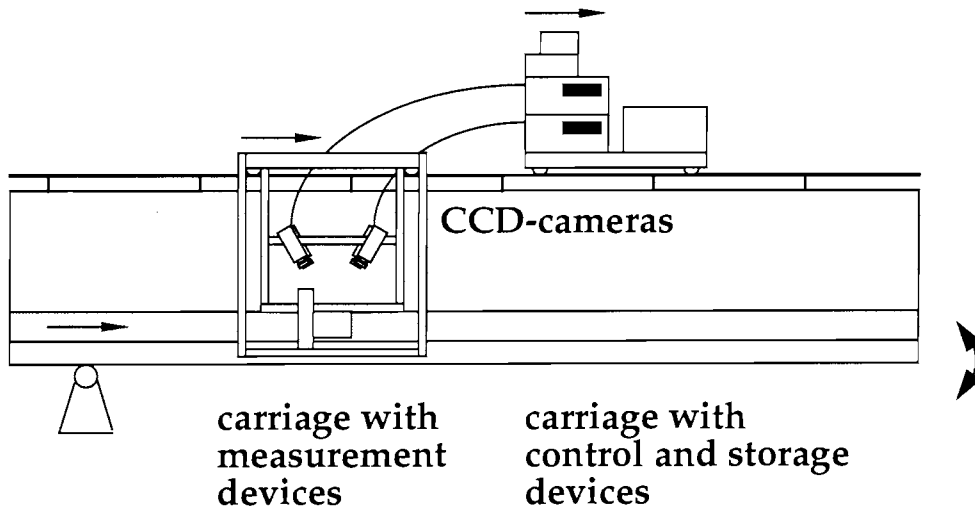


FIGURE 22. side-view of the experimental setup

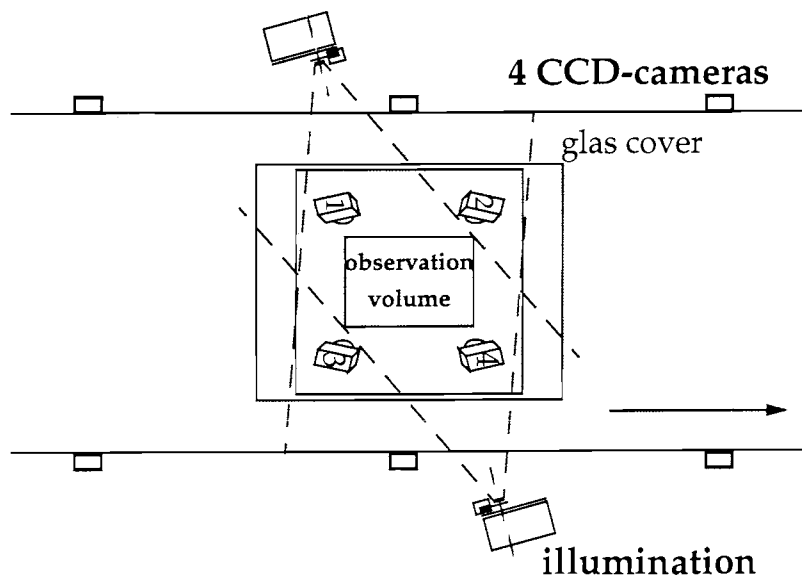


FIGURE 23. Top view of the measurement carriage

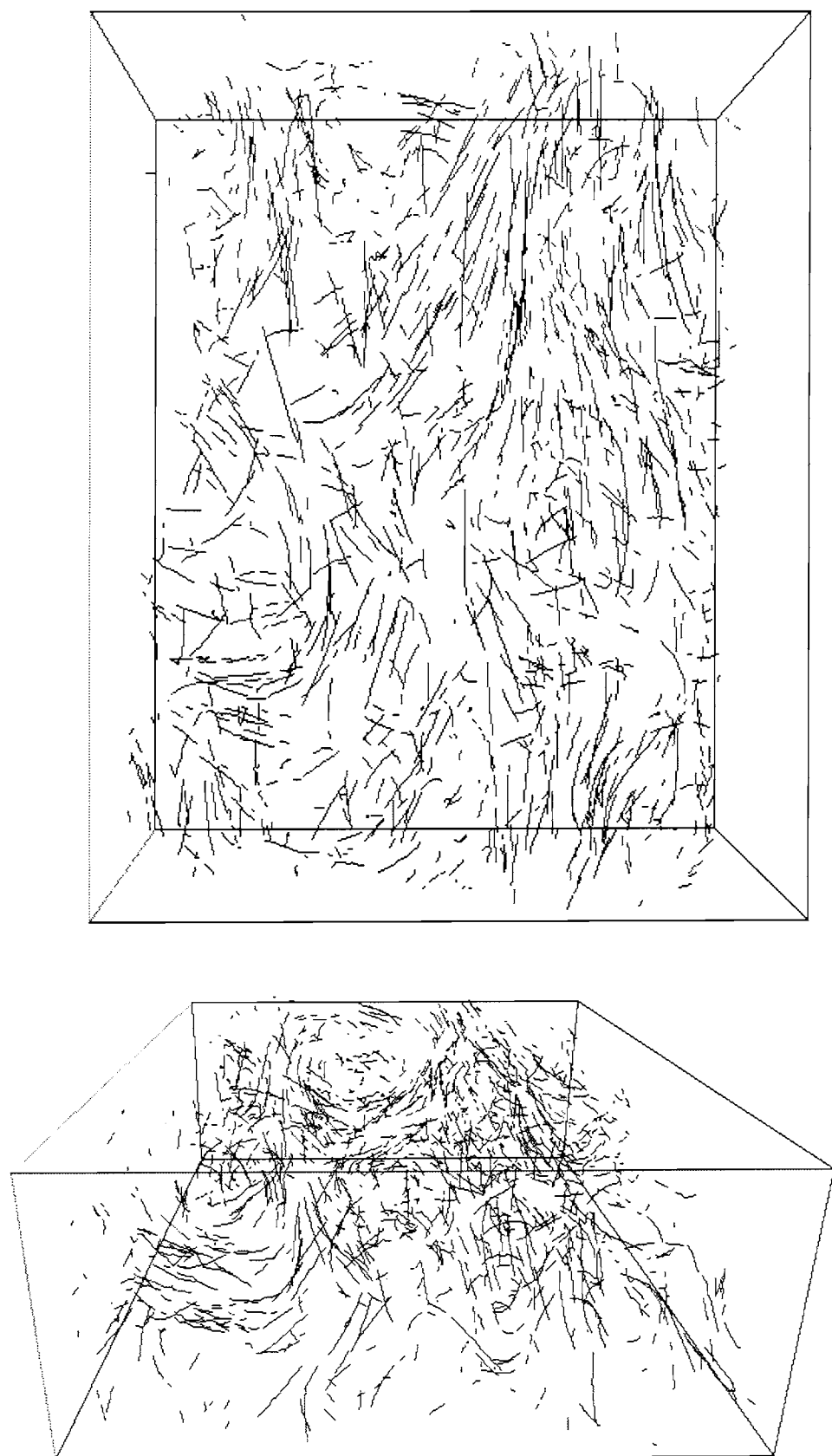
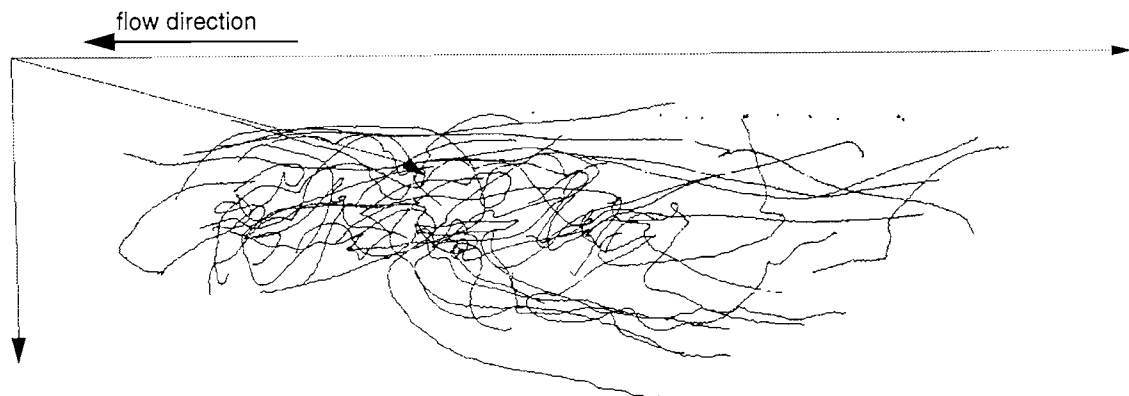


FIGURE 24. Top and frontview of the observation volume over 15 timesteps, 500 vectors per timestep, dimension of the observation volume $40 \times 60 \times 20 \text{ mm}^3$

side view



front and top view

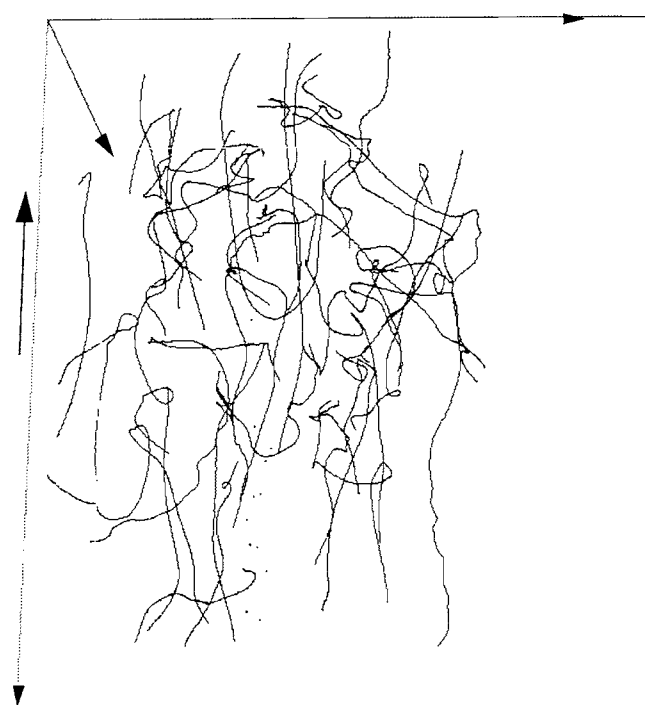
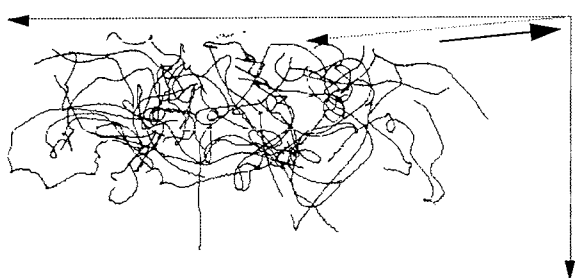


FIGURE 25. 50 trajectories over 250 - 500 timesteps (10-20s), mean discharge velocity 12.6 cm /s, $Re_h = 11'340$, dimension of the observation volume $400 \times 300 \times 90 \text{ mm}^3$ (l x b x h) centered in an open channel flow with a cross-section of $600 \times 90 \text{ mm}^2$ (b x h), reference carriage velocity 14.8 cm/s

Literature

Adrian R.J. (1991)

Particle-imaging techniques for experimental fluid mechanics. An. Rev. Fluid Me. **23**.

Beynon, J. D. E., Lamb, D. R., 1980

Charge-coupled devices and their applications, McGraw-Hill, London.

Merzkirch, Wolfgang, 1987

Flow Visualization, Academic Press Inc., Orlando, Florida.